COMPUTATIONAL STUDY OF NUCLEAR MAGNETIC SHIELDING CONSTANTS

Abril Carolina Castro Aguilera

Per citar o enllaçar aquest document:
Para citar o enlazar este documento:
Use this url to cite or link to this publication:
http://hdl.handle.net/10803/565597

ADVERTIMENT. L'accés als continguts d'aquesta tesi doctoral i la seva utilització ha de respectar els drets de la persona autora. Pot ser utilitzada per a consulta o estudi personal, així com en activitats o materials d'investigació i docència en els termes establerts a l'art. 32 del Text Refós de la Llei de Propietat Intel·lectual (RDL 1/1996). Per altres utilitzacions es requereix l'autorització prèvia i expressa de la persona autora. En qualsevol cas, en la utilització dels seus continguts caldrà indicar de forma clara el nom i cognoms de la persona autora i el títol de la tesi doctoral. No s'autoritza la seva reproducció o altres formes d'explotació efectuades amb finalitats de lucre ni la seva comunicació pública des d'un lloc aliè al servei TDX. Tampoc s'autoritza la presentació del seu contingut en una finestra o marc aliè a TDX (framing). Aquesta reserva de drets afecta tant als continguts de la tesi com als seus resums i índexs.

ADVERTENCIA. El acceso a los contenidos de esta tesis doctoral y su utilización debe respetar los derechos de la persona autora. Puede ser utilizada para consulta o estudio personal, así como en actividades o materiales de investigación y docencia en los términos establecidos en el art. 32 del Texto Refundido de la Ley de Propiedad Intelectual (RDL 1/1996). Para otros usos se requiere la autorización previa y expresa de la persona autora. En cualquier caso, en la utilización de sus contenidos se deberá indicar de forma clara el nombre y apellidos de la persona autora y el título de la tesis doctoral. No se autoriza su reproducción u otras formas de explotación efectuadas con fines lucrativos ni su comunicación pública desde un sitio ajeno al servicio TDR. Tampoco se autoriza la presentación de su contenido en una ventana o marco ajeno a TDR (framing). Esta reserva de derechos afecta tanto al contenido de la tesis como a sus resúmenes e índices.

WARNING. Access to the contents of this doctoral thesis and its use must respect the rights of the author. It can be used for reference or private study, as well as research and learning activities or materials in the terms established by the 32nd article of the Spanish Consolidated Copyright Act (RDL 1/1996). Express and previous authorization of the author is required for any other uses. In any case, when using its content, full name of the author and title of the thesis must be clearly indicated. Reproduction or other forms of for profit use or public communication from outside TDX service is not allowed. Presentation of its content in a window or frame external to TDX (framing) is not authorized either. These rights affect both the content of the thesis and its abstracts and indexes.

Universitat de Girona

DOCTORAL THESIS

Computational Study of Nuclear Magnetic Resonance Shielding Constants

Abril Carolina Castro Aguilera

2017

Doctoral programme in Chemistry

Supervised by: Prof. Dr. Marcel Swart
Tutor: Prof. Dr. Marcel Swart

Presented in partial fulfilment of the requirements for a doctoral degree from the University of Girona

Dr. Marcel Swart, ICREA Research Professor at Institut de Química Computacional i Catàlisi (IQCC), Universitat de Girona,

DECLARE:

That the thesis entitled "Computational Study of Nuclear Magnetic Resonance Shielding Constants", presented by Abril Carolina Castro Aguilera to obtain the doctoral degree, has been completed under my supervision and meets the requirements to opt for an International Doctorate.

For all the intents and purposes, I hereby sign this document.

Prof. Dr. Marcel Swart

Girona, September 28th, 2017

Dedicated to my love,

family, and friends.

List of Publications

The thesis is based in the following publications:

I. A. C. Castro, M. Swart, C. Fonseca Guerra, The influence of substituents and the environment on the NMR shielding constants of supramolecular complexes based on A-T and A-U base pairs, *Phys. Chem. Chem. Phys.*, **2017**, 19, 13496-13502. [cover: *PCCP*, **2017**, 19, 14188.]

II. A. C. Castro, H. Fliegl, M. Cascella, T. Helgaker, M. Repisky, S. Komorovsky, M. A. Medrano, A. G. Quiroga, M. Swart, Four-component relativistic ^{31}P-NMR calculations in *trans*-platinum(II) complexes: Importance of the solvent and dynamics in spectral simulations, *to be submitted.*

III. A. C. Castro, A. Romero, S. Osuna, K. N. Houk, M. Swart, Computational NMR Spectroscopy for Host-Guest Hemicarcerands, *to be submitted*.

IV. A. C. Castro, E. Osorio, J. L. Cabellos, E. Cerpa, E. Matito, M. Solà, M. Swart, G. Merino. Exploring the Potential Energy Surface of E_2P_4 clusters (E = Group 13 Elements): The quest of inverse carbon-free sandwiches, *Chem. Eur. J.*, **2014**, 20, 4583- 4590. [cover: *Chem. Eur. J.* 16/2014.]

Journal Covers

1. *PCCP*, **2017**, 19, 14188.

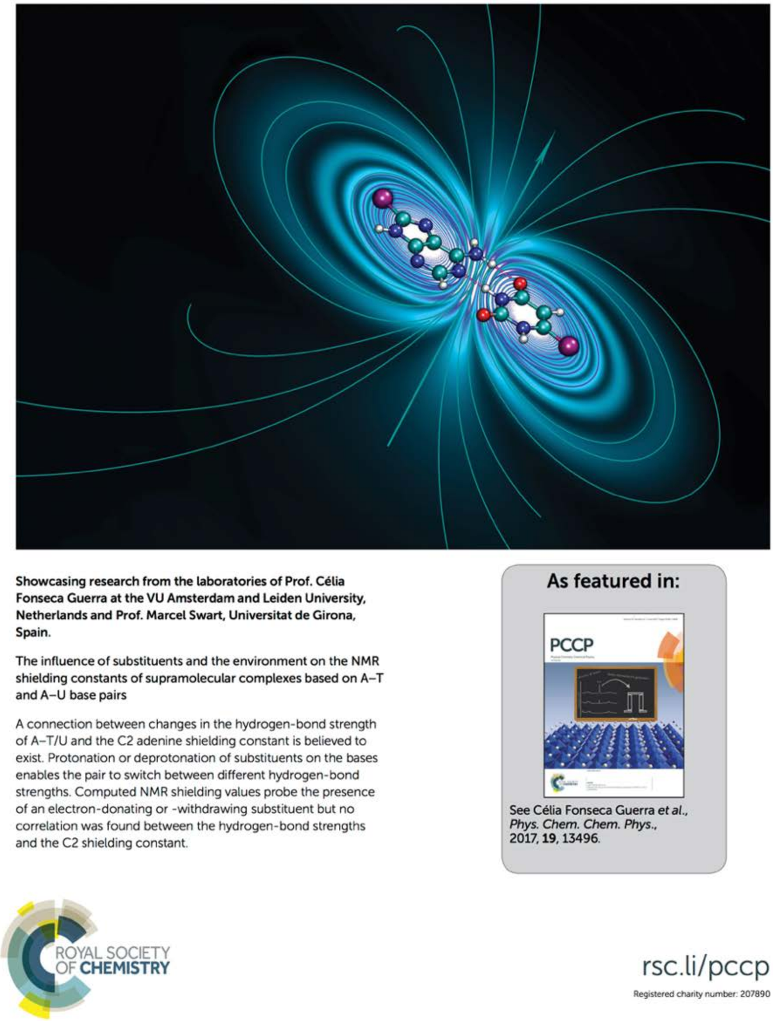

Showcasing research from the laboratories of Prof. Célia Fonseca Guerra at the VU Amsterdam and Leiden University, Netherlands and Prof. Marcel Swart, Universitat de Girona, Spain.

The influence of substituents and the environment on the NMR shielding constants of supramolecular complexes based on A–T and A–U base pairs

A connection between changes in the hydrogen-bond strength of A–T/U and the C2 adenine shielding constant is believed to exist. Protonation or deprotonation of substituents on the bases enables the pair to switch between different hydrogen-bond strengths. Computed NMR shielding values probe the presence of an electron-donating or -withdrawing substituent but no correlation was found between the hydrogen-bond strengths and the C2 shielding constant.

As featured in:

See Célia Fonseca Guerra *et al.*,
Phys. Chem. Chem. Phys.,
2017, **19**, 13496.

ROYAL SOCIETY OF CHEMISTRY

rsc.li/pccp

Registered charity number: 207890

2. *Chem. Eur. J.* 16/2014.

CHEMISTRY
A European Journal

www.chemeurj.org

A Journal of
ChemPubSoc
Europe

2014-20/16

Concept
Access to Optically Active 3-Substituted Piperidines by Ring Expansion of Prolinols and Derivatives
D. Gomez Pardo and J. Cossy

CEUJED 20 (16) 4493–4840 (2014) · ISSN 0947-6539 · Vol. 20 · No. 16 · 2014

Supported by
ACES

WILEY-VCH

Other Publications

V. L. Liu, D. Moreno, E. Osorio, A. C. Castro, S. Pan, P. K. Chattaraj, T. Heine, G. Merino. Structure and bonding of IrB_{12}^{-}: Converting a rigid boron B_{12} platelet to a Wankel motor, *RSC Adv.*, **2016**, 6, 27177-27182.

VI. P. Chakraborty, J. Adhikar, S. Samanta, D. Escudero, A. C. Castro, M. Swart, S. Ghosh, A. Bauzá, A. Frontera, E. Zangrando, D. Das. Combined experimental and theoretical investigation of ligand and anion controlled complex formation with unprecedented structural features and photoluminescence properties of Zinc(II) complexes, *Cryst. Growth Des.*, **2014**, 14(8), 4111- 4123.

List of Figures

Figure 1.1. *Two possible orientations of the magnetic moment of a spinning proton in an external magnetic field.* *8*

Figure 1.2. *Nuclear Zeeman effects. a) A nucleus with I=1/2. b) A nucleus with I=1. The arrow beside each spin line indicates the orientation of the magnetic moment in a vertical magnetic field.* *9*

Figure 1.3. *Effect of diamagnetic shielding. The dotted ellipses represent motion of electrons in their orbitals under the influence of* $\mathbf{B}_0$........ *11*

Figure 1.4. *Structure and 250-MHz* ^{1}*H-NMR spectra of adenosine in* $DMSO\text{-}d_6$. *(Reproduced with permission from R. S. Macomber, A Complete Introduction to Modern NMR Spectroscopy, John Wiley & Sons, 1998).* *12*

Figure 2.1. *Model representation of a solute molecule in a cavity and the solvent as a continuum, which reacts on the molecular electric field by a reaction field.* *30*

Figure 4.1. *Model structures of substituted* A^{X8}–T^{Y6} *and* A^{X8}–U^{Y6} *base pairs, where X8, Y6=* NH^-, NH_2, NH_3^+ *(N series),* O^-, *OH,* OH_2^+ *(O series), F, Cl or Br (halogen series).* *40*

Figure 4.2. *Schematic representation of substituent effects on the hydrogen bonds in A-U. The proton transfer from U to A is labeled with a bold circle and occurs in (a) and (f).* *45*

Figure 4.3. *Calculated correlation between the C2-adenine shielding values (ppm) of isolated adenine* (A^{X8}) *bases and* A^{X8}*-T base pairs. The proton transfer systems were not included in the plot, due to their particular behavior.* *53*

Figure 4.4. *Calculated dependence of the NMR C2-shielding values (ppm) as a function of the hydrogen-bond strength* ($kcal{\cdot}mol^{-1}$)*.* ***(a)*** *C2-adenine shielding of* A^{X8}*-T,* ***(b)*** *C2-adenine shielding of A-*T^{Y6}*,* ***(c)*** *C2-thymine shielding of* A^{X8}*-T, and* ***(d)*** *C2-thymine shielding of A-*T^{Y6} *base pairs. The proton transfer systems were not included in the plot, due to their particular behavior.* *55*

Figure 4.5. *Structures of adenine, thymine and A-T base pair interacting with a* K^+ *cation and two water molecules.* *56*

Figure 4.6. *Calculated dependence of the NMR C2-adenine shielding values (ppm) as a function of the hydrogen-bond strength* ($kcal{\cdot}mol^{-1}$) *of the natural A-T, and the* $[K^+(N7)\cdots A\text{-}T]$, $[A\text{-}T\cdots K^+(O4)]$

and [A-T···K$^+$(O2)] model structures...57

Figure 5.1. *Structure of the trans-[PtCl$_2$(dma)PPh$_3$] complex.*..62

Figure 5.2*. Progress of the solution of the complex in* ***a)*** *DMSO-d$_6$**:**D$_2$O/H$_2$O monitoring by ^{31}P-NMR at 30m (in blue), 2.5h (in red), and 24h (in green) and* ***b)*** *DMSO-d$_6$ (200µl) and 300µl of D$_2$O/H$_2$O/acetone (23%/66%/11%).*..66

Figure 5.3. *Structures of selected trans-platinum(II) complexes optimized at the PBE-D/TZ2P level with COSMO.*..67

Figure 5.4. *Dynamically calculated ^{31}P-NMR shielding (σ) constants of the PH$_3$ and trans-[PtCl$_2$(dma)PPh$_3$] complex obtained with SO-ZORA (Gas-phase and aqueous solution)* ***(a-b)*** *and mDKS* ***(c-d)*** *relativistic corrections at the PBE (in blue) and KT2 (in orange) levels.*............72

Figure 5.5. *AIMD snapshots of trans-[PtCl$_2$(dma)PPh$_3$] explicit 3 and 5 water molecules and plotting the most important non-covalent interaction regions (in blue/green) using the NCI program. Total number of atoms in parentheses.*..73

Figure 5.6. *Dynamically calculated ^{31}P-NMR shielding constants σ (in ppm) of the trans-[PtCl$_2$(dma)PPh$_3$] with explicit water molecules obtained with SO-ZORA* ***(a-b)*** *and mDKS* ***(c-d)*** *relativistic corrections at the PBE (in blue) and KT2 (in orange) levels.*..................................74

Figure 5.7. *Radial distribution function of the water* ***a)*** *oxygen and* ***b)*** *hydrogen atoms around Pt a for the solvated trans-[PtCl$_2$(dma)PPh$_3$] complex. The arrows describe the statistical presence of a weakly bound water along the axis perpendicular to the square-planar Pt complex.* 75

Figure 5.8. *Comparison of the static and dynamic ^{31}P-NMR chemical shifts of the parent trans-[PtCl$_2$(dma)PPh$_3$] complex calculated using SO-ZORA and mDKS relativistic corrections at the PBE and KT2 levels. The experimental value is indicated by a dashed line.*...........................77

Figure 6.1. *Structure of o-benzyne.*..82

Figure 6.2. *Hemicarcerands* ***1*** *and* ***2*** *with a guest* ***G*** *in its interior.*...83

Figure 6.3. *Guest structures divided into classes A-F*..86

Figure 6.4. *Optimized structures of o-benzyne guest along* ***a)*** *long axis and* ***b)*** *equatorial axis of hemicarcerand* ***2****.*..95

Figure 7.1*. Inverse sandwich structures of* ***a)*** *cationic [E-Cp-E’]$^+$ (E and E’= B-Tl),* ***b)*** *neutral [E-C$_4$H$_4$-E] (E= Al-Tl) and* ***c)*** *global minimum E$_2$C$_4$H$_4$ (E = Al-Tl) as proposed by Liu et al.*......99

Figure 7.2. *Lowest-lying structures of the B$_2$P$_4$ cluster computed at the S12h/TZ2P level. Relative energies are given in kcal·mol^{-1}. In parentheses are the B-B bond lengths in Å. All structures are local minima on its corresponding PES, except* ***1j****, which is a transition state.*............................103

Figure 7.3*. Structure of [(HOMO)+(HOMO-1)] and [(HOMO)-(HOMO-1) of the B$_2$P$_4$ (D$_{2d}$)*

cluster....103

Figure 7.4. *Lowest-lying structures of the E_2P_4 (E= Al-Tl) clusters computed at the S12h/TZ2P level. Relative energies are given in kcal·mol^{-1}. [a]This structure does not converge. [b]In parentheses are the number of imaginary frequencies. [c]This structure converges to the* ***2b*** *isomer.* 104

Figure 7.5. *Chemical bonding pictures of E_2P_4 (E= B, Al, Ga, In and Tl) revealed by the AdNDP analysis. The AdNDP analysis was performed at PBE0/LANL2DZ level.* 106

Figure 7.6. *Qualitative correlation diagram for the D_{4h} [E-P_4-E] (E= B-Tl) complexes*............108

Figure 7.7. *Energetic reaction cycle involving the isomerization of the E_2P_4 clusters (E= B-Tl) between D_{4h} and D_{2d} structures.* 109

Figure 7.8. *Contributions to the isomerization energy for the E_2P_4 clusters (E= B-Tl) by using IEDA.* 110

Figure A1.1. *Calculated correlation between the C2-thymine shielding values (ppm) of isolated thymine (T^{Y6}) bases and A-T^{Y6} base pairs. The proton transfer systems were not included in the plot, due to its particular behavior.* 126

Figure A1.2. *Calculated dependence of the NMR C2-shielding values (ppm) as a function of the hydrogen-bond strength (kcal·mol^{-1}).* ***a)*** *C2-adenine shielding of A^{X8}-U,* ***b)*** *C2-adenine shielding of A-U^{Y6},* ***c)*** *C2-uracil shielding of A^{X8}-U, and* ***d)*** *C2-uracil shielding of A-U^{Y6} base pairs. The proton transfer systems were not included in the plot, due to its particular behavior*.............................127

Figure A2.1 *a) ^{1}H-NMR, b) HSQC [^{1}H-^{13}C] NMR and c) ^{31}P-NMR spectra of the complex in DMSO d_6 (200µl) and 300µl of D_2O/H_2O (90%/10%) after 30m.* 128

Figure A3.1. *Most stable structures of hemicarceplexes (**1@G**) optimized at the PBE-D/TZ2P level.* 131

Figure A3.2. *Structure of (**1@o-benzyne**) optimized at the PBE-D/TZ2P level.*..........................134

List of Tables

Table 4.1. *Hydrogen-bond lengths (Å) and bond energies ΔE_{Bond} (kcal·mol^{-1}) for A^{X8}-T^{Y6} and A^{X8}-U^{Y6} base pairs^{a}*...43

Table 4.2. *EDA analysis (in kcal·mol^{-1}) of the A^{X8}-U^{Y6} base pairs (N and O series)^{a}*...47

Table 4.3. *EDA analysis (in kcal·mol^{-1}) of the A^{X8}-U^{Y6} base pairs using interacting fragments that involves the H3-proton transfer^{a}*...48

Table 4.4. *EDA analysis (in kcal·mol^{-1}) of the A^{X8}-U^{Y6} base pairs (halogen series)^{a}*...49

Table 4.5. *VDD atomic charges Q_A (a.u.) in the front atoms and the adenine/uracil C2 carbon atoms of the A^{X8}-U^{Y6} base pairs.*...50

Table 4.6. *NMR C2-adenine shielding (σ) values (ppm) computed at the SAOP/TZ2P level for the isolated adenine (A^{X8}) bases and A^{X8}-T base pairs^{a}*...52

Table 4.7. *NMR C2-thymine shielding (σ) values (ppm) computed at the SAOP/TZ2P level for the isolated thymine (T^{Y6}) bases and A-T^{Y6} base pairs^{a}*...54

Table 4.8 *NMR C2-adenine/thymine shielding (σ) values (ppm) computed at the SAOP/TZ2P level for adenine, thymine and A-T base pair interacting with a K^+ cation and two water molecules^{a}*..57

Table 5.1. *Basis-set dependence of mDKS relativistic corrections to the ^{31}P-NMR nuclear shielding constants and chemical shifts (in ppm) of the parent trans-[$PtCl_2$(dma)PPh_3] complex.*...68

Table 5.2. *Basis-set dependence of ZORA relativistic corrections (SR and SO) to the ^{31}P-NMR nuclear shielding constants and chemical shifts (in ppm) of the PH_3 and trans-platinum(II) complexes using the PBE functional.*...69

Table 5.3. *Static ^{31}P-NMR chemical shifts of the trans-platinum(II) complexes calculated with selected methods and using the PH_3 correction (85% aqueous H_3PO_4), see Eq. 5.1.*...71

Table 5.4. *Static and dynamic ^{31}P-NMR shielding constants (σ) of PH_3 and the parent trans-[$PtCl_2$(dma)PPh_3] complex and ^{31}P-NMR chemical shifts (δ) of the parent complex.*...76

Table 6.1. *Calculated and experimental ^{1}H-NMR chemical shifts (δ) of free and incarcerated guests and their spectra changes in the chemical shifts of guest protons caused by incarceration (Δδ).*..87

Table 6.2. *Modified results of the calculated and experimental ^{1}H-NMR chemical shifts (δ) for selected class B guests.*...90

Table 6.3. *Calculated and experimental ^1H-NMR chemical shifts (δ) of free and incarcerated hosts* ***1@G*** *(δ), and their chemical shift changes (Δδ) relative to free host* ***1****.* 92

Table 6.4. *Comparison between the calculated and experimental ^1H and ^{13}C-NMR chemical shifts in o-benzyne (ppm).*...93

Table 7.1. *Results of the EDA for the* ***2a*** *(D_{4h}) structure in [E-P_4-E] (E= B-Tl) complexes. The interacting fragments are $(E\cdots E)^{2+}$ and P_4^{2-}. Energy values are in kcal·mol^{-1}.* 107

Table 7.2. *Results of IEDA at the S12h/TZ2P level for the E_2P_4 (E = B, Al, Ga, In, Tl) clusters with E_2^{2+} and P_4^{2-} fragments for the $D_{4h} \rightarrow D_{2d}$ isomerization reaction. Energy values are in kcal·mol^{-1}.* 110

Table 7.3. *The second, third and fifth columns collect the results of I_{NB} aromaticity index (values multiplied by 1000) for the E_2P_4 (E= Al, Ga, In, Tl) D_{4h} and D_{2d} clusters. Global values (E_2P_4) and the local values for the P_4^{2-} unit (for comparison the free P_4^{2-} value is 53) for the D_{4h} conformer are collected. The fourth column contains the delocalization index between P_4^{2-} unit and the E_2^{2+} fragment.* 111

Table 7.4. *^{31}P-NMR shielding values (ppm) computed at the KT2/ET-pVQZ level for the D_{4h} and D_{2d} isomers of the E_2P_4 clusters.*..112

Table A1.1. *VDD atomic charges in the front atoms and the adenine/thymine C2 carbon atoms of the A^{X8}-T^{Y6} base pairs.* 124

Table A1.2. *VDD atomic charges in the front atoms and the adenine/uracil C2 carbon atoms of the A^{X8}-U^{Y6} base pairs.*...125

Table A1.3. NMR C2-adenine shielding (σ) values (ppm) computed with SAOP/TZ2P level for the isolated adenine (AX8) bases and AX8-U base pairs.[a...125

Table A1.4. *NMR C2-adenine shielding (σ) values (ppm) for the isolated adenine $(A^{X8})^{[a]}$ and the A^{X8}//A^{X8}-$T^{[b]}$ bases computed with SAOP/TZ2P level.* 126

Table A2.1. *Basis-set dependence of ZORA relativistic corrections (SR and SO) to the ^{31}P-NMR nuclear shielding constants and chemical shifts (in ppm) of the phosphine and trans-platinum(II) complexes using the KT2 functional.* 129

List of Abbreviations

AdNDP	Adaptive natural partitioning analysis
AIMD	*ab-initio* Molecular Dynamic
A-T	Adenine-Thymine
A-U	Adenine-Uracil
CCSDT	Coupled Cluster
CDFT	Current Density Functional Theory
DFT	Density Functional Theory
DIEs	Deuterium isotope effects
DMSO	Dimethyl sulfoxide
EDA	Energy Decomposition Analysis
GIAO	Gauge-Including Atomic Orbitals
G-U	Guanine-Cytosine
KS	Kohn-Sham
NCI	Non-covalent Interaction plots
NMR	Nuclear Magnetic Resonance
MD	Molecular Dynamic
mDKS	Matrix Dirac-Kohn-Sham
QM	Quantum mechanical
SO	Spin-orbit coupling
SR	Scalar relativistic effect
TF	Thomas-Fermi
TMS	Tetramethylsilane
VDD	Voronoi deformation density
ZORA	Zeroth-order Regular Approximation

Acknowledgments

This thesis is the product of some four years of work, conducted mostly at the Institut de Química Computacional i Catàlisi (IQCC), at the Universitat de Girona. I owe my deep gratitude to my supervisor, Marcel Swart, not only for the scientific knowledge, but also for all the opportunities I was given to conduct my research. Also, I would like to thank my colleagues from the IQCC for their wonderful collaboration. You supported me greatly and were always willing to help me.

I would like to thank to all the collaborators of this work, specially to Trygve Helgaker, Heike Fliegl, Michele Cascella, and Célia Fonseca Guerra, for their valuable guidance during my research stays abroad. I also thank to the reviewers of this thesis, for their work and useful suggestions.

I thank for financial support to the following organizations: Ministry of Economy and Competitiveness of Spain (MICINN), National Council on Science and Technology of Mexico (CONACyT), and the CANIOC joint exchange programme, funded by the European Seventh Framework Programme through the Marie Curie Actions.

Special thanks to the Institut de Química Computacional i Catàlisi (IQCC), MareNostrum & RES, and Norwegian Supercomputing Program (NOTUR) for the computational resources.

Table of Contents

Summary 1
Resum 2
Resumen.. 3
Chapter 1. Introduction.. 5
1.1 Computational NMR spectroscopy 7
1.1.1 Basic theory of NMR... *7*
1.1.2 A brief account of the chemical shift.. *9*
1.1.2.1 Definition 9
1.1.2.2 Theory of chemical shifts 10
1.2 Computational aspects 12
1.2.1 Drawback of theoretical models *13*
1.2.2 Additional medium effects.. *14*
1.2.3 Relativistic effects *15*
Chapter 2. Methodology.. 17
2.1 Density functional theory 19
2.1.1 The Hohenberg-Kohn Theorems... *20*
2.1.2 The Kohn-Sham formulation... *21*
2.1.3 Relativistic DFT *23*
2.1.3.1 The Dirac equation... 23
2.1.3.2 The Breit-Pauli approximation 24
2.1.3.3 The Zeroth Order Regular Approximation (ZORA)............................ 25
2.1.3.4 Four-component methods 26
2.2 Calculation of NMR parameters... 27
2.2.1 Theoretical background.. *27*
2.3 Simulation techniques.. 29
2.3.1 Continuum Solvent Models *30*
2.3.2 Molecular dynamic simulations... *31*
Chapter 3. Objectives 35
Chapter 4. The influence of substituents and the environment on the NMR shielding constants of supramolecular complexes based on A-T and A-U base pairs 37
4.1 State of the art.. 39
4.2 Computational Methods 41
4.2.1 Energy decomposition analysis setup *41*

4.3 Results and Discussion 42
4.3.1 Substituent effects on the model structures *42*
4.3.2 Origin of the Substituent Effects *46*
4.3.3 NMR Chemical Shielding Constants *51*
Chapter 5. Four-component relativistic ^{31}P-NMR calculations in *trans*-platinum(II) complexes: Importance of the solvent and dynamics in spectral simulations 59
5.1 State of the art 61
5.2 Computational Details 62
5.2.1 Treatment of the Solvent Effects *64*
5.3 Results and Discussion 65
5.3.1 Experimental NMR studies of the trans-[PtCl$_2$(dma)PPh$_3$] complex in solution *65*
5.3.2 Static ^{31}P-NMR chemical shift calculations *66*
5.3.3 Solvent effects in the ^{31}P-NMR shielding constants *71*
5.3.4 Explicit treatment of the solvent *73*
5.3.5 ^{31}P-NMR Chemical Shift Analysis *76*
Chapter 6. Computational NMR Spectroscopy for host-guest Hemicarcerands. 79
6.1 State of the art 81
6.2 Computational Details 83
6.3 Results and Discussion 84
6.3.1 Guest molecules inclusion within hosts *85*
6.3.2 Chemical shifts of incarcerated hosts ***1@G*** *91*
6.3.3 Encarceration of o-benzyne *93*
Chapter 7. Exploring the potential energy surface of E$_2$P$_4$ clusters (E= Group 13 elements): The quest for inverse carbon-free sandwiches 97
7.1 State of the art 99
7.2 Computational Methods 100
7.3 Results and Discussion 102
7.3.1 Structures *102*
7.3.2 Adaptive natural density partitioning analysis *105*
7.3.3 Energy decomposition analysis *106*
7.3.4 Isomerization energy decomposition analysis *108*
7.3.5 Global and local aromaticity *110*
7.3.6 ^{31}P-NMR shielding constants *111*
Chapter 8. General Conclusions 113
References 115
Appendices 123

Summary

Nuclear Magnetic Resonance (NMR) spectroscopy is an indispensable structural tool in the modern analytical arsenal of chemists and structural biologists. Certainly, the synergy between computational and experimental methods in NMR spectroscopy is a powerful approach since it allows to combine the experimental precision with the predictive and explanatory power of theoretical methods, yielding new insight unachievable by the experimental or theoretical approaches alone. However, despite the advances attained in theoretical chemistry methods, the accuracy with which the NMR shift constants can be obtained depends on several factors and a protocol for these calculations is not always well established and understood.

The present thesis is a computational study of the NMR shift constants in a number of chemical systems of interest, using both *static* and *dynamic* approaches via Density Functional Theory, to predict, confirm the presence of transient species, and/or explain ambiguous signals in the NMR spectra. Special attention was put on cases where there are strong interactions between the solvent and the molecule studied. The most accurate calculations of this type involve the use of molecular dynamics simulations to provide typical solvent configurations in an atomistic and dynamic detail, and it can be combined with quantum mechanical calculations to determine the NMR chemical shifts in liquid state conditions.

In addition, this thesis addresses other methodological issues that influence the quality of the calculated NMR chemical shifts such as the level of theory, the explicit inclusion of solvent molecules, the choice of the reference molecule, as well as the relativistic effects for heavy element compounds.

Resum

L’espectroscòpia de Ressonància Magnètica Nuclear (RMN) és una eina indispensable en el modern arsenal de químics analítics i biòlegs estructurals. Indubtablement, una pràctica poderosa en espectroscòpia de RMN és l'ús de tots dos mètodes computacionals i experimentals, ja que permet combinar la precisió experimental amb el poder predictiu i explicatiu dels mètodes teòrics, aconseguint així una percepció que seria inabastable només per mètodes experimentals o teòrics . No obstant això, malgrat els avenços aconseguits en química teòrica, la precisió amb la qual es poden obtenir els desplaçaments químics de RMN depèn de diversos factors i no sempre es té ben establert i entès un protocol per al seu estudi.

La present tesi és un estudi computacional dels desplaçaments químics de RMN en un nombre de compostos químics d’interès, usant aproximacions *estàtiques* i *dinàmiques* mitjançant la teoria del funcional de la densitat, la qual ajudarà a predir, a confirmar i/o a complementar dades obtingudes experimentalment. S’ha donat especial atenció en casos on existeixen fortes interaccions substrat-solvent. Aquest tipus de càlculs tan precisos impliquen l’ús de metodologies més rigoroses, com la inclusió de simulacions de dinàmica molecular per a proveir en detall les típiques configuracions d’un solvent i que, en combinar-se amb càlculs de mecànica quàntica, permeten determinar els desplaçaments químics de RMN en condicions d’estat líquid.

Addicionalment, aquesta tesi aborda altres problemes metodològics que afecten la qualitat dels desplaçaments químics teòrics com el nivell de teoria, la inclusió explícita de molècules de solvent, l’elecció de la molècula de referència, així com els efectes relativistes en compostos que contenen àtoms pesats.

Resumen

La espectroscopia de Resonancia Magnética Nuclear (RMN) es una herramienta indispensable en el moderno arsenal de químicos analíticos y biólogos estructurales. Indudablemente, una práctica poderosa en espectroscopia de RMN es el uso de ambos métodos computacionales y experimentales, ya que permite combinar la precisión experimental con el poder predictivo y explicativo de los métodos teóricos, logrando así una percepción que sería inalcanzable solamente por métodos experimentales o teóricos. Sin embargo, a pesar de los avances logrados en química teórica, la precisión con la cual se pueden obtener los desplazamientos químicos de RMN depende de diversos factores y no siempre se tiene bien establecido y comprendido un protocolo para su estudio.

La presente tesis es un estudio computacional de los desplazamientos químicos de RMN en un número de compuestos químicos de interés, usando aproximaciones *estáticas* y *dinámicas* mediante la Teoría del Funcional de la Densidad lo cual ayudará a predecir, confirmar y/o complementar datos obtenidos experimentalmente. Se ha dado especial atención en casos donde existen fuertes interacciones substrato-disolvente. Este tipo de cálculos tan precisos implican el uso de metodologías más rigurosas, como la inclusión de simulaciones de dinámica molecular para proveer en detalle las típicas configuraciones de un disolvente y que, al combinarse con cálculos de mecánica cuántica, permiten determinar los desplazamientos químicos de RMN en condiciones de estado líquido.

Adicionalmente, esta tesis aborda otros problemas metodológicos que afectan la calidad de los desplazamientos químicos teóricos como el nivel de teoría, la inclusión explicita de moléculas de disolvente, la elección de la molécula de referencia, así como los efectos relativistas en compuestos que contienen átomos pesados.

Chapter 1

Introduction

SUMMARY

In this chapter, we introduce a brief description of the general theory behind the NMR spectroscopy and the fundamental quantum mechanical methods that are used to compute the NMR chemical shifts.

1.1 Computational NMR Spectroscopy

Nuclear Magnetic Resonance (NMR)[1] is the study of molecular structure through measurement of the interaction of an oscillating radio-frequency electromagnetic field with a collection of nuclei immersed in a strong external magnetic field. These nuclei are parts of atoms that, in turn, are assembled into molecules. An NMR spectrum, therefore, can provide detailed information about molecular structure and dynamics, information that would be difficult, if not impossible, to obtain by any other method.

It was in 1902 that physicist P. Zeeman shared a Nobel Prize for discovering that the nuclei of certain atoms behave strangely when subjected to a strong external magnetic field. And it was exactly 50 years later that physicists F. Bloch and E. Purcell shared a Nobel Prize for putting the so-called nuclear Zeeman effect to practical use by constructing the first crude NMR spectrometer. During the succeeding years, NMR has completely revolutionized the study of chemistry and biochemistry, not to mention having a significant impact on a host of other areas.

Nuclear magnetic resonance is probably the single most widely applied spectroscopic technique in modern chemical research for elucidation of molecular structure.

1.1.1 Basic theory of NMR

The physics behind NMR signals is based on the observation that atomic nuclei have a quantum mechanical property called ***nuclear spin***. Because the nuclear proton is a charged particle (Z= 1), this spinning gives rise to a ***magnetic moment*** (μ) represented by the boldface vector arrows in Figure 1.1. For a proton, the nuclear spin quantum number (m), can assume two possible orientations of the magnetic moment vector in an external magnetic field, “up” (in the same direction as the external field) or “down” (in the opposite direction to the external field). These two spin states are degenerate in the absence of an external magnetic field. However, when unpaired protons are immersed in an external field, the two states are no longer degenerate. We describe such a nucleus as having a ***nuclear spin*** (I) of ½.

Perhaps surprisingly, neutrons also exhibit a magnetic moment and a nuclear spin of I=1/2, even though they are uncharged. Therefore, they too can adopt two different

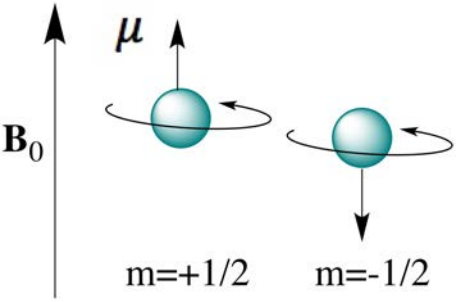

Figure 1.1. Two possible orientations of the magnetic moment of a spinning proton in an external magnetic field.

orientations in a magnetic field, where the more stable orientation corresponds to m=-1/2. The value of the spin (I) of any given nucleus depends on the mass number and the atomic number of the nucleus. Certain atomic nuclei (those with an odd number of protons, and/or an odd number of electrons) possess non-zero nuclear spin. Nuclei with zero nuclear spin have zero nuclear magnetic moment and cannot be detected by NMR methods.

As complex nuclei can adopt more than two magnetic spin orientations, a nucleus of spin I has 2I+1 possible nondegenerate spin orientations in a magnetic field. The energy of the ith spin state (E_i) is directly proportional to the value of m_i and the magnetic field strength $\mathbf{B}_0$ (that is, energy is quantized in units of $\gamma h\mathbf{B}_0/2\pi$):

$$E_i = -m_i \frac{\gamma h \boldsymbol{B}_0}{2\pi} \tag{1.1}$$

In Eq. (1.1) Planck's constant h, and π have their usual meanings, while γ is called the ***magnetogyric ratio***, a proportionality constant characteristic of the isotope being examined. Figure 1.2 graphically depicts the variation of spin state energy as a function of magnetic field strength for two different nuclei, one with I=1/2, the other with I=1. Notice that as field strength increases, the difference in energy (ΔE) between any two spin states also increases proportionally.

Magnetic moments are actually not statically aligned exactly parallel or antiparallel to the external magnetic field, as Figure 1.2 implied. Instead, they are forced to remain at

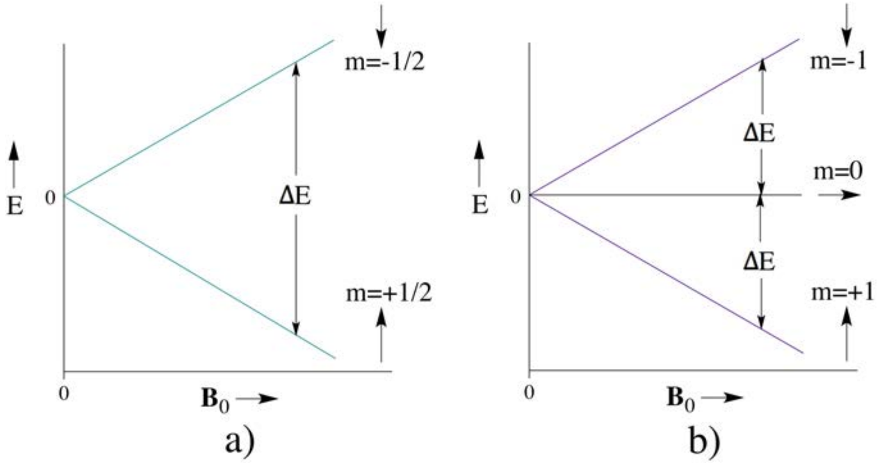

Figure 1.2. Nuclear Zeeman effects. a) A nucleus with *I*=1/2. b) A nucleus with *I*=1. The arrow beside each spin line indicates the orientation of the magnetic moment in a vertical magnetic field.

a certain angle to $\mathbf{B}_0$, and this causes them to "wobble" around the axis of the field at a fixed frequency. This periodic wobbling motion is called precession. Thus, the magnetic moment vector of a nucleus in a magnetic field precesses with a characteristic angular frequency called the Larmor frequency (ω), which is a function solely of γ and $\mathbf{B}_0$:

$$\omega = \gamma \boldsymbol{B}_0 \tag{1.2}$$

The angular Larmor frequency, can be transformed into linear frequency v by division by 2π:

$$v_{precession} = \frac{\omega}{2\pi} = \frac{\gamma \boldsymbol{B}_0}{2\pi} \tag{1.3}$$

1.1.2 A brief account of the chemical shift

1.1.2.1 Definition

The fundamental quantity underpinning the phenomenon of the chemical shift of a nucleus is its magnetic shielding tensor, σ. The isotropic average, σ_{iso}, is the shielding or deshielding of the nucleus in the substrate with respect to the bare nucleus *in vacuo.*

Although this property cannot be observed directly, the difference in shielding constants between two nuclei in different environments can be observed. The chemical shift, δ, is such a difference, namely that between the probe nucleus and the same nucleus in a reference (standard) compound such as tetramethylsilane (TMS). In gases or liquid media, only the isotropic average can be observed, which is, to a good approximation,

$$\delta = \delta_{iso} = \sigma_{iso}(standard) - \sigma_{iso} \tag{1.4}$$

where σ_{iso}(standard) is the isotropic shielding of the nucleus of interest in the reference compound.

1.1.2.2 Theory of chemical shifts

The electron cloud surrounding each nucleus in a molecule serves to shield that nucleus from the external magnetic field. Figure 1.3 depicts a comparison between a bare proton and one shielded by an electron cloud. The external magnetic field ($\mathbf{B}_0$ in Figure 1.3) causes each electron pair surrounding the nucleus to circulate through its orbital in such a way as to generate an induced magnetic field ($\mathbf{B}_i$) opposed to the external field. As a result, while a bare proton experiences the full magnitude of the external field, the shielded nucleus experiences an effective field ($\mathbf{B}_{\mathrm{eff}}$) that is equal to the external field minus the induced field:

$$\boldsymbol{B}_{eff} = \boldsymbol{B}_0 - \boldsymbol{B}_i \tag{1.5}$$

Because the strength of the induced field is directly proportional to that of the external field, we can define a shielding constant σ that is a function of the exact molecular (*i.e.*, electronic) environment of the nucleus:

$$\boldsymbol{B}_i = \sigma \boldsymbol{B}_0 \tag{1.6}$$

The value of σ is dimensionless and field independent. Substituting into Eq. (1.3) gives:

$$v_{precession} = \frac{\gamma(1-\sigma)\boldsymbol{B}_0}{2\pi} \tag{1.7}$$

Thus, the greater the shielding of the nucleus (the larger the value of σ), the lower

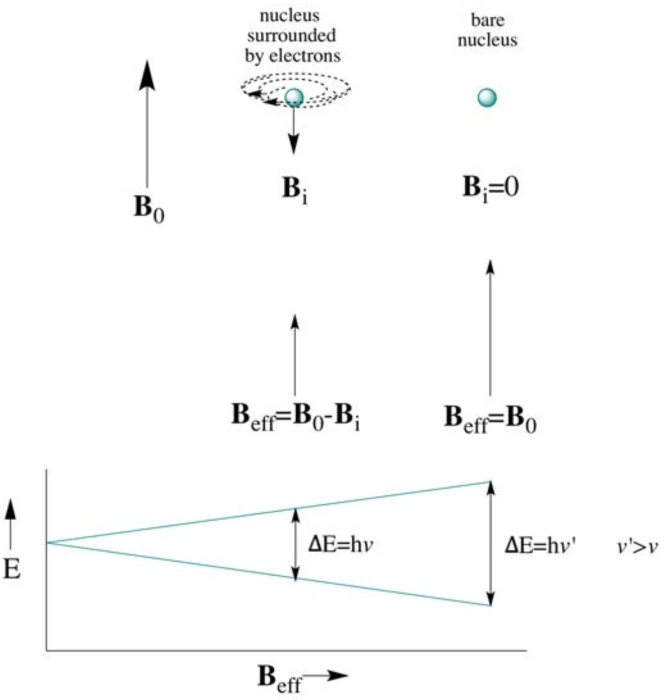

Figure 1.3. Effect of diamagnetic shielding. The dotted ellipses represent motion of electrons in their orbitals under the influence of $\mathbf{B}_0$.

will be its resonance frequency and the farther to the right it will be its resonance frequency and the farther to the right it will appear in an NMR spectrum. Conversely, nuclei from which electron density has been withdrawn (resulting in smaller σ) are said to be deshielded and appear toward the left of the spectrum (higher frequency).

The type of shielding and deshielding that we have discussed is a consequence of the isotropic (spherically symmetric) distribution of paired electrons and is referred to as *diamagnetic shielding*. In the case of heavier atoms there can also be a nonsymmetrical (anisotropic) distribution of valence electrons, and circulation of these electrons in a magnetic field gives rise to an induced field aligned with the external field. This is called *paramagnetic shielding*. Thus, the net σ value for an atom includes both terms, $\sigma_{\text{diamagnetic}} - \sigma_{\text{paramagnetic}}$, and is proportional to the electron density around the nucleus.

In case of hydrogen, diamagnetic shielding is the predominant term. But for other nuclei (*e.g.* carbon, fluorine, and phosphorus) paramagnetic shielding becomes

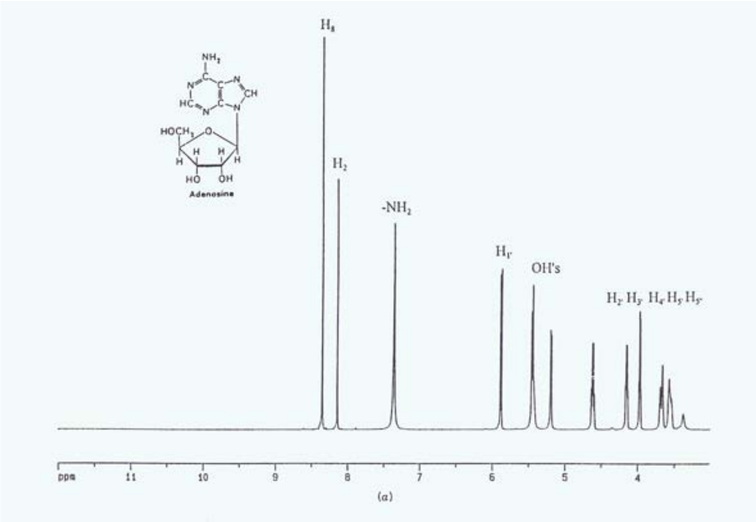

Figure 1.4. Structure and 250-MHz ^{1}H-NMR spectra of adenosine in DMSO-d_6. (Reproduced with permission from R. S. Macomber, *A Complete Introduction to Modern NMR Spectroscopy*, John Wiley & Sons, 1998).

increasingly important.

NMR techniques can thus be used to ascertain the nature of the binding of small molecules to large proteins. Although initial studies involved the simplest of systems, similar analyses have since been applied to a wide variety of more complex systems. For example, the structure and ^{1}H-NMR spectrum of adenosine in DMSO-d_6 is shown in Figure 1.4. The base protons of the purine ring appear downfield at ~δ 8 ppm, the NH_2 protons at δ 7.4 ppm, $H_{1'}$ of the sugar at δ 5.9 ppm, the hydroxyl protons between δ 5.5 and 4.5 ppm, and the remaining ribose protons ($H_{2'}$, $H_{3'}$, $H_{4'}$, $H_{5'}$ and $H_{5''}$)between δ 4.3 and 3.0 ppm.

1.2 Computational aspects

The most important application of NMR calculations is, arguably, their help in structural elucidation. While proton (^{1}H) and ^{13}C shielding constants hold a prominent place in organic chemistry, other magnetic nuclei such as ^{15}N, ^{19}Si, or ^{31}P but also heavier nuclei such as transition-metals are increasingly important in many areas of chemistry.[2]

Obviously, all these nuclei are equally amenable to computational investigations. However, some methodological questions are still left to be answered concerning the scopes and limitations of the quantum chemical methods.

Thus, in the following section we will give an overview of the level of confidence that can be expected for NMR shielding constants computed for the various relevant magnetic nuclei using different methodologies and implementations. It is important to mention that the computed magnetic properties are in general extremely sensitive to the geometry chosen. This applies in particular to chemical shifts calculations where even small changes in bond lengths or angles may lead to significant deviations in the chemical shifts. Hence, reliable chemical shifts can only be expected if these calculations are based on good geometries.

1.2.1 Drawback of theoretical models

As mentioned before, advances have been made with theoretical chemistry methods for finding accurate reproductions of experimentally observed NMR shift constants.[3] These can nowadays be obtained using both high-level coupled cluster (CCSD(T))[4] and density functional methods.[5-10] However, the accuracy with which the shift constants can be obtained depends on several factors, and is not uniformly accurate for all nuclei. There have been numerous studies investigating the accuracy of density functionals for the calculation of NMR parameters typically through critical comparison of computed and experimental values for selected test sets of molecules. For instance, several studies in a wide range of molecules showed for ^{1}H nuclei a high accuracy of less than 1 ppm difference between theory and experiment.[5-7] In contrast, for ^{13}C and ^{15}N these accuracies are somewhat less (3-10 ppm), depending on the method and basis set used.[11]

Although there appears to be no agreement on a single best functional, hybrid functionals such as the popular B3LYP variant tend to performed somewhat better than their nonhybrid counterparts. On the other hand, Xu *et al.*[12,13] investigated a number of density functional methods and found that the OPBE functional performs remarkably well. Likewise, Zhao and Truhlar[10] found that the M06-L functional gives even smaller deviations than OPBE and is as good as the Keal-Tozer functionals (KT1 and KT2).[6] These latter two functionals were specially designed to provide high-quality shielding constants for light main-group nuclei.

Moreover, special attention needs to be paid to the basis set employed. The basis set needs to be able to adequately describe the electron density close to the nuclei. Several schemes have been devised to modify existing basis sets for this purpose. These usually involve decontracting basis functions (to make the basis sets more flexible) and adding tight functions (to improve the description of the electron density near the nuclei).

1.2.2 Additional medium effects

The overwhelming majority of NMR calculations is carried out for static structures, *i.e.* actually vacuum conditions are modeled, when there are no collisions and interactions with other molecules. Thus, theoretically calculated NMR shift values must be compared with experimental values determined in the gas phase. This raises the question of how the data obtained in the gas phase will apply to solutions and if it is correct to compare chemical shifts calculated in gas phase with experimental NMR data obtained in solution.

Thus, for a better compatibility with experiments conducted at ambient temperature and solution, effects of thermal motion and solvation can be included in the computations. Classical thermal effects can be modeled computationally by performing molecular dynamics (MD) simulations and averaging the computed NMR parameters over a sufficient number of snapshots from the trajectories.[14] Methods to evaluate quantum-mechanical zero-point corrections have also been devised.[15] Such thermal effects on NMR parameters tend to be rather small for the lighter nuclei such as ^{1}H and ^{13}C and more noticeable for heavier nuclei such as transition metals.[16]

Additionally, the perturbation of NMR parameters due to the solvent effects can be modeled in computational with continuum models to simulate dielectric solvent effects.[17] Many studies have used continuum models to calculate shielding constants,[18-20] especially important are those of Ruud and coworkers.[21] However, for polar protic solvents such as water, the specific hydrogen-bonding interactions are not captured by this approach, and specific solute-solvent interactions need to be included.

1.2.3 Relativistic effects

Electrons in heavy element compounds move so fast that relativistic effects become important. Chemical and physical properties of atoms and molecules are predicted differently with a relativistic and non-relativistic theory. Only the former is adequate for heavy element systems. Thus, it is not surprising that the relativistic effects can have a particularly strong impact on calculated NMR parameters.[22]

Relativistic effects are usually separated into spin-orbit coupling (SO) interactions and scalar relativistic (SR) effects, where the SR are relativistic effects at the one-electron level and the SO are relativistic effects that affect the electron-electron interactions in many-electron systems. There are many fully and quasi-relativistic methods available for quantum chemical calculations. For instance, all-electron relativistic quantum chemical calculations can be carried out with a Hamiltonian that only includes SR terms or including both SR and SO. The latter approach is in principle more accurate.[23] For example, a DFT-NMR code for molecules that includes both scalar and spin-orbit relativistic effects is based on the zero-order regular approximation (ZORA) two-component Hamiltonian.[24-26] In recent years, relativistic Gauge-Including Atomic Orbitals (GIAO) NMR chemical shift calculations have been successfully applied to a variety of molecules containing transition metal atoms and have become a routine tool for understanding their chemistry.[27]

Despite the success of the GIAO method in general, the modelling of heavy nuclei chemical shifts with DFT has met with some difficulties. Autschbach and Le Guennic have studied platinum chemical shifts using DFT, with a focus on solvent effects. These authors found it difficult to determine accurate chemical shifts and further showed that, in many cases, calculations require consideration of explicit solvation shells in addition to an implicit solvation model to describe the bulk solvation effects. Moreover, Bühl and co-workers have applied MD simulations extensively to successfully determine the chemical shifts for metal complexes. Calculations of the metal chemical shifts for a number of Fe,[28,29] Mn,[30] V,[31] and Co[32] complexes showed sizable solvent effects.

In particular, the calculation of metal NMR parameters in solution requires elaborate computational models.[23,33-36] However, this challenge also provides a great opportunity to obtain important new information about how solvation influences the structure of a metal complex and how such structural effects combined with the presence of solvent, in turn, influence the NMR parameters of the metal center.

Chapter 2

Methodology

SUMMARY

In this chapter, we introduce the general strategies to compute magnetic properties via density functional theory (DFT). The first section briefly reviews the theoretical background concerning the DFT method applied in this research. In addition to presenting the general methodological aspects, the discussion will be extended in section 2.1.3 to relativistic corrections which represent a considerable challenge for any method and where DFT seems to be particularly successful and sometimes the only choice.

In section 2.2, is an overview of the technical issues associated with our aim objective in this thesis, that is the calculation of NMR chemical shifts. Here, basic aspects of the theoretical background to compute NMR are explained in detail.

Next, we will discuss considerations concerning the simulation techniques. An overview of the continuum solvent models and the molecular dynamic simulations is given in section 2.3. In this case, we provide a more qualitative introduction which aims to understand how the methods work and how well they perform in practical applications.

2.1 Density functional theory

The foundation for modern density functional theory, DFT, is based on the Hohenberg and Kohn[37] theorems which demonstrated that the energy of the system, as well as all other observables are determined completely by the electron density (ρ) of the system. No knowledge of the wave function is necessary, and thereby there is no need to solve the Schrödinger equation[38]

$$\hat{H}(\boldsymbol{r}_1,\ldots,\boldsymbol{r}_N)\psi(\boldsymbol{r}_1,\ldots,\boldsymbol{r}_N) = E\psi(\boldsymbol{r}_1,\ldots,\boldsymbol{r}_N) \tag{2.1}$$

where $\psi(\mathbf{r}_1,\ldots,\mathbf{r}_\mathrm{N})$ is the electronic wave function and $\hat{H}(\mathbf{r}_1,\ldots,\mathbf{r}_\mathrm{N})$ is the electronic Hamiltonian describing the motion of N electrons in the field of M nuclei,

$$\hat{H} = \sum_{i=1}^{N} -\frac{1}{2}\nabla_I^2 - \sum_{i=1}^{N}\sum_{a=1}^{M}\frac{Z_a}{R_{ia}} + \sum_{i=1}^{N}\sum_{j>i}^{M}\frac{1}{r_{ij}} \tag{2.2}$$

where ∇_i^2 is the Laplacian operator, R_{ia} is the distance between ath nucleus and i-th electron, r_{ij} is the distance between i-th and j-th electron, Z_a is the atomic number of nucleus a. The first term in the Eq. (2.2) is the operator of the kinetic energy of the electrons, the second term represents the coulomb attraction between electrons and nuclei and the last term stands for the electron-electron repulsion.

An exact solution for the wave function requires, in principle, a computational effort that scales exponentially with the number of electrons in the system. In contrast, an alternative to wavefunction based methods, DFT has become widely used over the past 30 years.[39] The equations of a perfect density functional should be solvable with an effort linear with the number of electrons. In practice, the development of the functionals is nowhere near this state of perfection. In certain cases the accuracy of DFT calculations is equal to those more computationally demanding quantum chemical calculations.[40]

The motivation for DFT is that the ground state properties of a system can be described by considering the ground state electron density. The density can be found from the electronic wavefunction $\psi(\mathbf{r}_1,\mathbf{r}_2,\ldots,\mathbf{r}_n)$ by

$$\rho(\boldsymbol{r}_1) = N\int \psi^*(\boldsymbol{r}_1,\boldsymbol{r}_2,\ldots,\boldsymbol{r}_n)\,\psi(\boldsymbol{r}_1,\boldsymbol{r}_2,\ldots,\boldsymbol{r}_n)d\boldsymbol{r}_2..d\boldsymbol{r}_n \tag{2.3}$$

This has an obvious advantage over the wavefunction approach; for an N electron system, the wavefunction is a complex function of $3N$ variables (or $4N$, if spin is included), while the charge density is a function of 3 (x, y, z) or 4 variables, respectively. The usefulness of DFT arises as the ground state properties of a system are determined by the ground state density, which is a unique function of the potential for a given number of electrons.

The first density functional actually appeared even before the Hartree-Fock method,[41,42] the basis for modern wave function based models. The *Thomas-Fermi (TF) model* was published already 1927 in two independent works.[43,44] Here, the energy was given by the kinetic energy of a uniform electron gas and the classical electrostatic interaction between the electrons and nuclei for an electron gas of a given energy. However, it soon became evident that the TF model had limited applicability due to the crude approximations that it contains, especially for the kinetic energy. During the years to come, improvements on the model were attempted, for example, by adding the exchange energy of the electrons from the work of Dirac.[45] It was the work of Kohn, Hohenberg, and Sham[37,46] that provided a route to useful calculations, which will be discussed in the following sections. Whereas the TF approach involves the electron density only, the Kohn-Sham (KS) approach reintroduced one-electron orbitals. These can be found from solving one-electron equations involving an orbital-dependent kinetic energy functional and a local effective potential.

2.1.1 The Hohenberg-Kohn Theorems

Hohenberg and Kohn formulated DFT as an exact theory of many-body systems. DFT is based in the two theorems:

Theorem 1. Every observable of a stationary quantum mechanical system (including energy), can be calculated, in principle exactly, from the ground-state density alone, i.e., every observable can be written as a functional of the ground-state density ρ_0.

Thus, the ground state energy of a system E_0, is a unique functional of the ground state density. $E_0 = E\left[\rho_0(\mathbf{r})\right]$

Theorem 2: The functional for the ground state energy is minimized by the ground state electron density. The energy of the system is minimum when the exact density of the system ρ_0 is considered.

$$E[\rho] \geq E[\rho_0] \tag{2.4}$$

Applying this, E_0 can be found by minimizing $E[\rho]$ with a variational method:

$$E[\rho] = F_{HK} + \int v_{ext}(\boldsymbol{r})\, \rho(\boldsymbol{r}) d\boldsymbol{r} \tag{2.5}$$

where v_{ext} stands for the external potential which represents the electron-nuclei attraction:

$$v_{ext} = \sum_{a=1}^{M} \frac{Z_a}{|\boldsymbol{R}_a - \boldsymbol{r}|} \tag{2.6}$$

Z_a is the charge of an a-th nucleus (atomic number), $|\mathbf{R}_a - \mathbf{r}|$ is the distance between a given electron and the nucleus a.

F_{HK} is a universal function of electron density, which depends on the kinetic energy $T[\rho]$, the classical Coulomb energy $J[\rho]$, and on the non-classical electron-electron interaction energy $E_{NC}[\rho]$:

$$F_{HK}[\rho] = T[\rho] + J[\rho] + E_{NC}[\rho] \tag{2.7}$$

2.1.2 The Kohn-Sham formulation

The Hohenberg-Kohn theorems show that is possible to use the ground state density to calculate properties of the system. The Kohn-Sham equations provide a route of finding the ground state density. In the Kohn-Sham (KS) one-electron model,[46] a system of independent *non-interacting* electrons in a common one-body potential, v_{KS}, is shown to mimic the true many-electron system. Therefore, one can write the ground state wavefunction explicitly in terms of simple one-electron orbitals. The only complication is that the full wavefunction, ψ_S, must still satisfy exchange anti-symmetry. This is achieved by placing one-electron wavefunction ψ_i in a *Slater determinant*,[47] as follows:

$$\psi_S = \frac{1}{\sqrt{N!}} det\{\psi_i(\boldsymbol{x}_1)\psi_j(\boldsymbol{x}_2)\cdots\psi_k(\boldsymbol{x}_N)\} \tag{2.8}$$

In the KS formalism, they divided the total energy functional $E[\rho]$ in four parts:

$$E[\rho] = T_s[\rho] + \int \rho(\boldsymbol{r})v_{ext}(\boldsymbol{r})d\boldsymbol{r} + J[\rho] + E_{XC}[\rho] \tag{2.9}$$

where $T_s[\rho]$ is the kinetic energy of *non-interacting* electrons. The interaction of the electrons with nuclei is represented by the second term of Eq. (2.9), where v_{ext} is the external potential (see Eq. 2.6). $J[\rho]$ is the classical Coulomb energy and the $E_{XC}[\rho]$ is the exchange-correlation energy which includes the non-classical electron-electron interaction energy and correction towards the kinetic energy corresponding to the fully interacting system $T[\rho]$.

Representing the electron density by a set of occupied one-electron orbitals $\{\psi_i\}$ gives:

$$\rho(\boldsymbol{r}) = \sum_{i=1}^{occ.} \psi_i^*(\boldsymbol{r})\psi_i(\boldsymbol{r}) \tag{2.10}$$

$$T_s[\rho] = -\frac{1}{2}\sum_{i}^{N} \langle\psi_i^*|\nabla_i^2|\psi_i\rangle \tag{2.11}$$

If the orbitals are required to be orthonormal, then a functional of the orbitals can be defined as:

$$\Omega[\psi_i] = E[\rho] - \sum_i \sum_j \varepsilon_{ij} \int \psi_i^*(\boldsymbol{r})\psi_j(\boldsymbol{r})d\boldsymbol{r} \tag{2.12}$$

where ε_{ij} are Lagrange multipliers to ensure the orbitals are orthonormal. Minimization of $\Omega[\psi_i]$ with respect to $\psi_i^*(\mathbf{r})$ gives the Kohn-Sham equations:

$$\left[-\frac{1}{2}\nabla_i^2 + v_{eff}(\boldsymbol{r})\right]\psi_i(\boldsymbol{r}) = \varepsilon_i\psi_i(\boldsymbol{r}) \tag{2.13}$$

where $v_{eff}(\mathbf{r})$ denotes the Kohn-Sham potential defined as:

$$v_{eff}(r) = v_{ext}(\boldsymbol{r}) + v_H + v_{xc}(\boldsymbol{r}) \tag{2.14}$$

The second term in Eq. (2.14) is the Hartree potential:

$$v_H = \int \frac{\rho(\boldsymbol{r}')}{|\boldsymbol{r} - \boldsymbol{r}'|} d\boldsymbol{r}' \tag{2.15}$$

And $v_{xc}(\mathbf{r})$ is the functional derivative of the exchange-correlation energy E_{xc}:

$$v_{xc}(\boldsymbol{r}) = \frac{\delta E_{xc}}{\delta \rho(\boldsymbol{r})} \tag{2.16}$$

The exchange-correlation energy is clearly the crucial quantity of DFT. It is, after a Kohn-Sham calculation, the only quantity for which a reliable estimate is needed to obtain a good total energy. Kohn and Sham paved the way for a renaissance for DFT. The problem of the kinetic energy was largely solved. The new challenge was to find a solution for E_{xc}. More than fifty years on, the problem remains unsolved.

2.1.3 Relativistic DFT

Heavy element compounds are not only systems with many electrons (and therefore expensive), they also require proper treatment of relativistic effects. The question whether the Hohenberg-Kohn and Kohn-Sham theorems could be used in a relativistic theory was answered by Rajagopal and Callaway, who provided the necessary generalization of these theorems.[48] Relativistic DFT is actually Current Density Functional Theory (CDFT) since the close relation between electric and magnetic fields makes it necessary to consider also the dependence on the current, instead of just the density. We refer to some of the many excellent references focusing on the relativistic quantum chemistry for details.[49,50] Below we will briefly discuss the elementary parts of the two- and four-component relativistic corrections used in this thesis.

2.1.3.1 The Dirac equation

A conceptually direct way of performing a relativistic molecular computation is to use directly the time-independent Dirac equation[51]:

$$\widehat{H}^{D}\psi^{D} = E\psi^{D} \tag{2.17}$$

where $\widehat{H}^{D}$ is the Dirac Hamiltonian:

$$\widehat{H}^{D} = c\boldsymbol{\alpha}\cdot\boldsymbol{p} + mc^{2}\boldsymbol{\beta} + V\boldsymbol{I}_{4} \tag{2.18}$$

In equation 2.17, the eigenfunction, ψ^{D}, is a four-component vector which contains two "large" components, which pass to the corresponding non-relativistic wave functions for **α** and **β** spin in the limit $c \rightarrow \infty$, and two "small" components which vanish in the nonrelativistic limit. The Hamiltonian given in (2.18) is a matrix operator in which **p** is a 3 x 3 unit vector whose elements correspond to the components of the momentum, and V is the nucleus-electron interaction term, which for point nuclei takes the form:

$$V = -\sum_{Ai}\frac{Z_{A}}{r_{Ai}} \tag{2.19}$$

where Z_{A} is the charge associated with the Ath nucleus and r_{Ai} is the distance between the Ath nucleus and the ith electron. In the Dirac Hamiltonian (2.18), the components of **α** may be written in terms of the Pauli spin matrices, σ, and $\mathbf{I}_{4}$ is the 4 x 4 unit matrix.

The Dirac equation is not often used in its original four-component form because such molecular computations are unfortunately quite expensive as compared to nonrelativistic ones, and the explicit inclusion of electron correlation is a formidable task. Implementation of Dirac theory requires a significant rewrite of existing code and this feature has prevented the method from entering ordinarily in quantum chemistry.

Many attempts have been made to transform the four-component equation (2.17) into two-component form, in order to keep interpretations simpler and to reduce the computational effort. In the next section, we will give an account of one of these methods.

2.1.3.2 The Breit-Pauli approximation

Shifting the diagonal of the Dirac Hamiltonian by $-2mc^{2}$ to align the relativistic and nonrelativistic energy scales and writing the Dirac equation in two component form (with both lines representing two equations) gives the eigenvalue equation:

$$\begin{pmatrix} V & c\sigma\cdot\pi \\ c\sigma\cdot\pi & -2mc^2+V \end{pmatrix}\begin{pmatrix}\psi^L(\boldsymbol{r}) \\ \psi^S(\boldsymbol{r})\end{pmatrix} = E\begin{pmatrix}\psi^L(\boldsymbol{r}) \\ \psi^S(\boldsymbol{r})\end{pmatrix} \tag{2.20}$$

We simplify by assuming that we have no magnetic fields so that $\mathbf{A} = 0$ and $\pi = \mathbf{p}$, and derive a relation between ψ^L and ψ^S by writing the lower equation as:

$$\psi^S(\boldsymbol{r}) = K(E,\boldsymbol{r})\frac{\sigma\cdot\boldsymbol{p}}{2mc}\psi^L(\boldsymbol{r}) \tag{2.21}$$

with K a local multiplicative operator that depends on the energy of the electron:

$$K(E,\boldsymbol{r}) = \left(1+\frac{E-V}{2mc^2}\right)^{-1} \tag{2.22}$$

By inserting Eq. (2.21) in the upper line of Eq. 2.20 we obtained a two-component equation for the large component wave function:

$$\left(\frac{1}{2m}(\sigma\cdot\boldsymbol{p})K(E,\boldsymbol{r})(\sigma\cdot\boldsymbol{p})+V\right)\psi^L(\boldsymbol{r}) = E\psi^L(\boldsymbol{r}) \tag{2.23}$$

This equation is known as the Unnormalized Elimination of the Small Component (UESC) equation. The UESC equation is exact, but not very practical since it is not an eigenvalue equation. It mainly serves as a starting point for approximations to the Dirac equation. Close to the nuclei, $(E-V)/2mc^2$ cannot be regarded as a small expansion parameter. The other assumption is that V is small compared to $2mc^2$. In molecules electrons will, however, also come close to the nuclei where V can be (much) larger than $2mc^2$. In these small regions around the nuclei the chosen expansion of K is not valid and the resulting operators are invalid.

2.1.3.3 The Zeroth Order Regular Approximation (ZORA)

With the cause of the problem identified it is clear what needs to be done: one should find a series expansion that is valid for the whole region of space. The regular expansion became popular after its introduction in DFT by van Lenthe, Snijders and Baerends in 1993.[24] The idea is to rewrite the inverse operator in K as:

$$K = \left(1 + \frac{E - V}{2mc^2}\right)^{-1} = \left(1 - \frac{V}{2mc^2}\right)^{-1}\left(1 + \frac{E}{2mc^2 - V}\right)^{-1} \tag{2.24}$$

where $\frac{E}{2mc^2 - V}$ is used as the expansion parameter. This parameter is small everywhere because E is constant and always smaller than $2mc^2 - V$ (remember that V is negative so that the denominator is even larger than $2mc^2$). In practice, it is common to include only the first term of the expansion which gives the Zeroth Order Regular Approximation (ZORA) Hamiltonian:

$$\left(\left(\frac{1}{2m}(\sigma \cdot \boldsymbol{p})\right)\left(1 - \frac{V}{2mc^2}\right)^{-1}(\sigma \cdot \boldsymbol{p}) + V\right)\psi^{ZORA}(\boldsymbol{r}) = E\psi^{ZORA}(\boldsymbol{r}) \tag{2.25}$$

And the scalar relativistic version of the ZORA equation can be written as:

$$\left(\frac{1}{2m}\boldsymbol{p} \cdot \left(1 - \frac{V}{2c^2}\right)^{-1}\boldsymbol{p} + V\right)\psi^{ScZORA}(\boldsymbol{r}) = E^{ScZORA}\psi^{ScZORA}(\boldsymbol{r}) \tag{2.26}$$

2.1.3.4 Four-component methods

An alternative approach is to retain the simplicity of the relativistic formalism and solve the Dirac equation by expanding the large and the small components in a basis set of the form:

$$\{\chi^{4c}\} = \left\{\begin{pmatrix}\chi^L \\ 0\end{pmatrix}\right\} \cup \left\{\begin{pmatrix}0 \\ \chi^S\end{pmatrix}\right\} \tag{2.27}$$

$$\psi^{4c} = \sum_{\kappa}^{n^L} C_\kappa^L \chi_\kappa^L + \sum_{\lambda}^{n^S} C_\lambda^S \chi_\lambda^S \tag{2.28}$$

in which χ^{L} and χ^{S} are two-component functions. With this choice of basis the Dirac equation becomes a matrix equation:

$$\begin{pmatrix}\boldsymbol{V}^{LL} & c\boldsymbol{\Pi}^{LS} \\ c\boldsymbol{\Pi}^{SL} & \boldsymbol{V}^{SS} - 2mc^2\boldsymbol{S}^{SS}\end{pmatrix}\begin{pmatrix}\boldsymbol{C}^L \\ \boldsymbol{C}^S\end{pmatrix} = \begin{pmatrix}\boldsymbol{S}^{LL}\boldsymbol{C}^L \\ \boldsymbol{S}^{SS}\boldsymbol{C}^S\end{pmatrix}E \tag{2.29}$$

that can be diagonalized to give the energies and expansion coefficients $\boldsymbol{C}^{\mathrm{L}}$ and $\boldsymbol{C}^{\mathrm{S}}$. Matrix elements of the Dirac and the Coulomb-Breit operator are easily computed by standard methods. The main disadvantage of the 4c-component scheme is that the size of matrices is at least twice as large as in nonrelativistic theory.

2.2 Calculation of NMR parameters

The molecular properties responsible for the generation of NMR spectra were first identified and analyzed in terms of perturbation theory by Ramsey.[52] Since then, even though the improvements in the methodology techniques and computer technology have been very impressive over the last three decades, the theoretical prediction of NMR spectral properties significantly lagged experimental work. Nevertheless, great progress has been made over the last two decades, particularly with respect to DFT, and the calculation of chemical shifts is becoming much more routine than previously.

In a genuine NMR experiment, the electromagnetic frequency is fixed (radio wave lengths) and the sample is scanned by a variable magnetic field. At some particular field values the energy difference matches the electromagnetic frequency and the transition (Nuclear Magnetic Resonance) is observed.

The magnetic field that a particular nucleus feels differs from the external magnetic field applied, because the electronic structure in which the nucleus is immersed in, makes its own contribution. Also, the nuclear spins interact by creating their own magnetic fields. The effects which we are now dealing with are so small, that they are not important for most applications. This time, however, the situation changes: we are going to study very subtle interactions using the NMR technique which aims precisely at the energy levels that result from spin-spin and spin-magnetic field interactions. Even if these effects are very small, they can be observed.

2.2.1 Theoretical background

In this section, we will discuss only some aspects of DFT methods that are related to the calculation of NMR properties (see reviews[53,54]). In the presence of a magnetic field, the usual Hohenberg-Kohn theorems as outline in section 2.1.1 do not hold anymore and the corresponding exchange-correlation energy is a functional of both the electron density

$\rho(\mathbf{r})$, as in ordinary DFT, and the current density $\mathbf{j}(\mathbf{r})$. Instead, the expressions determining the energy and the magnetic properties are obtained by introducing an exchange-correlation density functional that depends on the density ρ and on the paramagnetic current density:

$$\boldsymbol{j}_p(\boldsymbol{r}) = -i\sum_k \left(\phi_k^*(\boldsymbol{r})\nabla\phi_k(\boldsymbol{r}) - \phi_k(\boldsymbol{r})\nabla\phi_k^*(\boldsymbol{r})\right) \tag{2.30}$$

Together with some assumptions for the dependence of the energy functional on $\mathbf{j}_p(\mathbf{r})$, these densities form the basis for the current-density functional theory (CDFT).[55,56] Such approximations to the exchange-correlation energy functional are still in the early development phase and have not reached the maturity to be of any practical relevance. Therefore, this additional current dependency can be neglected:

$$E_{XC}[\rho(\boldsymbol{r}), j(\boldsymbol{r})] \approx E_{XC}[\rho(\boldsymbol{r})] \tag{2.31}$$

Fortunately, it seems that this is not a crude approximation and one does not need to worry too much about using functionals which are formally inadequate because they neglect the required dependence on $j(\mathbf{r})$.[57]

On the other hand, the magnetic external field and the intrinsic nuclear magnetic moments can be treated as perturbations. For this reason, the nuclear magnetic shielding tensor, $\boldsymbol{\sigma}$, is calculated as an energy derivative. This second-order molecular property can be expressed as the second derivative of the energy of the molecule, E, with respect to an external magnetic field, $\boldsymbol{B}$, and the magnetic moment of a nucleus, $\boldsymbol{\mu}$, as in Eq. (2.32).

$$\boldsymbol{\sigma} = \left(\frac{\partial^2 E}{\partial \boldsymbol{B} \partial \boldsymbol{\mu}}\right)_{\boldsymbol{B}=\boldsymbol{\mu}=0} \tag{2.32}$$

The magnetic tensor $\boldsymbol{\sigma}$ is a non-symmetric 3 x 3 tensor, whose trace, $\boldsymbol{\sigma}_{\text{iso}} = 1/3(\boldsymbol{\sigma}_{\text{xx}} + \boldsymbol{\sigma}_{\text{yy}} + \boldsymbol{\sigma}_{\text{zz}})$, is the isotropic magnetic shielding of the nucleus. NMR-DFT calculations allow for the decomposition of the total magnetic shielding, and thus the chemical shift, into paramagnetic and diamagnetic terms, $\boldsymbol{\sigma}_{\text{iso}} = \boldsymbol{\sigma}_{\text{dia}} + \boldsymbol{\sigma}_{\text{para}}$. The diamagnetic term of the shielding constant depends only on the unperturbed electron density in the ground state. In contrast, the paramagnetic term depends on both occupied-occupied and occupied-virtual couplings between molecular orbitals, induced by the external magnetic field. The paramagnetic term can be correlated to the ability of the external magnetic field to create a circulation of electrons through the molecules. The induced current density moves in a plane perpendicular to the external magnetic field, generating an induced magnetic field that adds to the external one, resulting in deshielding, or downfield shift.

The energy in Equation (2.32) can be computed using approximated methods, among those HF and DFT, or explicitly correlated wavefunction-based methods. In particular for DFT, the usual way to tackle Eq. (2.32) is by employing stationary perturbation theory. The integrals in question are complex because the magnetic field perturbs the kinetic energy term (it is the motion of the electrons that generates electronic magnetic moments). The nature of the perturbed kinetic energy operator is such that an origin must be specified defining a coordinate system for the calculation. This origin is called the 'gauge origin'. The magnetic field is independent of the choice of the gauge origin. So too are the computed magnetic properties if the wave function used is exact. Regrettably, we are not often afforded the opportunity to work with exact wave functions. Thus, to reduce artifacts associated with the gauge origin, an approach must be specified. In this work, we have used the method that uses gauge-including atomic orbitals (GIAOs) as a basis set (London 1937). By a clever incorporation of the gauge origin into the basis functions themselves, all matrix elements involving the basis functions can be arranged to be independent of it. More details of the fundamental theory as well as on many technical aspects regarding the calculation of NMR parameters in the context of various quantum chemical techniques can be found in the literature.[58]

2.3 Simulation techniques

Molecular simulation refers to methods aimed at generating a representative sampling of a system at a finite temperature.[59-62] Most reactions are both qualitatively and quantitatively different under gas and solution phase conditions, especially those involving ions or polar species. Simulations are therefore intimately related with describing solute-solvent interactions, but such effects can also be modelled with less rigorous methods. Likewise, molecular properties as NMR chemical shifts are also sensitive to the chemical environment. Thus, in this section we summarize two strategies employed in this thesis to include liquid state conditions.

2.3.1 Continuum Solvent Models

The methods based on the continuum model allow to simulate both bulk and short-range (specific) solute-solvent interactions. An extensive review of continuum models up to the most recent developments and applications can be found in several references.[63-65] In the basic idea of all continuum model, the molecule of interest (solute) is assumed to reside in a "cavity" and described fully at a quantum level. The solvent, on the other hand, rather than represent its charge distribution explicitly, is incorporated as a continuum medium (a continuous electric field around the cavity that represents a statistical average over all solvent degrees of freedom at thermal equilibrium (see Figure 2.1). This field is usually called the 'reaction field' in the regions of space occupied by the solute, since it derives from reaction of the solvent to the presence of the solute.

The electric field at a given point in space is the gradient of the electrostatic potential ϕ at that point, and the work required to create the charge distribution may be determined from the interaction of the solute charge density ρ with the electrostatic potential according to:

$$G = -\frac{1}{2}\int \rho(\boldsymbol{r})\phi(\boldsymbol{r})d\boldsymbol{r} \tag{2.33}$$

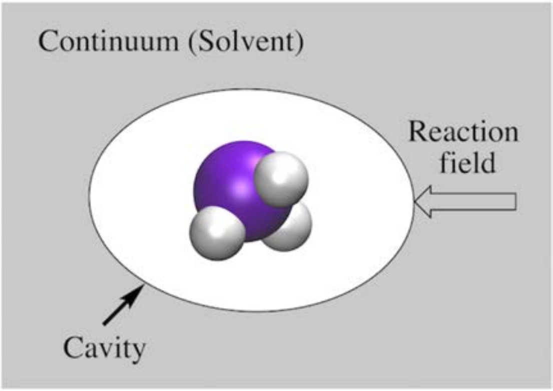

Figure 2.1. Model representation of a solute molecule in a cavity and the solvent as a continuum, which reacts on the molecular electric field by a reaction field.

The charge density ρ of the solute may be expressed either as some continuous function of $\mathbf{r}$ or as discrete point charges, depending on the theoretical model used to represent the solute. The polarization energy, G_P, discussed above, is simply the difference in the work of charging the system in the gas phase and in solution. Thus, in order to compute the polarization free energy, all that is needed is the electrostatic potential in solution and in the gas phase (the latter may be regarded as a dielectric medium characterized by a dielectric constant of 1). The continuum methods are the most widely used schemes as they are readily implemented and give results relatively quickly and automatically, however, they are not generally very accurate.

2.3.2 Molecular dynamic simulations

Molecular dynamic (MD) simulation is a well-established technique that give us a clear picture of the microscopic structure of liquids providing typical fluid configurations in an atomistic and dynamic detail. Combined with quantum mechanical (QM) calculations, it can help to determine properly NMR parameters in liquid state conditions.[14] In the following, a short description of this technique is given and an extensive review of molecular dynamics up to the most recent developments and applications can be found in several additional reading materials or text books.[66-68]

If we knew the potential energy V as a function of the position ($\boldsymbol{R}$) of all the atoms (whatever force field has been used for the approximations), then all the forces the atoms undergo could be easily computed. If $\boldsymbol{R} = (X_1, X_2, \ldots, X_{3N})^T$ denotes the coordinates of all the N atoms (X_1, X_2, X_3 are the x, y, z coordinates of atom 1, X_4, X_5, X_6 are the x, y, z of atom 2, etc.), then $-\frac{\partial V}{\partial X_1}$ is the x component of the force atom 1 undergoes, $-\frac{\partial V}{\partial X_2}$ is the y component of the same force, etc. When a force field is used, all this can be easily computed even analytically. In molecular dynamics, we are interested in time t, the velocity of the atoms (in this way temperature will come into play), and the acceleration of the atoms.

The Newton equation tell us that, knowing the force acting on a body (*e. g.*, an atom), we may compute the acceleration the body undergoes. We have to know the mass, but there is no problem with that. Hence the i-th component of the acceleration vector is equal to:

$$\boldsymbol{a}_i = -\frac{\partial V}{\partial X_i} \cdot \frac{1}{M_i} \tag{2.34}$$

for $i = 1, 2, \dots, 3N$ ($M_i = M_1$ for $i = 1, 2, 3, M_i = M_2$ for $i = 4, 5, 6, etc.$).

Now, let us assume that at $t = 0$ all the atoms have the initial coordinates $\boldsymbol{R}_0$ and the initial velocities $\boldsymbol{v}_0$. Now we assume that the forces calculated act *unchanged* during a short period Δt (often 1 femtosecond or 10^{-15} s). We know what should happen to a body (atom) if under influence of a constant force during time Δt. Each atom undergoes a uniformly variable motion and the new position may be found in the vector:

$$\boldsymbol{R} = \boldsymbol{R}_0 + \boldsymbol{v}_0 \Delta t + \boldsymbol{a} \frac{\Delta t^2}{2} \tag{2.35}$$

and its new velocity in the vector:

$$\boldsymbol{v} = \boldsymbol{v}_0 + \boldsymbol{a} \Delta t \tag{2.36}$$

where the acceleration $\boldsymbol{a}$ is a vector composed of the acceleration vectors of all the N atoms:

$$\begin{aligned} \boldsymbol{a} &= (\boldsymbol{a}_1, \boldsymbol{a}_2, \dots, \boldsymbol{a}_N)^T \\ \boldsymbol{a}_1 &= \left(-\frac{\partial V}{\partial X_1}, -\frac{\partial V}{\partial X_2}, -\frac{\partial V}{\partial X_3}\right) \cdot \frac{1}{M_1} \\ \boldsymbol{a}_2 &= \left(-\frac{\partial V}{\partial X_4}, -\frac{\partial V}{\partial X_5}, -\frac{\partial V}{\partial X_6}\right) \cdot \frac{1}{M_2}, etc \end{aligned} \tag{2.37}$$

All on the right hand of Equations (2.35) and (2.36) is known. Therefore, the new positions and the new velocities are easy to calculate. Now, we may use the new positions and velocities as a start ones and repeat the whole procedure over and over. This makes it possible to go along the time axis in a step-like way in practice reaching even micro times (10^{-9} sec), which means billions of such steps. The procedure described above simply represents the numerical integration of $3N$ differential equations. If $N = 2000$ then the task is impressive. It is so straightforward, because we are dealing with numerical (not analytical) solutions.

The computer simulation makes the system evolve from the initial state to the final one. The position $\boldsymbol{R}$ in $3N$-dimensional space becomes a function of time and therefore $\boldsymbol{R}(t)$ represents the trajectory of the system in the configurational space. A similar statement affects to $\boldsymbol{v}(t)$. Knowing the trajectory means that we know the smallest details of the motion of all the atoms. Within the approximation used, we may ask about some mean values, like the mean value of the total energy, potential energy, kinetic energy, the distance between atoms, etc. All these quantities may be computed at any step of the procedure, then added up and divided by the number of steps giving the mean values we required. In this way we may obtained the theoretical prediction of the mean value of the computed chemical shielding and compare it to, say, the NMR result.

Chapter 3

Objectives

The overall aim of this thesis is to computationally determine the NMR shift constants in a number of chemical systems of interest, using both *static* and *dynamic* approaches, which will complement experimental data. Given the sensitivity of NMR, this will confirm the presence of transient species and/or explain ambiguous signals in the NMR spectra. As NMR measurements are extremely sensitive to both indirect and direct effects, our objective is to gain a better understanding and learn about how methodological issues, such as the level of theory, basis set, relativistic effects, chemical environment, among others, may affect the quality of the calculated data.

Likewise, the objectives can be divided according to the studies presented in this thesis:

Chapter 4 *"The influence of substituent and the environment on the NMR shielding constants of supramolecular complexes based on A-T and A-U base pairs"*

- Examine the effect of the substituents on the hydrogen-bond lengths, strength and bonding mechanism, and the NMR shielding constants of the *C*2-adenine and *C*2-thymine/uracil atoms in the base pairs.

Chapter 5 *"Four-component relativistic ^{31}P-NMR calculations in trans-platinum(II) complexes: Importance of the solvent and dynamics in spectral simulations"*

- Determine the ^{31}P-NMR chemical shifts of the *trans*-[PtCl$_2$(dma)(PPh$_3$)]

complex and species derived from its hydrolysis, in an attempt to understand its mechanism of action as anticancer platinum drug.

- Demonstrate, comparing with experimental spectra, the importance of relativistic effects, dynamics, and explicit solvation for the accurate modelling of the ^{31}P chemical shifts.

Chapter 6 *"Computational NMR Spectroscopy for Host-Guest Hemicarcerands"*

- Study the structure and ^{1}H-NMR chemical shifts of hemicarcerand **1** and its corresponding hemicarceplexes with *o*-benzyne and a variety of 27 guests from which experimental data are available for comparison.
- Describe the rotational mobility and the conformational preference for the guest molecules.
- Predict the ^{1}H and ^{13}C-NMR chemical shift constants of *o*-benzyne within hemicarcerand **2**.

Chapter 7 *"Exploring the potential energy surface of E_2P_4 clusters (E= Group 13 elements): The quest for inverse carbon-free sandwiches"*

- Explore if it is possible to stabilize a carbon-free inverse sandwich E_2P_4 structures by selecting the appropriate Group 13 atoms.
- Analyze the bonding to provide an explanation about the structural preferences.
- Predict the ^{31}P-NMR shielding constants in order to support future experimental analysis.

Chapter 4

The Influence of Substituents and the Environment on the NMR Shielding Constants of Supramolecular Complexes based on A-T and A-U Base Pairs[a]

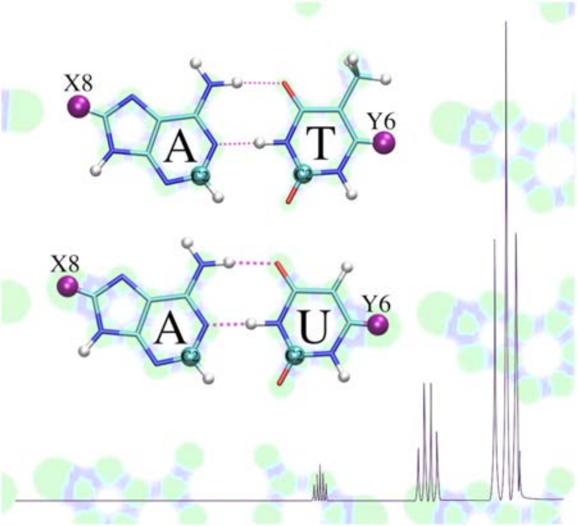

---

[a] This chapter is based on the publication: A. C. Castro, M. Swart, C. Fonseca-Guerra, *Phys. Chem. Chem. Phys.*, **2017**, 19, 13496-13502. [*cover*: PCCP, 2017, 19, 14188.].

SUMMARY

In this chapter, we have theoretically analyzed supramolecular complexes based on the Watson-Crick A-T and A-U base pairs using dispersion corrected density functional theory (DFT). Hydrogen atoms H8 and/or H6 in the natural adenine and thymine/uracil bases were replaced, respectively, by substituents X8, Y6 = NH^-, NH_2, NH_3^+ *(N series),* O^-, *OH,* OH_2^+ *(O series), F, Cl or Br (halogen series). We examined the effect of the substituents on the hydrogen bond lengths, strength and bonding mechanism, and the NMR shielding constants of the C2-adenine and C2-thymine/uracil atoms in the base pairs. The general belief in the literature that there is a direct connection between changes in the hydrogen-bond strength and the C2-adenine shielding constant is conclusively rejected by our computations.*

4.1 State of the art

Hydrogen bonds are important in many fields of biological chemistry. They play, for instance, a key role in the working of the genetic code.[69-73] In particular, the stability of the Watson-Crick DNA (A-T) and RNA (A-U) base pairs has been studied and it has been found that the hydrogen bonds in A-U are stronger than those of A-T.[74] In 2004, Acharya *et al.* found that the pKa values of the donors and acceptors of A-U pairs are more similar than those of A-T pairs, which was interpreted as evidence for stronger RNA hydrogen bonds than those of DNA.[75] Furthermore, Vakonakis and LiWang reported the same assumption based on measurements of *C2* chemical shifts and deuterium isotope effects in adenine.[76,77]

Calculations of NMR parameters have significantly contributed to understanding the molecular interactions of DNA and RNA bases.[78,79] So far, ^{15}N-NMR shielding tensors, as a function of the hydrogen-bond length, have been systematically investigated for the G-C base pair, concluding that the shielding values strongly depend on the distance between the bases.[80] Furthermore, the shift tensors of carbon atoms in purine-based compounds were found to be sensitive to local structure changes like substitution on the purine ring, tautomerism, and intermolecular interactions.[81] In our previous work,[8] we analyzed with density functional theory (DFT) the geometries, counterpoise-corrected bond energies, and the NMR shielding parameters of the Watson-Crick A-T and A-U base pairs concluding that the introduction of a methyl substituent at the pyrimidine ring affects both NMR shielding constants (*e.g.*, for adenine *C2* atom) and hydrogen-bond strengths (*e.g.*, A-T *versus* A-U). However, these are two independent and uncorrelated effects and the results of NMR experiments do not directly reflect the strength of the hydrogen bonds.[8] This was confirmed by a subsequent study using DFT and hybrid DFT/MM calculations of deuterium isotope effects (DIEs) on nucleosides and nucleotides.[82] More recently, Pérez *et al.* suggested by employing a variety of quantum-mechanical techniques that the differences between the stability of RNA and DNA are due to a variety of effects (*e.g.*, intra- and intermolecular stacking and other subtle contributions related to their global conformation) rather than resulting from a significant difference in the hydrogen bonding of DNA and RNA base pairs.[83]

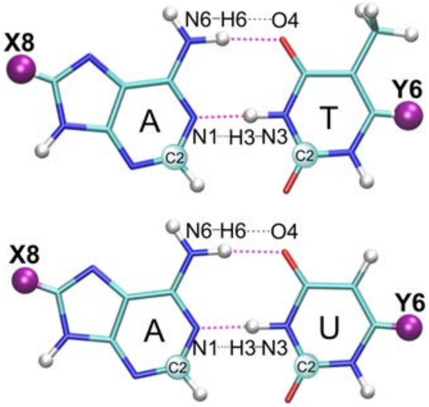

Figure 4.1. Model structures of substituted A^{X8}–T^{Y6} and A^{X8}–U^{Y6} base pairs, where X8, Y6= NH^-, NH_2, NH_3^+ (N series), O^-, OH, OH_2^+ (O series), F, Cl or Br (halogen series).

Based on previous findings, we know that supramolecular switches, that is, dimers with tunable hydrogen-bond strength, can be built using the DNA Watson-Crick base pairs. In particular, the hydrogen-bond strengths in A-T and G-C base pairs were investigated when anionic, neutral, cationic or halogen substituents are introduced at remote positions, that is, at atoms of the DNA base that are not involved in the N–H···O or N···H–N hydrogen bonds. These switches can be moved between three different states of hydrogen-bond strength and geometrical shape simply by changing the substituents.[84-86] The question that arises and is tackled in the present study is how this strengthening and weakening will influence the individual NMR chemical shielding constants. Thus, in this chapter we examined the dependence of the NMR *C2-adenine* and *C2-thymine/uracil* shielding constants as a function of the hydrogen-bond strength of the natural and substituted A^{X8}-T^{Y6} and A^{X8}-U^{Y6} base pairs (see Figure 4.1), and examined if there is evidence to support the idea of a correlation between these two effects.

Our results prove that a larger *C2-adenine* shielding does not necessarily correspond to a stronger interaction. In fact, the NMR *C2-adenine* and *C2-thymine/uracil* shielding constants merely probe the presence/absence of substituents at the adenine X8 and thymine/uracil Y6 positions.

4.2 Computational Methods

All calculations were performed with the Amsterdam Density Functional (ADF)[87,88] and QUILD[89] programs using dispersion corrected relativistic density functional theory at the ZORA-BLYP-D3(BJ)/TZ2P level for geometry optimizations, frequencies and energies.[90-93] The BLYP-D3(BJ) functional was recently shown to yield excellent results for hydrogen bonding structures and energies for A-T and G-C Watson-Crick pairs and stacked configurations.[92-94] The NMR shielding constants were calculated using the Gauge Including Atomic Orbital (GIAO) method to treat the gauge dependence problem.[95] The TZ2P[96] and the ET-pVQZ[97] all electron basis sets were used in conjunction with the KT2,[6] S12g[98] and SAOP[99] functionals (see Appendix 1, where B3LYP[100] data can also be found), which were shown to improve the description of NMR shielding constants significantly. This is in particular true for KT2 when compared[101] to high-level CCSD(T) calculations and experiments when large basis sets were used by Helgaker, Tozer and Gauss. The effect of the density functional, solvation (through the COSMO[102-104] model) or Spin-Orbit relativistic corrections is however minor for the substituent effects: obviously the absolute values of the NMR shieldings vary with the use of different methodologies. But the effect of replacing *e.g.* Ade-H8 by an anionic substituent leads in all cases to a drastic increase of the shielding; a cationic substituent there instead leads to a significant lowering; these substituent effects are observed in all cases, irrespective of the particular method in place (see Appendix 1).

4.2.1 Energy decomposition analysis setup

The hydrogen bonding in the model systems was analyzed in the conceptual framework provided by the Kohn-Sham molecular orbital model, using a quantitative bond energy decomposition analysis (EDA)[105-107] implemented in the ADF2014 package at the BLYP-D3(BJ)/TZ2P and S12g/TZ2P levels (both functionals lead to the same findings). The hydrogen bond energy, ΔE_{Bond}, contains two components [Eq. (4.1)].

$$\Delta E_{Bond} = \Delta E_{prep} + \Delta E_{int} \tag{4.1}$$

In this formula, the preparation energy, ΔE_{prep}, is the amount of energy required to deform the separate bases from their equilibrium structure to the geometry that they acquire in the pair. The interaction energy, ΔE_{int}, corresponds to the actual energy change when the prepared bases are combined to form the base pair.

ΔE_{int} can be divided into four components as shown in Equation (4.2).

$$\Delta E_{int} = \Delta V_{elstat} + \Delta E_{Pauli} + \Delta E_{oi} + \Delta E_{disp} \tag{4.2}$$

The term $\Delta V_{\mathrm{elstat}}$ corresponds to the classical electrostatic interaction energy between the unperturbed charge distributions of the prepared (i.e. deformed) bases and is usually attractive. The second term in Equation (4.2), $\Delta E_{\mathrm{Pauli}}$, refers to the repulsive interactions between the fragments, which are caused by the fact that two electrons with the same spin cannot occupy the same region in space. $\Delta E_{\mathrm{Pauli}}$ was computed by enforcing the Kohn-Sham determinant of the superimposed fragments to obey the Pauli principle by antisymmetrization and renormalization. The stabilizing orbital interaction term, ΔE_{oi}, was estimated in the final step of the energy partitioning analysis when the Kohn-Sham orbitals relax to their optimal form. This term can be further partitioned into contributions by the orbitals belonging to different irreducible representations of the point group of the interacting system [Eq. (4.3)]. In systems with a clear σ and π separation, this symmetry partitioning proves to be very informative.

$$\Delta E_{oi} = \Delta E_{oi,\sigma} + \Delta E_{oi,\pi} \tag{4.3}$$

The last term ΔE_{disp} in equation (4.2) refers to the dispersion correction term.

4.3 Results and Discussion

4.3.1 Substituent effects on the model structures

The nomenclature selected in the present study is exemplified in Figure 4.1. Letters A, T and U have been used for the natural DNA and RNA bases, indicating with a superscript the substitutions of the X8 and Y6 atoms in the bases. Thus, A^{H8}-T^{H6} represents the natural Watson-Crick base pair, A-T, whereas A^{F8}-T^{F6} refers to an adenine-thymine complex in which adenine H8 and thymine H6 have been replaced by fluorine atoms. In accordance with our previous work,[84-86] all the base pairs have been optimized and analyzed in C_s symmetry, whereas the isolated bases were optimized in C_1 symmetry without any geometry restriction.

The hydrogen-bond distances and bond energies of the natural and substituted Watson-Crick base pairs A^{X8}-T^{Y6} and A^{X8}-U^{Y6} are summarized in Table 4.1. Our BLYP-D3(BJ)/TZ2P results yield N6–H6···O4 and N1···H3–N3 hydrogen-bond distances in A-T of 2.88 and 2.80 Å, respectively, which agree well with those obtained at the BP86/TZ2P level (2.85 and 2.81 Å)[8,86] and at the RI-MP2/cc-pVTZ level (2.86 and 2.83 Å).[108] Likewise, the hydrogen-bond results for the A-U base pair are 2.89 and 2.79 Å, which are similar to our previous work[8,86] at the BP86/TZ2P level (2.86 and 2.81 Å). Hence, the introduction of methyl groups at pyrimidine-C5 (*i.e.* replacing uracil by thymine) affects

Table 4.1. Hydrogen-bond lengths (Å) and bond energies ΔE_{Bond} (kcal·mol^{-1}) for A^{X8}-T^{Y6} and A^{X8}-U^{Y6} base pairs[a]

		A^{X8}-T^{Y6}			A^{X8}-U^{Y6}		
X8	Y6	N6-H6···O4	N1···H3-N3	ΔE_{Bond}	N6-H6···O4	N1···H3-N3	ΔE_{Bond}
H	H	2.884	2.797	-16.50	2.891	2.792	-16.77
NH_2	NH_2	2.871	2.799	-15.86	2.882	2.794	-16.00
OH	OH	2.882	2.791	-16.65	2.892	2.787	-16.80
NH^-	H	2.841	2.754[b]	-21.40	2.849	2.753[b]	-22.15
NH_2	H	2.897	2.792	-15.23	2.908	2.786	-15.49
NH_3^+	H	2.763	2.864	-19.67	2.775	2.856	-19.66
O^-	H	2.835	2.745[b]	-20.98	2.844	2.744[b]	-21.77
OH	H	2.889	2.796	-16.47	2.899	2.791	-16.64
OH_2^+	H	2.760	2.867	-20.03	2.769	2.859	-19.98
H	NH^-	2.670	2.957	-17.92	2.673	2.954	-18.27
H	NH_2	2.854	2.805	-16.06	2.863	2.799	-16.36
H	NH_3^+	2.821	2.714[b]	-27.16	2.827	2.723[b]	-28.95
H	O^-	2.682	2.947	-17.70	2.683	2.949	-17.98
H	OH	2.875	2.793	-16.64	2.884	2.787	-16.93
H	OH_2^+	2.853	2.728[b]	-29.44	2.856	2.740[b]	-32.07
F	H	2.880	2.807	-16.50	2.890	2.801	-16.70
Cl	H	2.875	2.807	-16.57	2.886	2.803	-16.75
Br	H	2.879	2.808	-16.59	2.886	2.802	-16.73
H	F	2.893	2.782	-16.94	2.898	2.778	-17.22
H	Cl	2.897	2.784	-16.85	2.899	2.781	-17.16
H	Br	2.899	2.784	-16.88	2.900	2.782	-17.17
F	F	2.890	2.791	-16.84	2.898	2.788	-17.08
Cl	Cl	2.889	2.793	-16.92	2.894	2.792	-17.08
Br	Br	2.897	2.795	-16.91	2.897	2.795	-17.12

[a] Computed at BLYP-D3(BJ)/TZ2P level of theory. [b] Proton transfer occurs in the N1···H3-N3 hydrogen-bond from thymine/uracil to adenine.

hydrogen-bond distances by 0.01 Å or less as we found previously for the methylation at purine-N9, pyrimidine-N1.[109,110] The N6–H6···O4 hydrogen-bond seems to be slightly shorter (stronger) for A-T than for A-U, whereas the reverse is true for the N1···H3–N3 bond. Furthermore, our results corroborate that the RNA (A-U) base pair is more strongly bound (by 0.27 kcal·mol^{-1} at the BLYP-D3(BJ)/TZ2P) than the DNA (A-T) base pair, as was reported before.[8,109]

At the BLYP-D3(BJ)/TZ2P level, the hydrogen-bond energy for A-T amounts to -16.5 kcal·mol^{-1}, which is consistent with the complete-basis-set extrapolated CCSD(T) CBS value of -16.4 kcal·mol^{-1} obtained by Jurečka *et al*.[111,112] The two approaches agree exceptionally well with a difference of only about 0.1 kcal·mol^{-1}, and are fully consistent with the value obtained previously at the BLYP-D/TZ2P level (-16.7 kcal·mol^{-1}).[92] Furthermore, the results for the substituted A^{X8}-T^{Y6} model base pairs are in line with those previously studied theoretically at the BP86/TZ2P level.[8,86] The base pairs involving N6–H6···O4 and N1···H3–N3 hydrogen-bond distances differ by less than 0.04 and 0.01 Å, respectively. For a complete description of the substituted Watson-Crick A^{X8}-T^{Y6} base pairs, see ref. 14 and 19.

Contrary to the substituted A^{X8}-T^{Y6} base pairs, the A-U^{Me6} base pair, to the best of our knowledge, is the only A-U model structure investigated in an earlier theoretical study.[8] Thus, from here onwards we will focus on the analysis of the novel substituted A^{X8}-U^{Y6} base pairs. The effect of the substituents can be understood as deriving from their moderately electron-donating/withdrawing capacity. A neutral substituent (NH_2, OH or halogen) at X8 and/or Y6 positions causes relatively small changes in N6–H6···O4 hydrogen-bond distances and bond energies: the effects are 0.03 Å and 1.3 kcal·mol^{-1} or less, respectively, and the N1···H3–N3 hydrogen-bond distances remain essentially unaffected (0.01 Å or less), as seen in Table 4.1. On the other hand, introducing a charged substituent at adenine X8 or uracil Y6 has more pronounced effects: the hydrogen bonds contract or expand by up to 0.22 Å and the Watson-Crick hydrogen bonds are stabilized by as much as 15.3 kcal·mol^{-1}.

In the following, we examine in more detail the substituent effects and trends therein along X8, Y6 = NH^-, NH_2, and NH_3^+ (N series), but similar arguments emerge also along X8, Y6 = O^-, OH, and OH_2^+ (O series). This corresponds to three different states of protonation: H^+ removed, neutral and H^+ added. First, we inspect the trends along the A^{X8}-U, that is, if only adenine carries a substituent X8 while uracil is un-substituted. Introducing a negatively charged amide substituent NH^- at X8, that is, going from A-U to $A^{(NH^{-})8}$-U, causes the hydrogen-bond strength (ΔE_{Bond}) to increase from -16.8 to -22.2 kcal·mol^{-1} while, simultaneously, the N6–H6···O4 and N1···H3–N3 bonds contract from 2.89 to 2.85 and from 2.79 to 2.75 Å, respectively. Note also in $A^{(NH^{-})8}$-U the transfer of the relatively acidic uracil proton H3 from the N3 atom of uracil to the N1 atom of $A^{(NH^{-})8}$ (see Figure 4.2a). Such a proton transfer also occurs in the similarly substituted $A^{(NH^{-})8}$-T base pair. Next, two successive protonation steps, that is, proceeding along $A^{(NH^{-})8}$-U, $A^{(NH_2)8}$-U, and $A^{(NH_3^{+})8}$-U have the effect of switching the hydrogen-bond strength from -22.2 ("stronger") to -15.5 ("weaker") and back to -19.7 kcal·mol^{-1} ("stronger"). This switching in bond strength is accompanied by a characteristic change in the geometric shape of the natural A-U base pair, which is schematically represented in Figure 4.2.

Next, introducing the substituents on the RNA base, that is, if uracil carries a substituent Y6 while adenine is un-substituted (A-U^{Y6}), induces similar hydrogen-bond energy trends to the substituted effects at adenine X8. In both series, this switching in bond strength from "stronger" to "weaker" and back to "very stronger" is accompanied again by a characteristic change in the geometric shape of the A-U base pair that runs counter to the substituent effects at adenine X8 (see Fig. 4.2d-f and Table 4.1). The first protonation (*i.e.* going from A-U to A-$U^{(NH^{-})6}$) causes the N6–H6···O4 bond to contract and the N1···H3-N3 bond to expand (see Fig. 4.2d). Next, there is no pronounced in-plane bending in A-$U^{(NH_2)6}$ compared to the natural A-U base pair. Finally, one more protonation causes a proton transfer in A-$U^{(NH_3^{+})6}$ from the N3 atom of uracil to adenine N1 (see Fig. 4.2f) and

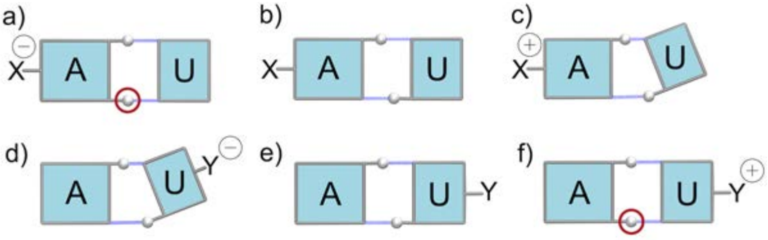

Figure 4.2. Schematic representation of substituent effects on the hydrogen bonds in A-U. The proton transfer from U to A is labeled with a bold circle and occurs in (a) and (f)

the hydrogen bonds are shortened relative to natural A-U. In fact, the latter case with a positively charged group at the Y6 position shows a similar behavior to the A-$T^{(NH_3^+)6}$ base pair.

Additionally, we analyzed in more detail the relatively small changes in hydrogen-bond distances and energies when the A-U base pairs carry halogen substituents (F, Cl or Br). It can be seen that a halogen atom at adenine X8 position has little effect, whereas a halogen atom at uracil Y6 weakens the N6–H6···O4 bond and strengthens the N1···H3–N3 bond. The latter effect apparently dominates (and is the strongest in the case of Y6 = fluorine) as follows from the fact that the overall hydrogen-bond strength (ΔE_{Bond}) increases. Introducing a halogen atom at the adenine X8 position decreases the hydrogen-bond strength by less than 0.1 kcal·mol^{-1}. For example, going from A-U to A^{F8}-U causes a decrease of the ΔE_{Bond} from -16.77 to -16.70 kcal·mol^{-1}. In contrast, a halogen atom at the uracil Y6 position increases the hydrogen-bond strength, *e.g.* going from A-U to A-U^{F6} leads to an energy value of -17.22 kcal·mol^{-1} (see Table 4.1).

4.3.2 Origin of the Substituent Effects

The substituent effects of the A^{X8}-U^{Y6} base pairs described above can be supported by the corresponding energy decomposition analysis (EDA) and Voronoi deformation density (VDD) analysis of the charge distribution. The hydrogen bonding in all our model systems receives an important stabilizing contribution from occupied-virtual interactions, which are almost in the same order of magnitude as the electrostatic interaction (see Table 4.2). This is also true in the substituted A^{X8}-T^{Y6} base pairs for which these analyses have already been reported in an earlier work.[14] As expected, the behavior in A^{X8}-U^{Y6} is similar to that of A^{X8}-T^{Y6}. The percentage contribution of the orbital interactions (ΔE_{oi}) to all the bonding forces (*i.e.*, $\Delta E_{\mathrm{oi}} + \Delta V_{\mathrm{elstat}} + \Delta E_{\mathrm{disp}}$) between the Watson-Crick A^{X8}-U^{Y6} base pairs amounts to 36-40% and the remaining 60-64% is provided by the electrostatic attraction ($\Delta V_{\mathrm{elstat}}$). The partition of the orbital term into contributions from irreducible representations shows that the σ bonding (ΔE_{σ}) is significant stronger than the π bonding (ΔE_{π}), by 88% or more in all cases.

Additionally, in those systems in which proton transfer occurs from uracil to adenine, the covalent component is even larger, up to 68%. Note, however, that this is an artifact of

Table 4.2. EDA analysis (in kcal·mol^{-1}) of the A^{X8}-U^{Y6} base pairs (N and O series)[a]

X8	H	**NH_2**	**NH^-**	**NH_2**	**NH_3^+**	H	H	H
Y6	H	**NH_2**	H	H	H	**NH^-**	**NH_2**	**NH_3^+**
ΔE_{prep}	1.85	2.45	76.44	3.15	1.63	3.22	2.35	69.58
ΔE_{int}	-18.62	-18.45	-98.59	-18.64	-21.29	-21.49	-18.71	-98.53
ΔE_{Pauli}	40.38	40.75	171.73	40.61	38.70	45.72	40.73	151.40
ΔV_{elstat}	-32.36	-32.43	-88.67	-32.35	-33.40	-35.40	-32.75	-78.16
ΔE_{disp}	-5.34	-5.34	-4.99	-5.36	-5.26	-4.93	-5.33	-5.15
ΔE_{oi}	-21.29	-21.43	-176.65	-21.54	-21.34	-26.88	-21.35	-166.62
ΔE_{σ}	-19.71	-19.89	-163.73	-19.96	-19.20	-23.75	-19.78	-151.14
ΔE_{π}	-1.58	-1.54	-12.92	-1.58	-2.14	-3.13	-1.57	-15.48
$\%\Delta V_{elstat}$[b]	54.9	54.8	32.8	54.6	55.6	52.7	55.1	31.2
$\% \Delta E_{disp}$[b]	9.0	9.0	1.8	9.0	8.8	7.3	9.0	2.1
$\% \Delta E_{oi}$[b]	36.1	36.2	65.4	36.4	35.6	40.0	35.9	66.7
ΔE_{Bond}	-16.77	-16.00	-22.15[c]	-15.49	-19.66	-18.27	-16.36	-28.95[c]

X8	H	**OH**	**O^-**	**OH**	**OH_2^+**	H	H	H
Y6	H	**OH**	H	H	H	**O^-**	**OH**	**OH_2^+**
ΔE_{prep}	1.85	2.01	74.95	1.94	1.57	2.96	1.93	73.49
ΔE_{int}	-18.62	-18.81	-96.72	-18.58	-21.55	-20.94	-18.86	-105.56
ΔE_{Pauli}	40.38	40.67	171.06	40.19	38.61	44.76	40.91	146.34
ΔV_{elstat}	-32.36	-32.59	-88.33	-32.23	-33.41	-34.76	-32.76	-75.99
ΔE_{disp}	-5.34	-5.37	-5.02	-5.35	-5.25	-4.94	-5.37	-5.06
ΔE_{oi}	-21.29	-21.52	-174.43	-21.19	-21.49	-26.00	-21.64	-170.86
ΔE_{σ}	-19.71	-19.94	-161.70	-19.63	-19.28	-23.05	-20.05	-154.29
ΔE_{π}	-1.58	-1.57	-12.73	-1.56	-2.21	-2.95	-1.59	-16.57
$\% \Delta V_{elstat}$[b]	54.9	54.8	33.0	54.8	55.6	52.9	54.8	30.1
$\% \Delta E_{disp}$[b]	9.0	9.0	1.9	9.1	8.7	7.5	9.0	2.2
$\% \Delta E_{oi}$[b]	36.1	36.2	65.1	36.1	35.7	39.6	36.2	67.7
ΔE_{Bond}	-16.77	-16.80	-21.77[c]	-16.64	-19.98	-17.98	-16.93	-32.07[c]

[a] Computed at BLYP-D3(BJ)/TZ2P with bases in C_1 symmetry and base pairs in C_s symmetry. [b] The percentage values give the contribution to the total attractive forces (i.e. $\Delta V_{elstat} + \Delta E_{oi} + \Delta E_{disp}$). [c] Proton transfer occurs in the N1···H3-N3 hydrogen-bond from uracil to adenine.

partitioning the complex into adenine and uracil while the H3-hydrogen atom gains much proton character because it is already far removed from uracil to which it was originally bound. Therefore, an additional analysis was performed for A$^{(NH^-)8}$-U and A$^{(O^-)8}$-U base pairs in terms of a neutral (N1-protonated X8-substituted) adenine and a negatively charged (N3-deprotonated) uracil fragmentation. Similarly, the A-U$^{(NH_3^+)6}$ and A-U$^{(OH_2^+)6}$ base pairs were analyzed using a positively charged (N1-protonated) adenine and a neutral (N3-deprotonated Y6-substituted) uracil interacting fragments. In this more realistic context, the orbital interactions yield again the well-known percentages of 35-36% (see Table 4.3).

Table 4.3. EDA analysis (in kcal·mol^{-1}) of the A^{X8}-U^{Y6} base pairs using interacting fragments that involves the H3-proton transfer[a]

X8	**NH$^-$**	**O$^-$**	H	H
Y6	H	H	**NH$_3^+$**	**OH$_2^+$**
ΔE_{prep}	4.57	4.43	4.28	---[c]
ΔE_{int}	-55.23	-57.56	-62.39	-54.24
ΔE_{Pauli}	48.71	50.03	47.68	42.26
ΔV_{elstat}	-61.53	-64.42	-66.41	-56.80
ΔE_{disp}	-5.53	-5.57	-5.72	-5.60
ΔE_{oi}	-36.87	-37.61	-37.94	-34.10
ΔE_{σ}	-29.91	-30.89	-33.05	-30.29
ΔE_{π}	-6.96	-6.72	-4.89	-3.81
% ΔV_{elstat}[b]	59.2	59.9	60.3	58.9
% ΔE_{disp}[b]	5.3	5.2	5.2	5.8
% ΔE_{oi}[b]	35.5	35.0	34.5	35.3
ΔE_{Bond}	-50.66	-53.13	-58.11	---[c]

[a] Computed at BLYP-D3(BJ)/TZ2P with bases in C_1 symmetry and base pairs in C_s symmetry. [b] The percentage values give the contribution to the total attractive forces (i.e. $\Delta V_{\text{elstat}} + \Delta E_{\text{oi}} + \Delta E_{\text{disp}}$). [c] Proton transfer occurred, making preparation energy not well defined.

As expected, in those instances in which the overall hydrogen-bond energy (ΔE_{Bond}) has been strengthened relative to the natural A-U base pair, the electrostatic (ΔV_{elstat}) and the orbital (ΔE_{oi}) energy terms always increase. For example, going from A-U to A$^{(\text{NH}_3^+)8}$-U, the ΔE_{Bond} increases from -16.8 to -19.7 kcal·mol^{-1}, as well as the electrostatic (from -32.4 to -33.4 kcal·mol^{-1}) and orbital interactions (-21.29 to -21.34 kcal·mol^{-1}). However, in those cases in which the ΔE_{Bond} decreases relative to the natural A-U base pair, we do not always see reduced the electrostatic and orbital interaction energies. Instead, these bonding energy terms are often even stabilized and the reduction in hydrogen-bond energy comes from both increased Pauli repulsion (ΔE_{Pauli}) and preparation energy (ΔE_{prep}). For example, going from A-U to A-U$^{(\text{NH}_2)6}$, the hydrogen-bond strength decreases from -16.8 to -16.4 kcal·mol^{-1}. Here, the ΔV_{elstat} is stabilized (from -32.4 to -32.8 kcal·mol^{-1}) and so is the ΔE_{oi} (from -21.3 to -21.4 kcal·mol^{-1}). Thus, the destabilization of the ΔE_{Bond} is now entirely contained in the increase of the Pauli repulsion (from 1.9 to 2.4 kcal·mol^{-1}) and the preparation energy (from 40.4 to 40.7 kcal·mol^{-1}).

This seemingly counterintuitive result can be understood if one realizes that the effects of introducing ionic substituents are relatively larger than those introducing neutral substituents. The characteristic changes in the geometric shape of the base pairs caused by ionic substituents (discussed in Section 4.3.1) also induce substantial changes in the individual components of the hydrogen-bond energy (ΔE_{Bond}). These changes in the geometry are the result of achieving a new balance between the repulsive and attractive forces that modify the individual contributions of the ΔE_{Bond}. On the other hand, the introduction of a neutral amino or hydroxyl substituent causes small alterations in hydrogen-bond lengths and energies, which hardly affects the bonding forces (*i.e.*, ΔE_{oi} + $\Delta V_{\mathrm{elstat}}$ + ΔE_{disp}). Instead, these slightly alterations of the hydrogen bonds are associated with (or occurs at the cost of) an increase in $\Delta E_{\mathrm{Pauli}}$ and ΔE_{prep}.

The substitution with halogens atoms along the Watson-Crick A^{X8}-U^{Y6} base pairs (X8, Y6 = F, Cl, Br) produces relatively insignificant changes if we compare with the much larger effects described above. Note that the substituent effects in uracil are more pronounced than those in adenine. This is in line with the fact that the pyrimidine base (uracil) is smaller than the purine base (adenine) and that its orbital energies are more strongly affected by the substituent. Thus, the percentage contribution of the orbital interactions (ΔE_{oi}) in the A-U^{Y6} base pairs are almost 1% larger than the orbital interactions in the A^{X8}-U base pairs, when only adenine carries a halogen at X8 (Table 4.4). The complete EDA of the A^{X8}-T^{Y6} and A^{X8}-U^{Y6} base pairs, including the results obtained with the S12g/TZ2P level are available in the Appendix 1.

Table 4.4. EDA analysis (in kcal·mol^{-1}) of the A^{X8}-U^{Y6} base pairs (halogen series)^{a}

X8	**F**	**Cl**	**Br**	H	H	H	**F**	**Cl**	**Br**
Y6	H	H	H	**F**	**Cl**	**Br**	**F**	**Cl**	**Br**
ΔE_{prep}	1.73	1.74	1.79	2.08	2.03	2.01	1.92	1.87	1.82
ΔE_{int}	-18.43	-18.49	-18.52	-19.30	-19.19	-19.18	-19.00	-18.95	-18.94
$\Delta E_{\mathrm{Pauli}}$	39.20	39.28	39.28	41.19	40.92	40.67	39.89	39.69	39.29
$\Delta V_{\mathrm{elstat}}$	-31.73	-31.80	-31.80	-32.99	-32.75	-32.62	-32.23	-32.07	-31.86
ΔE_{disp}	-5.32	-5.32	-5.32	-5.39	-5.38	-5.38	-5.35	-5.35	-5.35
ΔE_{oi}	-20.58	-20.65	-20.68	-22.12	-21.97	-21.85	-21.31	-21.22	-21.02
ΔE_{σ}	-19.05	-19.11	-19.13	-20.46	-20.31	-20.20	-19.71	-19.61	-19.43
ΔE_{π}	-1.53	-1.55	-1.55	-1.66	-1.66	-1.64	-1.60	-1.61	-1.59
% $\Delta V_{\mathrm{elstat}}{}^{b}$	55.1	55.0	55.0	54.5	54.5	54.5	54.7	54.7	54.7
% $\Delta E_{\mathrm{disp}}{}^{b}$	9.2	9.2	9.2	8.9	9.0	9.0	9.1	9.1	9.2
% $\Delta E_{\mathrm{oi}}{}^{b}$	35.7	35.8	35.8	36.6	36.5	36.5	36.2	36.2	36.1
ΔE_{Bond}	-16.70	-16.75	-16.73	-17.22	-17.16	-17.17	-17.08	-17.08	-17.12

[a] Computed at BLYP-D3(BJ)/TZ2P with bases in C_1 symmetry and base pairs in C_s symmetry.

[b] Percentage ΔE_{oi} of all attractive forces (i.e. $\Delta V_{\mathrm{elstat}}$ + ΔE_{oi} + ΔE_{disp}).

Next, we inspect the substituent effects on the VDD atomic charges of the front atoms (i.e., the ones that are involved in the hydrogen bonding) and the *C2-adenine* atom (see Figure 4.1). As shown in Table 4.5, introducing a neutral or halogen substituent at adenine X8 or uracil Y6 has little effect on the atomic charges of the front atoms. However, charged substituents have more pronounced effects: the negatively charged substituents (NH^- and O^-) inject an excess of negative charge into the base pairs and cause the H6 and H3 hydrogen atoms to become *less positive* by up to 0.020 electrons. Note also that the nitrogen and oxygen front atoms become *more negative* by up to 0.113 electrons, except in the $A^{(NH^-)8}$-U and $A^{(O^-)8}$-U base pairs where the proton transfer weakens the electrostatic attraction in the N1···H3–N3 hydrogen-bond and the adenine N1 atoms become *less negative* by 0.108 and 0.105 electrons, respectively.

In contrast, positively charged substituents (NH_3^+ and OH_2^+) cause the hydrogen front atoms to become more positive by up to 0.015 electrons, whereas nitrogen and oxygen front atoms become less negative by up to 0.116 electrons. Again, the electrostatic attraction in the N1···H3–N3 hydrogen-bond is decreased when the H3 atom is transferred

Table 4.5. VDD atomic charges Q_A (a.u.) in the front atoms and the adenine/uracil C2 carbon atoms of the A^{X8}-U^{Y6} base pairs.

X8	Y6	N6	H6	O4	N1	H3	N3	*C2-adenine*	*C2-uracil*
H	H	-0.171	0.136	-0.297	-0.186	0.151	-0.122	0.091	0.213
NH_2	NH_2	-0.176	0.130	-0.315	-0.186	0.149	-0.128	0.082	0.210
OH	OH	-0.174	0.133	-0.305	-0.184	0.151	-0.125	0.089	0.213
NH^-	H	-0.185	0.117	-0.349	-0.078	0.147	-0.235	0.059	0.192
NH_2	H	-0.177	0.133	-0.297	-0.185	0.152	-0.120	0.085	0.212
NH_3^+	H	-0.157	0.150	-0.293	-0.169	0.154	-0.118	0.113	0.214
O^-	H	-0.184	0.120	-0.347	-0.081	0.148	-0.234	0.064	0.192
OH	H	-0.175	0.136	-0.298	-0.184	0.152	-0.119	0.090	0.212
OH_2^+	H	-0.156	0.151	-0.292	-0.166	0.154	-0.118	0.116	0.214
H	NH^-	-0.175	0.122	-0.377	-0.192	0.131	-0.136	0.092	0.197
H	NH_2	-0.171	0.133	-0.314	-0.188	0.148	-0.128	0.091	0.211
H	NH_3^+	-0.155	0.148	-0.289	-0.073	0.162	-0.220	0.107	0.207
H	O^-	-0.175	0.124	-0.370	-0.192	0.132	-0.135	0.093	0.196
H	OH	-0.171	0.135	-0.305	-0.187	0.151	-0.128	0.091	0.216
H	OH_2^+	-0.153	0.151	-0.274	-0.070	0.165	-0.218	0.108	0.213
F	H	-0.171	0.139	-0.296	-0.183	0.153	-0.119	0.095	0.212
Cl	H	-0.172	0.137	-0.296	-0.185	0.155	-0.121	0.092	0.214
Br	H	-0.171	0.136	-0.298	-0.187	0.153	-0.119	0.092	0.212
H	F	-0.171	0.137	-0.292	-0.185	0.152	-0.126	0.092	0.219
H	Cl	-0.171	0.137	-0.292	-0.186	0.152	-0.126	0.091	0.216
H	Br	-0.170	0.138	-0.292	-0.186	0.151	-0.125	0.091	0.216
F	F	-0.171	0.139	-0.291	-0.183	0.154	-0.123	0.094	0.217
Cl	Cl	-0.171	0.140	-0.291	-0.184	0.153	-0.122	0.095	0.214
Br	Br	-0.172	0.140	-0.292	-0.185	0.153	-0.123	0.094	0.216

as a proton (A-U$^{(NH_3^+)6}$ and in A-U$^{(OH_2^+)6}$ base pairs) and the uracil N3 atoms become more negative by up to 0.098 electrons. Halogen substituents cause relatively small effects on the VDD atomic charges. In line with the higher electronegativity of the halogen atoms, the hydrogen front atoms are slightly more positive by up to 0.004 electrons, whereas nitrogen and oxygen atoms are in most cases slightly less negative by up to 0.006 electrons.

For a better understanding, the atomic charges of *C2-adenine/uracil* atoms will be discussed in the next section and the complete VDD description of the A^{X8}-T^{Y6} and A^{X8}-U^{Y6} base pairs is available in the Appendix A1, Tables A1.1- A1.2. We therefore proceed to analyze the main results of our work, the NMR chemical shielding constants.

4.3.3 NMR Chemical Shielding Constants

As mentioned before, the presence of a methyl group at the pyrimidine ring (*e.g.*, A-T *versus* A-U) has two effects: it decreases the hydrogen-bond strength, and it decreases the NMR shielding at the adenine *C*2 atom. However, a correlation between these two effects was arguable. Since we now have ample data for the influence of the hydrogen bond strength by varying the X8 and Y6 substituents, we have analyzed in detail if the NMR *C2-adenine* and *C2-thymine/uracil* shielding constants correlate with the hydrogen-bond strength.

Let us first focus our attention on the NMR *C2-adenine* shielding (σ) constants of the isolated adenine (A^{X8}) bases (see Table 4.6). Neutral substituents (NH_2 and OH) at X8 have little effect on the shielding values. However, the presence of charged substituents induces an interesting and significant variation. Introducing a negatively charged group at X8 increases the *C2-adenine* shielding (σ). If we examine the results obtained at the SAOP/TZ2P level, substituent NH^- at X8 causes an increase of the shielding from 29.4 to 43.6 ppm. In contrast, a positively charged group at X8 decreases σ, *e.g.* substituent NH_3^+ induces a deshielding of -5.7 ppm (see Δσ (A^{X8}), Table 4.6). These tendencies are easily understood in terms of the charge transfer between the *C2-adenine* atom and the electron-donating/withdrawing capacity of the substituents at the X8 position. If we inspect the VDD atomic charges of the adenine *C*2 atom, a negatively charged substituent causes *C*2 to become *less positive* by up to 0.032 electrons, whereas a positively charged substituent causes the *C*2 atom to become more positive by up to 0.025 electrons. In the

Table 4.6. NMR *C2-adenine* shielding (σ) values (ppm) computed at the SAOP/TZ2P level for the isolated adenine (A^{X8}) bases and A^{X8}-T base pairs[a]

X8	Adenine (A^{X8})		A^{X8}-T		ΔΔ(σ)[c]	VDD charges[d]	
	C2 (σ)	Δσ	*C2* (σ)	Δσ		Q_A	ΔQ_A
H	29.39	0.00	30.66	0.00	0.00	0.092	0.000
NH^-	43.59	14.20	52.04[b]	21.38	7.18[b]	0.060	-0.032
NH_2	32.59	3.20	33.66	3.00	0.20	0.084	-0.008
NH_3^+	23.68	-5.71	24.88	-5.78	0.07	0.115	0.023
O^-	41.53	12.15	50.13[b]	19.47	7.33[b]	0.065	-0.027
OH	30.80	1.42	31.91	1.25	0.17	0.088	-0.004
OH_2^+	23.05	-6.34	24.31	-6.35	0.01	0.117	0.025
F	29.31	-0.07	30.39	-0.27	0.20	0.092	0.000
Cl	29.32	-0.07	30.48	-0.18	0.11	0.096	0.004
Br	29.67	0.28	30.81	0.15	0.13	0.092	0.000

[a] Geometries optimized at the BLYP-D3(BJ)/TZ2P level. [b] Proton transfer occurs in the N1···H3-N3 hydrogen-bond from thymine to adenine. [c] Absolute ΔΔ(σ) calculated as Δσ (A^{X8}-T) - Δσ (A^{X8}). [d] VDD atomic charges Q_A (a.u.) in the *C2-adenine* atom of the A^{X8}-T base pairs.

case of the halogen substituents, the shielding becomes larger as the halogen becomes heavier and contains more electrons (see Table 4.6). At the same time, the change in shielding follows the electronegativity values for these halogens: a larger electronegativity can be associated with a larger electron-withdrawing effect and hence should lead to a smaller shielding at C2. This is indeed what we observe here (Table 4.6).

Compared to the isolated adenine (A^{X8}) bases, the *C2-adenine* shielding (σ) values along the A^{X8}-T base pairs remain essentially unaffected (see Table 4.6). Here, we analyzed the A^{X8}-T base pairs, but similar arguments hold for the A^{X8}-U base pairs (see Appendix A1, Table A1.3). As expected, we find a linear correlation between the A^{X8} and A^{X8}-T *C2-adenine* shielding values (see Fig. 4.3). In agreement with this, the overall differences between the Δσ (A^{X8}) and Δσ (A^{X8}-T) values (see ΔΔ(σ), Table 4.6) are very small, on the order of 0.1-0.2 ppm (this difference is mainly an electronic effect, and not geometric, see Appendix 1, Table A1.4). The only exception is found for $A^{(NH^-)8}$-T and $A^{(O^-)8}$-T where a proton transfer from thymine to adenine has taken place, which for obvious reasons leads to significant changes in the electronic structure of the adenine. This leads us to the important conclusion that the largest part of the change in the *C2-adenine* shielding values comes from the substituents, and is hardly influenced by the formation of the hydrogen bonds in the base pair. In general, an intrinsic increase in the *C2-adenine* shielding for all of the A^{X8}-T base pairs (irrespective of the substituents) is observed caused by the presence

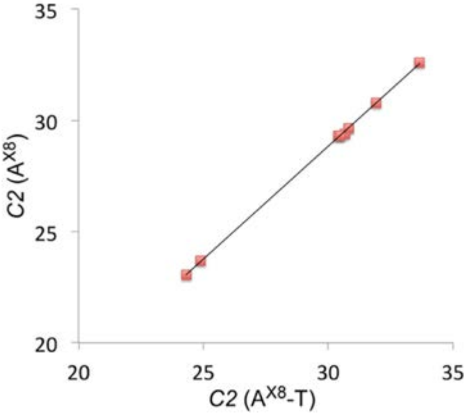

Figure 4.3. Calculated correlation between the *C2-adenine* shielding values (ppm) of isolated adenine (A^{X8}) bases and A^{X8}-T base pairs. The proton transfer systems were not included in the plot, due to their particular behavior.

of the aromatic ring next to it (thymine), *i.e.* the *C2-adenine* shielding increases from 29.39 to 30.66 ppm when X8 = H (see Table 4.6), which is conserved for the different substituents.

In order to corroborate the correlation described above, we also examined the NMR *C2-thymine* shielding (σ) constants of the isolated thymine (T^{Y6}) bases and the A-T^{Y6} base pairs (see Table 4.7). Here, the introduction of a negatively charged group at Y6 decreases the *C2-thymine* shielding in T^{Y6}. For instance, substituent NH^- at Y6 decreases the *C2-thymine* shielding from 35.2 to 33.0 ppm. On the other hand, a positively charged group at Y6 increases σ, *e.g.* substituent NH_3^+ induces an increase of 5.8 ppm. In this case, these tendencies cannot be supported in terms of the charge transfer between the *C2-thymine* atom and the electron-donating/withdrawing capacity of the substituents at the Y6 position. A negatively charged substituent causes the VDD atomic charge of the thymine C2 atom to become slightly *less positive* (by up to 0.016 electrons), while a positively charged substituent has little effect on the thymine C2 VDD charge.

Furthermore, a clear pattern again emerges (similar to Figure 4.3) from the comparison between the *C2-thymine* shielding values along the T^{Y6} and A-T^{Y6} model systems (see Appendix A1, Fig. A1.1). The only two cases that present an increase of the ΔΔ(σ) values are A-$T^{(NH_3^+)6}$ and A-$T^{(OH_2^+)6}$, as a consequence of the proton transfer that occurs from thymine to adenine.

Table 4.7. NMR *C2-thymine* shielding (σ) values (ppm) computed at the SAOP/TZ2P level for the isolated thymine (T^{Y6}) bases and A-T^{Y6} base pairs[a]

Y6	Thymine (T^{Y6})		A-T^{Y6}		ΔΔ(σ)[c]	VDD charges[d]	
	C2 (σ)	Δσ	*C2* (σ)	Δσ		Q_A	ΔQ_A
H	35.16	0.00	34.00	0.00	0.00	0.208	0.000
NH^-	32.97	-2.20	32.89	-1.11	1.08	0.194	-0.014
NH_2	36.78	1.61	36.11	2.11	0.49	0.209	0.001
NH_3^+	41.01	5.84	35.20[b]	1.20	4.64[b]	0.205	-0.003
O^-	32.81	-2.36	32.60	-1.40	0.96	0.192	-0.016
OH	37.65	2.49	36.75	2.76	0.26	0.210	0.002
OH_2^+	43.39	8.23	36.63[b]	2.63	5.60[b]	0.210	0.002
F	38.48	3.32	37.09	3.09	0.23	0.212	0.004
Cl	37.65	2.49	36.52	2.52	0.03	0.208	0.000
Br	37.54	2.38	36.34	2.34	0.04	0.208	0.000

[a] Geometries optimized at the BLYP-D3(BJ)/TZ2P level. [b] Proton transfer occurs in the N1···H3-N3 hydrogen-bond from thymine to adenine. [c] Absolute ΔΔ(σ) calculated as Δσ (A-T^{Y6}) - Δσ (T^{Y6}). [d] VDD atomic charges Q_A (a.u.) in the *C2-thymine* atom of the A-T^{Y6} base pairs.

In the same manner, we explored the dependence of the NMR *C2*-shielding constants as a function of the hydrogen-bond strength. For a better understanding, we examined the results of the *C2-adenine* and *C2-thymine* shielding values in two separate plots, along the A^{X8}-T and A-T^{Y6} base pairs (see Fig. 4.4). Looking at Figure 4.4a, one might be tricked into thinking that there is some kind of relationship between the *C2-adenine* shielding and the hydrogen-bond strength in the A^{X8}-T base pairs. Nevertheless, this influence clearly disappears when a Y6 substituent is introduced at the thymine ring (see Fig. 4.4b). For example, if we compare with A-T, the NMR *C2-adenine* shielding in A-$T^{(NH^-)6}$ decreases from 30.7 to 29.4 ppm, whereas the hydrogen-bond strength increases from -16.5 to -17.9 kcal·mol^{-1}. This is opposite to the effect from A-T to A-U, where the *C2-adenine* shielding and the hydrogen-bond strength both increase by 0.107 ppm and 0.3 kcal·mol^{-1}, respectively (at the SAOP/TZ2P level). In this way, it is clearly seen that a larger shielding does not necessarily correspond to a stronger interaction. Consistent with these findings are the results for the *C2-thymine* shielding values along the A^{X8}-T and A-T^{Y6} base pairs (see Fig. 4.4c and d). When a substituent is at the X8 position (see Fig. 4.4c), the *C2-thymine* shielding may appear to have a correlation with the hydrogen-bond strength. However, when a substituent is at the Y6 position (see Fig. 4.4d), the lack of correlation between the *C2-thymine* shielding and the hydrogen-bond strength is very clear. We plot here only the A^{X8}-T^{Y6} data but the A^{X8}-U^{Y6} base pairs lead to similar conclusions (see Appendix 1, Fig. A1.2).

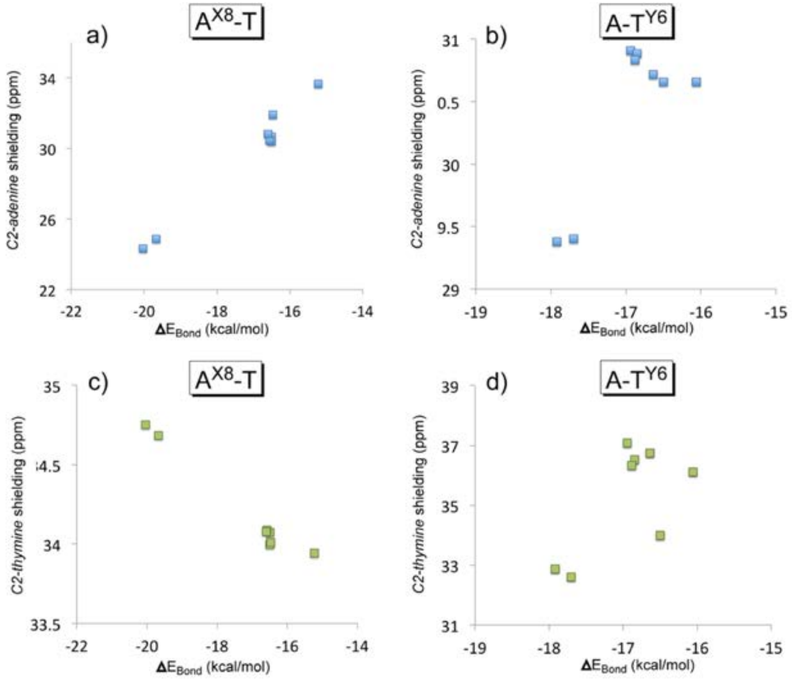

Figure 4.4. Calculated dependence of the NMR *C*2-shielding values (ppm) as a function of the hydrogen-bond strength (kcal·mol^{-1}). **(a)** *C2-adenine* shielding of A^{X8}-T, **(b)** *C2-adenine* shielding of A-T^{Y6}, **(c)** *C2-thymine* shielding of A^{X8}-T, and **(d)** *C2-thymine* shielding of A-T^{Y6} base pairs. The proton transfer systems were not included in the plot, due to their particular behavior.

Finally, we wanted to illustrate our study with a biological model that occurs in DNA and RNA. Thus, we explored the interaction of adenine, thymine and A-T structures with a monovalent K$^+$ cation and two water molecules (see Fig. 4.5). We limit the optimizations to the planar C_s symmetry, where the K$^+$ cation interacts with the N7 nitrogen atom of adenine or the O4/O2 oxygen atoms of thymine. These positions are known[113] to be one of the actives sites for the interaction of metal ions with nucleic acids in various biological systems.

As expected, the K$^+$···2H$_2$O acts as a positively charged substituent, similarly to adding NH$_3$$^+$/OH$_2$$^+$ substituents that led to a decrease of the *C2-adenine* shielding when introduced at the X8 position (see Table 4.6) and an increase of the *C2-thymine* shielding when added at the Y6 position (see Table 4.7). For K$^+$···2H$_2$O, if we compare with the

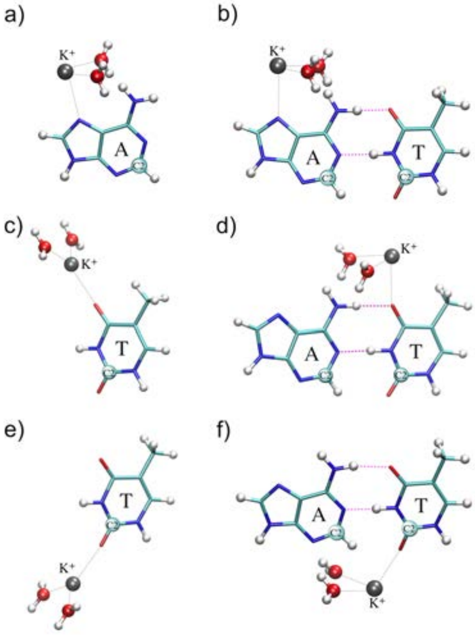

Figure 4.5. Structures of adenine, thymine and A-T base pair interacting with a K^+ cation and two water molecules.

isolated adenine base, the *C2-adenine* shielding of the [adenine···K^+(N7)···$2H_2O$] model structure (see Fig. 4.5a) decreases from 29.4 to 26.6 ppm (see Table 4.8). On the other hand, if we compare with the isolated thymine base, the *C2-thymine* shielding of the [thymine···K^+(O4)···$2H_2O$] model structure (see Fig. 4.5c) increases from 35.2 to 37.5 ppm. Similar effects are observed when the K^+···$2H_2O$ is positioned next to the A-T base pair at either the N7(A) or O4(T) position (see Table 4.8).

Finally, if we explore the dependence of the NMR *C2-adenine* constants as a function of the hydrogen-bond strength in the above (A-T)···K^+···$2H_2O$ model structures, the lack of correlation between NMR shielding constants and hydrogen-bond strengths is observed again (see Figure 4.6). Compared to the natural A-T base pair, the NMR *C2-adenine* shielding in the [$2H_2O$···K^+(N7)···A-T] model structure (see Fig. 4.5b) decreases from 30.7 to 27.7 ppm, whereas the hydrogen-bond strength increases from -16.5 to -20.5 kcal·mol^{-1}. Therefore, as already demonstrated above, this behaviour is completely opposite to the effect that a methyl group at the 5 position has (A-T *vs.* A-U). In the latter case (A-T vs.

Table 4.8 NMR *C2-adenine/thymine* shielding (σ) values (ppm) computed at the SAOP/TZ2P level for adenine, thymine and A-T base pair interacting with a K^+ cation and two water molecules[a]

Structure	*C2-adenine*	*C2-thymine*	ΔE_{Bond}
Adenine	29.39	---	---
Thymine	---	35.16	---
A-T	30.66	34.00	-16.50
a) K^+(N7)···Adenine	26.62	---	---
b) K^+(N7)···A-T	27.73	34.80	-20.54
c) Thymine···K^+(O4)	---	37.45	---
d) A-T···K^+(O4)	30.57	35.61	-17.80
e) Thymine···K^+(O2)	---	31.70	---
f) A-T···K^+(O2)	32.33	31.86	-30.58

[a] Geometries optimized at the BLYP-D3(BJ)/TZ2P level.

A-U) both the NMR shielding and hydrogen-bond strength increase, while in the case of K^+(N7) the hydrogen-bond strength increases but the NMR shielding decreases.

The main conclusion from the computational experiments by adding $K^+\cdots 2H_2O$ next to the A-T base pair is however that the substituent effects of adding charged ligands in the supramolecular switches are not limited to these "artificial" species. Similar trends of changes in hydrogen-bond strengths and NMR shielding constants are observed in the presence of potassium ions close to the DNA/RNA bases. This latter situation occurs

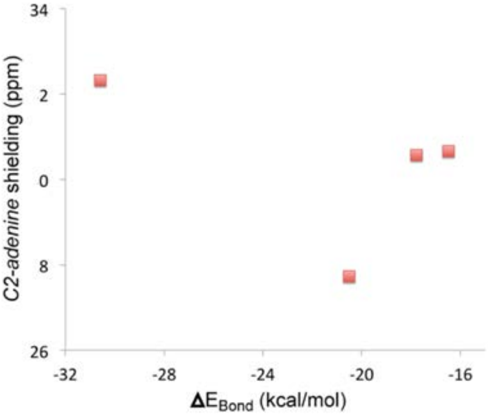

Figure 4.6. Calculated dependence of the NMR *C2-adenine* shielding values (ppm) as a function of the hydrogen-bond strength (kcal·mol^{-1}) of the natural A-T, and the [K^+(N7)···A-T], [A-T···K^+(O4)] and [A-T···K^+(O2)] model structures.

naturally in biological systems, in the minor and major grooves, which will have significant effects on the hydrogen-bond strengths and NMR shielding constants of the corresponding base pairs.

In this chapter, we have analyzed in detail the effect of neutral and ionic substituents at the adenine X8 and thymine/uracil Y6 positions on the hydrogen-bond strength, NMR chemical shielding and charge distributions within the DNA/RNA base pairs A-T and A-U. Our study at the BLYP-D3(BJ)/TZ2P level for geometry and energy show that in most cases the RNA base pair is slightly more strongly bound than the DNA base pair. Introducing substituents at the adenine X8 and thymine/uracil Y6 positions can lead to significant changes in the hydrogen bonding: from a destabilization by 1.3 kcal·mol^{-1} to a strong stabilization by 15.6 kcal·mol^{-1}, depending on the nature and position of the substituent. The NMR shielding constants are likewise affected substantially: the NMR *C2-adenine* shielding shows changes within a range of 8 ppm decrease up to 24 ppm increase. Most importantly, these NMR shielding values merely probe the presence/absence of (electron-donating/withdrawing) substituents at adenine X8 and thymine/uracil Y6 positions. The substituents affect both NMR shielding constants and hydrogen-bond strengths. However, these are two independent and uncorrelated effects.

We have also investigated a biologically relevant situation where a partially dehydrated potassium cation binds to the DNA base. Also, in this case, the influence of the potassium cation on the hydrogen-bond strength does not correlate with the NMR shielding. Not surprisingly, the presence of a cationic species close to the DNA/RNA bases has a profound effect on their electronic structure, thus leading to significant changes in the hydrogen-bond strength and NMR shielding constants. These changes are observed irrespective of whether the cations are covalently (supramolecular switches) or weakly bonded (potassium cations).

Chapter 5

Four-component Relativistic ^{31}P-NMR calculations in *trans*-platinum(II) complexes: Importance of the Solvent and Dynamics in Spectral simulations[a]

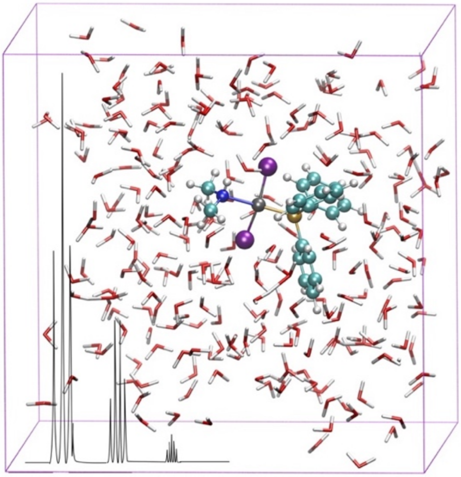

---

[a] This chapter is based on the publication: A. C. Castro, H. Fliegl, M. Cascella, T. Helgaker, M. Repisky, S. Komorovsky, M. A. Medrano, A. G. Quiroga, M. Swart, Four-component relativistic ^{31}P-NMR calculations in *trans*-platinum(II) complexes: Importance of the solvent and dynamics in spectral simulations. *To be submitted.*

SUMMARY

In this chapter, we have focused on the theoretical determination of the ^{31}*P-NMR chemical shifts of the trans-*[$PtCl_2$*(dimethylamine)*PPh_3] *complex and species derived from its hydrolysis, in an attempt to understand its mechanism of action as anticancer platinum drug.*

The ^{31}*P-NMR chemical shifts were computed using ab-initio molecular dynamics simulations with DFT-NMR calculations on a large series of snapshots. Comparing with experimental spectra, we show the importance of relativistic effects, dynamics, and explicit solvation for the accurate modeling of the* ^{31}*P-NMR chemical shifts.*

EMBARGOED UNTIL PUBLICATION DATE

Chapter 6

Computational NMR Spectroscopy for Host-Guest Hemicarcerands[a]

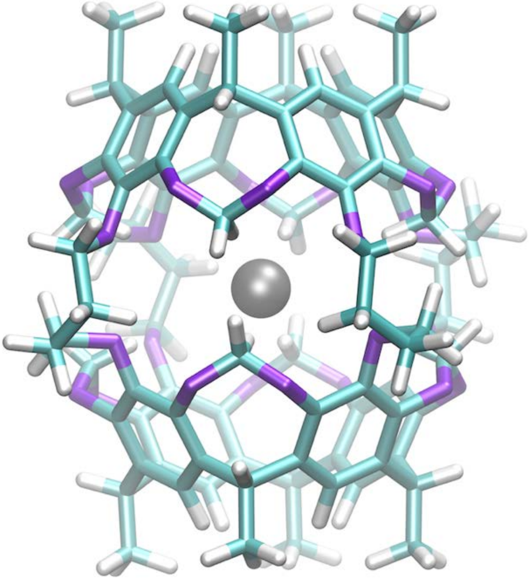

[a] This chapter is based on the publication: A. C. Castro, A. Romero, S. Osuna, K. N. Houk, M. Swart, Computational NMR Spectroscopy for Host-Guest Hemicarcerands. *To be submitted.*

SUMMARY

In this chapter, the incarceration of o-benzyne and other 27 guest molecules within hemicarcerand **1***, studied experimentally by Warmuth, and Cram and co-workers, respectively, has been studied via density functional theory (DFT). The possible incarceration of o-benzyne within a second hemicarcerand* **2** *as synthesized by Cram and co-workers has also been explored. Full structure optimization and determination of the* ^{1}*H-NMR chemical shifts were performed. In addition, the rotational mobility and the conformational preference of the guest molecules inside the hemicarcerand structures were explored, providing intriguing correlations of the chemical shifts with structural parameters of the host-guest system. Our proton NMR chemical shifts at the KT2/ET-pVQZ level indicate in most of the cases a direct correlation between theoretical calculations and experimental measurements, and provide a new strategy to characterize these challenging host-guest complexes.*

EMBARGOED UNTIL PUBLICATION DATE

Chapter 7

Exploring the potential energy surface of E_2P_4 clusters (E= Group 13 elements): The quest for inverse carbon-free sandwiches[a]

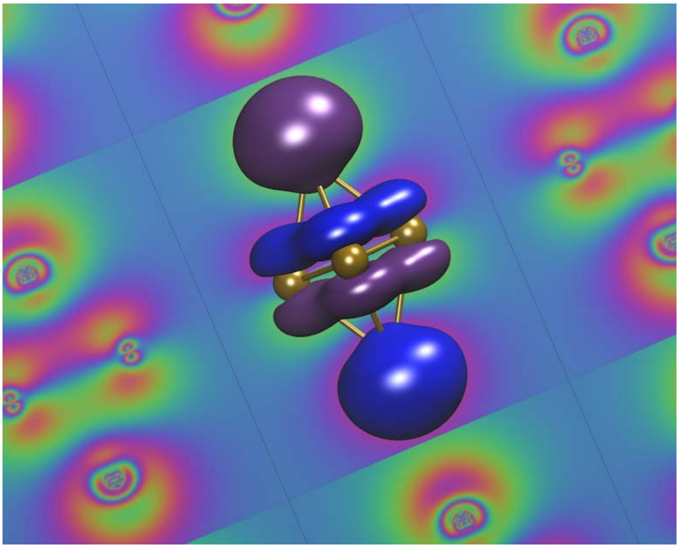

---

[a] This chapter is based on the publication: A. C. Castro, E. Osorio, J. L. Cabellos, E. Cerpa, E. Matito, M. Solà, M. Swart, G. Merino, *Chem. Eur. J.*, **2014**, 20, 4583- 4590. [cover: Chem. Eur. J. 16/2014.]

SUMMARY

In this chapter, inverse carbon-free sandwich structures with formula E_2P_4 (E= Al, Ga, In, Tl) have been proposed as a promising new target in main-group chemistry. Our computational exploration of their corresponding potential-energy surfaces at the S12h/TZ2P level shows that indeed stable carbon-free inverse-sandwiches can be obtained if one chooses an appropriate Group 13 element for E. The boron analogue B_2P_4 does not form the D_{4h}-symmetric inverse-sandwich structure, but instead prefers a D_{2d} structure of two perpendicular BP_2 units with the formation of a double B-B bond. For the other elements of Group 13, Al-Tl, the most favorable isomer is indeed the D_{4h} inverse-sandwich structure. The preference for the D_{2d} isomer for B_2P_4 and D_{4h} for the heavier analogues has been rationalized in terms of an isomerization-energy decomposition analysis, and further corroborated by determination of aromaticity of these species. Additionally, the prediction of the ^{31}P-NMR shielding constants was carried out for the most stable structures.

7.1 State of the art

Coordination chemistry of the monovalent Group 13 elements has become an exciting topic in main group chemistry, because the metal center can act as a good electron-rich σ-donor ligand.[209-212] Particularly, half-sandwich complexes containing monovalent elements of Group 13 are one of the most important sets of cyclopentadienyl (Cp) compounds.[213-217] In 2006, the group of Fischer reported the synthesis of an inversed sandwich complex $[Ga\text{-}Cp^*\text{-}Ga]^+$ through treatment of $GaCp^*$ with one-half molar equivalent of $[H(OEt_2)_2][B\{C_6H_3(CF_3)_2\}_4]$. The complex has a symmetric bipyramidal double cone form with both gallium atoms collinear with the C_5 symmetry axis and it can react with electron-rich d^{10} platinum(0) complexes.[218-222]

Some years ago, some of us reported an extensive computational study of the symmetrical and unsymmetrical inverse sandwiches with formula $[E\text{-}Cp\text{-}E']^+$ (E and E′= Group 13 element, see Figure 7.1a).[223] We found that while the most favorable dissociation pathway for the boron complex $[B\text{-}Cp\text{-}B]^+$ is the loss of a neutral boron atom, the heavier homologues $[E\text{-}Cp\text{-}E]^+$ (E= Al-Tl) dissociate through the loss of the charged E^+ fragment. Computations show that among the $[E\text{-}Cp\text{-}E]^+$ complexes, the gallium compound has the highest stability. Quite recently, Liu *et al.* designed, *in silico,* another type of inverse sandwich $[E\text{-}C_4H_4\text{-}E]$ (E= Al-Tl), replacing the Cp anion by the $C_4H_4^{2-}$ dianion (Figure 7.1b).[224] Computations indicate that $[E\text{-}C_4H_4\text{-}E]$ dissociates homolytically through the loss

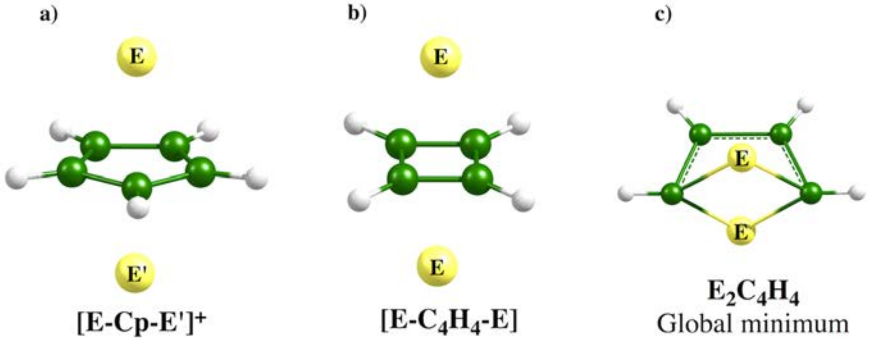

Figure 7.1. Inverse sandwich structures of **a)** cationic $[E\text{-}Cp\text{-}E']^+$ (E and E′= B-Tl), **b)** neutral $[E\text{-}C_4H_4\text{-}E]$ (E= Al-Tl) and **c)** global minimum $E_2C_4H_4$ (E = Al-Tl) as proposed by Liu *et al.*

of the neutral atom E with bond strengths following the trend Al > Ga > In > Tl. However, the inverse sandwich structure is only kinetically stable against isomerization, that is, the lowest-energy form is a bicyclic structure (see Figure 7.1c).

The question therefore arises if it is possible to stabilize these inverse sandwiches by using a carbon-free ligand. Baudler and Glinka suggested a diagonal relationship between carbon and phosphorus.[225-228] This "carbon-like" aspect of phosphorus is evident in the analogies of hydrocarbons with polyphosphanes or polyphosphides. In this sense, it is not strange to see a connection between $C_4H_4^{2-}$ and P_4^{2-}. The cyclotetraphosphide P_4^{2-} dianion and its derivatives have been subject to numerous experimental and theoretical studies.[229] In 2003, Kraus *et al.* succeeded in isolating the compound $Cs_2P_4{\cdot}2NH_3$ that contains a square and perfectly planar 6π-aromatic P_4^{2-} unit.[229] Inspired by these findings, in this paper we have explored in detail the potential energy surfaces (PESs) of the E_2P_4 (E= Group 13 element) clusters using a modified Kick algorithm.[230,231] We find that the stabilization of inverse sandwiches depends on the electronegativity and size of the Group 13 atoms. Our results show that while the most stable structure for B_2P_4 is the combination of two perpendicular BP_2 triangles connected by a multiple B-B bond, the inverse D_{4h} sandwich is the global minimum for E= Al, Ga, In, and Tl. Therefore, it is possible to stabilize a carbon-free inverse sandwich by selecting the appropriate Group 13 atoms. To understand the bonding in the E_2P_4 clusters, we performed an energy decomposition analysis (EDA)[105,106,232,233] and an adaptive natural density partitioning (AdNDP) analysis.[234] However, neither approach provides an explanation about the structural preferences. So, in order to understand why B_2P_4 chooses a D_{2d} structure, an isomerization energy decomposition analysis (IEDA)[235] was performed.

7.2 Computational Methods

Our computational procedure utilized a modified Kick heuristic[230,231] to explore in detail the potential-energy surfaces (PESs) of the singlet and triplet states of the E_2P_4 clusters. The lowest-lying structures found within 20 kcal $\cdot$mol^{-1} above the global minimum for the different Group 13 elements (at the PBE0/LANL2DZ level)[132,236] were selected for re-optimization and frequency analysis with the Amsterdam Density Functional (ADF, version 2012.01)[87,88] program using the S12h functional,[98] which contains Grimme's third-generation dispersion energy,[90] in conjunction with uncontracted basis sets of Slater-type orbitals (STOs) of triple-ζ quality plus double polarization functions (TZ2P).[96] The geometry optimizations and the vibrational frequency analysis of the optimized structures were carried out using the QUILD program[98] that contains superior optimization routines based on adapted delocalized coordinates.[237] For heavy atoms such as indium and thallium, scalar relativistic effects were considered using the zero-order regular approximation (ZORA).[24,25,137-139]

To gain more insight into the nature of the bonding in these clusters, an energy decomposition analysis (EDA)[105,106,232,233] was performed as implemented in the ADF2012 package at the S12h/TZ2P level. In this study, the preparation energy, ΔE_{prep}, is the energy needed to prepare the ionic fragments and consist of two principal terms. The first is the energy needed to deform the separate molecular fragments (in this case only for the P_4^{2-} dianion) from their equilibrium structure to the geometry that they attain in the overall molecular system ($\Delta E_{\mathrm{deform}}$), and the second ($\Delta E_{\mathrm{E-E}}$) is the (repulsive) interaction energy between the two E^+ cations, which results from electrostatic repulsion between the positively charged E^+ atoms, while making one fragment file that contains both $(E\cdots E)^{2+}$ atoms. Additional details of the EDA analysis can be consulted in Chapter 4, section 4.2.1.

The chemical bonding was also analyzed in terms of the adaptive natural density partitioning (AdNDP) method,[234] recently developed and implemented by Zubarev and Boldyrev. The AdNDP approach leads to partitioning of the charge density into elements with the lowest possible number of atomic centers per electron pair: n-center-two-electron (nc-2e) bonds, including core electrons, lone-pairs, (2c-2e) bonds, and so on. If some part of the electron density cannot be localized in this way, it is represented by using completely delocalized objects, similar to canonical MOs, incorporating the idea of the completely delocalized bonding. AdNDP accepts only those bonding elements the occupation numbers (ON) of which exceed the specified threshold values, which are usually chosen to be close to 2.00 |e|. However, the criterion for ONs can be adjusted for a particular case in the AdNDP procedure. When all the recovered (nc-2e) bonding elements are superimposed onto the molecular frame, the overall pattern always corresponds to the point group symmetry of the system. The AdNDP computations have been performed at the PBE0/LANL2DZ level.

Aromaticity calculations using the I_{NB} multicenter index[238] and electron delocalization analysis have been performed at the PBE0/def2-TZVP level. I_{NB} indices were computed by using a modified Becke-rho[239] atomic partition[240] and they were computed using APOST-3D[241,242] and ESI-3D[243,244] packages.

The prediction of the ^{31}P-NMR shielding constants was carried out for the most stable isomers using the ADF program, version 2016.01, with the KT2 functional[6] in conjunction with the even-temperate (ET) STO-type (ET-pVQZ)[97] basis set. Scalar (SR) and spin-orbit (SO) relativistic effects were included at the two-component level using the ZORA approximation and all the shielding constants were calculated using the Gauge Including Atomic Orbital (GIAO) method[245] to treat the gauge dependence problem.

7.3 Results and Discussion

7.3.1 Structures

Figure 7.2 summarizes the different local minima found on the B_2P_4 PES. Our computations reveal an ample diversity of structures within the range of 20 kcal·mol^{-1}, with structure **1a** being the most stable form. **1a** can be described as two perpendicular BP_2 triangles connected by a short B-B bond of 1.609 Å, which is similar to bond lengths characterized experimentally for B-B multiple bonds in some complexes.[246] Indeed, the B=B double bond length in species $[\{(Et_2O)Li\}_2\{Mes_2BB(Mes)Ph\}]$[247] was found to be 1.636(11) Å, which is quite close to the bond length found for B_2P_4 and similar to other analogous structures containing B=B double bonds.[248-250] The HOMOs are a degenerate pair of twisted π orbitals, indicating the presence of a multiple bond, which is weaker than that of the linear OC-B≡B-CO complex, because the overlap is less effective (see Figure 7.3). The second low-lying isomer **1b** is a C_{2v} planar entity, which is in competition to **1a** (it is only 0.5 kcal·mol^{-1} less stable than **1a**). Note that all the B_2P_4 isomers found in the selected range retain the B-B bond with distances between triple (1.583 Å) and single bonds (1.839 Å). This suggests that in B_2P_4 clusters, the formation of the B-B bonds is a dominant factor in their stability. The inverse sandwich **1j** is a transition state and is higher in energy than the global minimum by 109.6 kcal·mol^{-1}. The triplet forms are not competitive; the most

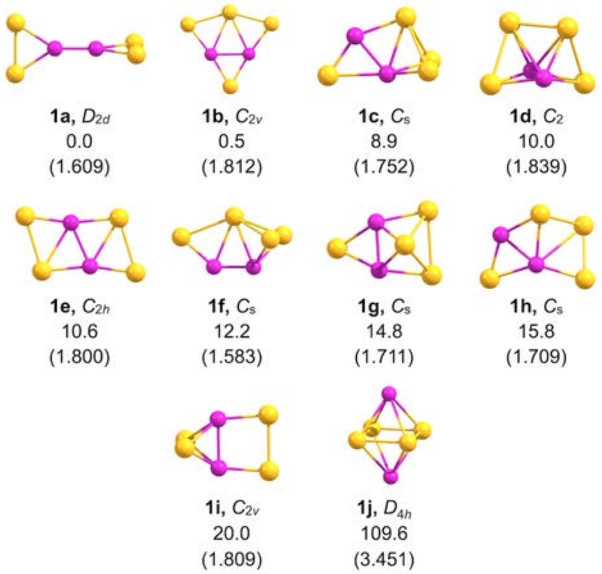
1a, D_{2d}
0.0
(1.609)
1b, C_{2v}
0.5
(1.812)
1c, C_s
8.9
(1.752)
1d, C_2
10.0
(1.839)
1e, C_{2h}
10.6
(1.800)
1f, C_s
12.2
(1.583)
1g, C_s
14.8
(1.711)
1h, C_s
15.8
(1.709)
1i, C_{2v}
20.0
(1.809)
1j, D_{4h}
109.6
(3.451)

Figure 7.2. Lowest-lying structures of the B_2P_4 cluster computed at the S12h/TZ2P level. Relative energies are given in kcal mol^{-1}. In parentheses are the B-B bond lengths in Å. All structures are local minima on its corresponding PES, except **1j**, which is a transition state.

stable triplet is less stable than **1a** by 63.7 kcal mol^{-1}.

The topology of the PES for the heavier analogues changes drastically (see Figure 7.4). For Al, Ga, In, and Tl, the lowest-lying isomer is a perfect D_{4h}-symmetric inverse sandwich (**2a**). The P-P bond lengths (~2.155 Å) are only slightly longer than those found for the naked P_4^{2-} dianion (2.142 Å),[229] indicating that the presence of the Al^+, Ga^+, In^+, or Tl^+

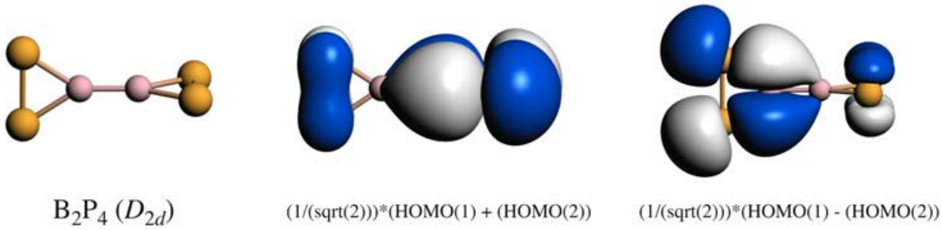
B_2P_4 (D_{2d})
(1/(sqrt(2)))*(HOMO(1) + (HOMO(2))
(1/(sqrt(2)))*(HOMO(1) - (HOMO(2))

Figure 7.3. Structure of [(HOMO)+(HOMO-1)] and [(HOMO)-(HOMO-1) of the B_2P_4 (D_{2d}) cluster.

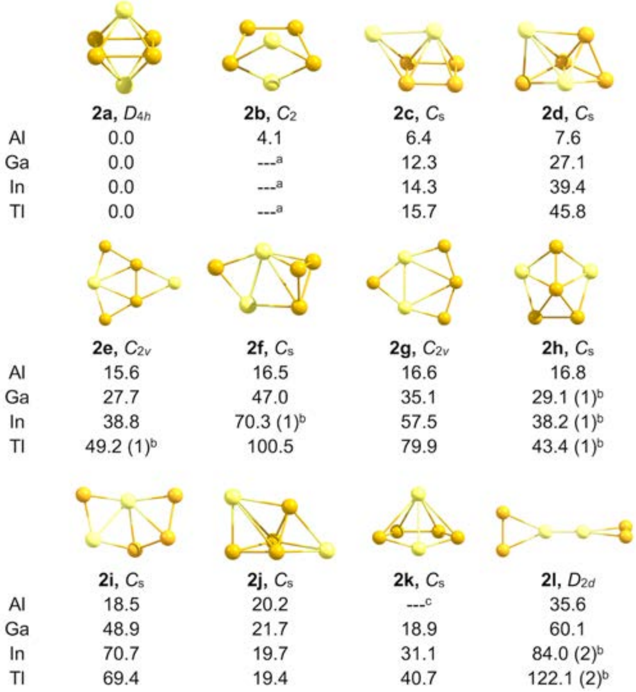

	2a, D_{4h}	2b, C_2	2c, C_s	2d, C_s	2e, C_{2v}	2f, C_s	2g, C_{2v}	2h, C_s	2i, C_s	2j, C_s	2k, C_s	2l, D_{2d}
Al	0.0	4.1	6.4	7.6	15.6	16.5	16.6	16.8	18.5	20.2	---[c]	35.6
Ga	0.0	---[a]	12.3	27.1	27.7	47.0	35.1	29.1 (1)[b]	48.9	21.7	18.9	60.1
In	0.0	---[a]	14.3	39.4	38.8	70.3 (1)[b]	57.5	38.2 (1)[b]	70.7	19.7	31.1	84.0 (2)[b]
Tl	0.0	---[a]	15.7	45.8	49.2 (1)[b]	100.5	79.9	43.4 (1)[b]	69.4	19.4	40.7	122.1 (2)[b]

Figure 7.4. Lowest-lying structures of the E_2P_4 (E= Al-Tl) clusters computed at the S12h/TZ2P level. Relative energies are given in kcal·mol^{-1}. [a]This structure does not converge. [b]In parentheses are the number of imaginary frequencies. [c]This structure converges to the **2b** isomer.

cations does not alter drastically the electronic structure of the P_4 ring. Moreover, the P-P bond lengths are in excellent agreement with those obtained experimentally for the $Cs_2P_4{\cdot}2NH_3$ compound (2.146 and 2.148 Å). The structural diversity is still present for the Al_2P_4 cluster, since we located ten local minima within the range of 20 kcal·mol^{-1}. Notice that the second most stable form of Al_2P_4 (**2b**) is only 4.1 kcal·mol^{-1} less stable than **2a** and is a C_2 bicyclic entity, similar to the structure found by Ding and co-workers[224] for $Al_2C_4H_4$. A D_{4h} bond-stretch isomer with a P-P bond length of 2.417 Å was also found at 40.3 kcal·mol^{-1}. A similar situation for the Be_3^{2-} dianion was recently discussed.[251,252] Finally, the most stable triplet is less stable by 46.9 kcal·mol^{-1}.

For Ga, In, and Tl clusters only four local minima were found in the range of 20 kcal·mol^{-1} (**2a**, **2c**, **2j**, and **2k** structures in Figure 7.4). The second most stable isomer keeps a square P_4 moiety, but with the E atoms on the same side of the P_4 plane (**2c**). The relative energy between **2c** and the global minimum increases down Group 13 from 6.4 (E= Al) to 15.7 kcal·mol^{-1} (E= Tl). In **2k**, an E atom is inserted into the P_4^{2-} fragment in order to form an almost flat pentagon, which interacts with the other E atom by means of its π system. Finally **2j**, which is less stable than **2a** by approximately 20 kcal·mol^{-1}, contains a P_4 butterfly rhombus. Note that the D_{2d} arrangement (the most stable for E= B) is only a non-competitive local minima for Al and Ga and a stationary point of order two for In and Tl. The most stable triplet forms are less stable than **3a** by 67.8 (Ga), 70.3 (In), and 70.5 kcal·mol^{-1} (Tl).

P_4, called white phosphorus, exists as tetrahedral molecule and is one of the allotropes of phosphorus. Let us consider the formation of the title complexes by means of the hypothetical reaction $\mathrm{E_2} + \mathrm{P_4}(T_d) \rightarrow \mathrm{E_2P_4}$. While B_2 is a triplet, the rest of the diatomic E_2 (E= Al-Tl) molecules are singlets. The energies for the reaction $\mathrm{E_2} + \mathrm{P_4} \rightarrow \mathrm{E_2P_4}$ obtained at the S12h/TZ2P level (including the ZPE correction) are -159.6 (B), -72.7 (Al), -68.3 (Ga), -58.5 (In), and -54.5 kcal·mol^{-1} (Tl). So, clearly, the formation of the title complexes by means of the suggested reaction is thermodynamically favorable.

7.3.2 Adaptive natural density partitioning analysis

According to the AdNDP analysis (see Figure 7.5), in all the D_{4h} E_2P_4 clusters (E= Al-Tl), the bonding framework consists of four (2c-2e) P-P bonds with the occupation number of 1.99|e| (except for the boron cluster, in which the occupation number is 1.88|e|) and three delocalized (6c-2e) π bonds, closely resembling benzene π MOs. Additionally, six lone pairs, four of them located on the P atoms and the other two on the E atoms, indicate that the E atoms can act as donor Lewis bases. Only small differences on the occupation number is noted between the boron and the rest of the Group 13 clusters. One would expect that the D_{4h} form of E_2P_4, even for boron, should be one of the most stable structures. Aromaticity of the planar P_4^{2-} fragment is a strong argument in favor of this assumption. However, aromaticity, in some cases, is not enough to preserve the symmetry of a molecule. The question that still remains is why boron prefers a different structure than the inverse sandwiches, even though for the inverse sandwich structures the strongest interaction energy is obtained in fact for boron (see Table 7.1).

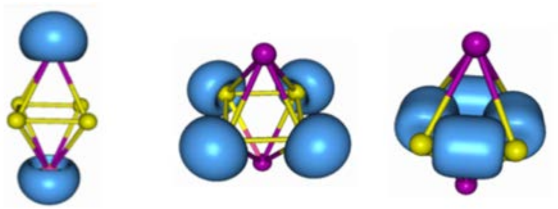

Two lone pairs on E atoms
[B] ON = 1.95 |e|
[Al] ON = 1.96 |e|
[Ga] ON = 1.97 |e|
[In] ON = 1.97 |e|
[Tl] ON = 1.96 |e|

Four lone pairs on P atoms
[B] ON = 1.93 |e|
[Al] ON = 1.95 |e|
[Ga] ON = 1.96 |e|
[In] ON = 1.96 |e|
[Tl] ON = 1.96 |e|

Four 2c-2e P-P σ bonds
[B] ON = 1.88 |e|
[Al] ON = 1.98 |e|
[Ga] ON = 1.99 |e|
[In] ON = 1.98 |e|
[Tl] ON = 1.99 |e|

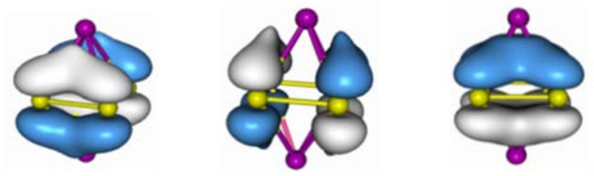

Three 6c-2e E_2P_4 π bonds
[B] ON = 1.99 |e|
[Al] ON = 2.00 |e|
[Ga] ON = 2.00 |e|
[In] ON = 1.99 |e|
[Tl] ON = 1.99 |e|

Figure 7.5. Chemical bonding pictures of E_2P_4 (E= B, Al, Ga, In and Tl) revealed by the AdNDP analysis. The AdNDP analysis was performed at PBE0/LANL2DZ level.

7.3.3 Energy decomposition analysis

Let us first focus our attention on the bonding in the inverse sandwiches. The orbital correlation diagram between the $(E\cdots E)^{2+}$ fragment valence orbitals and the π orbitals of the P_4^{2-} moiety in the neutral [E-P_4-E] (E= B, Al, Ga, In, Tl) species is qualitatively the same as that of the $[E\text{-}Cp\text{-}E]^+$ cations (see Figure 7.6). Four of the eight π valence electrons of the inverse sandwiches occupy the lowest-lying degenerate e_{1g} orbitals, which are the result of the combination of the corresponding e_{1g} orbitals of the P_4^{2-} fragment and the empty p_x and p_y atomic orbitals of the $(E\cdots E)^{2+}$ fragment. The other four valence π electrons occupy two a_{2u} orbitals, which are formed by combination of the a_{2u} orbital of P_4^{2-} and the antisymmetric combination of the s atomic orbital of the $(E\cdots E)^{2+}$ fragment.

The energy decomposition analysis (EDA) reveals that the boron cluster has the highest interaction energy (ΔE_{int}= -651.9 kcal·mol^{-1}) and this value decreases

Table 7.1. Results of the EDA for the **2a** (D_{4h}) structure in [E-P_4-E] (E= B-Tl) complexes. The interacting fragments are $(E\cdots E)^{2+}$ and P_4^{2-}. Energy values are in kcal ·mol^{-1}.

	$(E\cdots E)^{2+} + P_4^{2-} \rightarrow E_2P_4$				
	B	**Al**	**Ga**	**In**	**Tl**
ΔE_{int}	-651.9	-503.9	-493.9	-459.9	-442.0
ΔE_{Pauli}	422.6	236.9	220.4	190.4	159.9
$\Delta E_{\text{elstat}}{}^{a}$	-599.8 (56%)	-538.6 (73%)	-530.3 (74%)	-508.7 (78%)	-484.8 (81%)
$\Delta E_{\text{oi}}{}^{a}$	-474.8 (44%)	-202.3 (27%)	-184.1 (26%)	-141.5 (22%)	-116.7 (19%)
$a_{1g}{}^{b}$	-63.0 (13%)	-25.0 (12%)	-21.0 (11%)	-15.9 (11%)	-11.8 (10%)
$a_{2g}{}^{b}$	0.0 (0%)	0.0 (0%)	0.0 (0%)	0.0 (0%)	0.0 (0%)
$b_{1g}{}^{b}$	-7.5 (2%)	-4.9 (2%)	-4.2 (2%)	-3.4 (2%)	-3.0 (3%)
$b_{2g}{}^{b}$	-5.7 (1%)	-3.2 (2%)	-2.9 (2%)	-2.2 (2%)	-1.8 (2%)
$e_{1g}{}^{b}$	-182.4 (39%)	-65.0 (32%)	-63.6 (34%)	-45.6 (32%)	-40.7 (35%)
$a_{1u}{}^{b}$	0.0 (0%)	0.0 (0%)	0.0 (0%)	0.0 (0%)	0.0 (0%)
$a_{2u}{}^{b}$	-157.9 (33%)	-81.0 (40%)	-71.4 (39%)	-57.9 (41%)	-44.7 (38%)
$b_{1u}{}^{b}$	0.0 (0%)	0.0 (0%)	-0.1 (0%)	-0.1 (0%)	-0.2 (0%)
$b_{2u}{}^{b}$	0.0 (0%)	0.0 (0%)	-0.2 (0%)	-0.2 (0%)	-0.4 (0%)
$e_{1u}{}^{b}$	-58.3 (12%)	-23.2 (12%)	-20.7 (12%)	-16.1 (12%)	-14.1 (12%)
ΔE_{disp}	0.1	0.1	0.1	-0.1	-0.3
ΔE_{prep}	92.3	69.6	69.7	63.2	61.5
ΔE_{deform}	*0.1*	*0.1*	*0.1*	*0.2*	*0.1*
$\Delta E_{\text{E-E}}$	*92.2*	*69.6*	*69.6*	*63.0*	*61.4*
ΔE_{Bond}	-559.6	-434.3	-424.3	-396.7	-380.5

^{a}The percentaje values in parentheses give the contribution to the total attractive interactions $\Delta E_{\text{elstat}} + \Delta E_{\text{oi}}$. ^{b}The percentage values in parentheses give the contribution to the total interactions ΔE_{oi}. $^{c}\Delta E_{\text{prep}}$ gives the contribution to the total interactions ΔE_{prep} + $\Delta E_{\text{E-E}}$.

monotonically when one goes from boron to thallium (see Table 7.1). Interestingly, the orbital and electrostatic interactions in the boron cluster are much higher than those computed for the heavier analogues. The electrostatic bonding is the main contribution to the total attraction for all cases (56% in [B-P_4-B] to 81% in [Tl-P_4-Tl]). The partition of the orbital term into contributions from irreducible representations shows that the σ bonding (a_{1g} + a_{2u}) is slightly stronger than the π bonding (e_{1g}). The preparation energy term is entirely dominated by the electrostatic repulsion between the two E^+ cations. Note that the dispersion term is negligible.

The boron cluster has the highest interaction energy among the inverse sandwich structures, but it does not guarantee that this isomer is the global minimum (or even a local minimum, given that the boron cluster **1j** is in fact a transition state, *vide supra*). This is because there is a strong competition between several stabilization factors; all isomers suffer several electronic modifications when the Group 13 element E is changed. In the heavier congeners, the results of the bond dissociation energies (ΔE_{Bond}) suggest that the stability of the [E-P_4-E] (E= Al-Tl) complexes with respect to loss both $(E\cdots E)^{2+}$ atoms is Al > Ga > In > Tl. However, the traditional EDA does not give us a satisfactorily

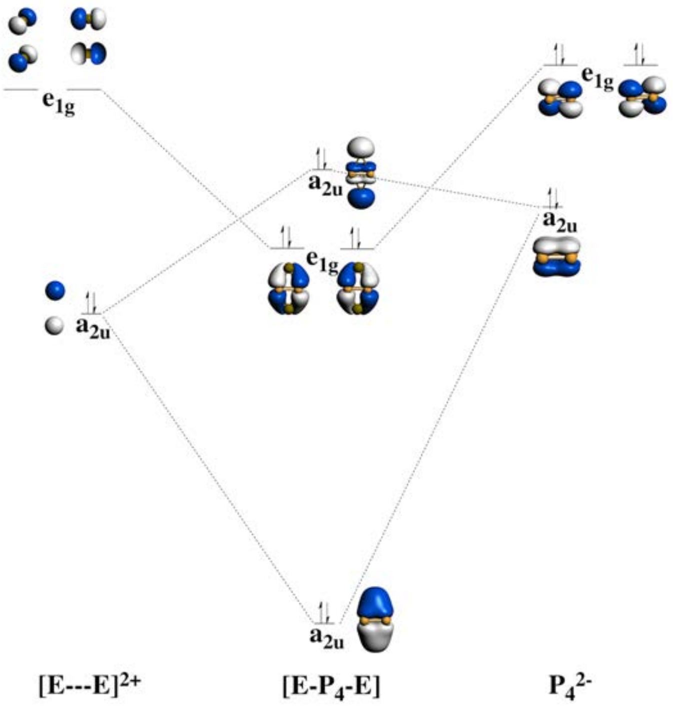

Figure 7.6. Qualitative correlation diagram for the D_{4h} [E-P$_4$-E] (E= B-Tl) complexes.

understanding of the relative stability between the D_{4h} B_2P_4 and E_2P_4 (E= Al-Tl) complexes, nor does it provide much insight into the isomeric preference of the species.

7.3.4 Isomerization energy decomposition analysis

To gain more quantitative insight into the nature of the P-E interactions, and how these interactions contribute to the stabilization of one specific isomer, we chose the hypothetical dissociation reaction $E_2P_4 \rightarrow E_2^{2+} + P_4^{2-}$ in order to compute the isomerization energy decomposition analysis (IEDA).[235] This analysis yields insight into the origins of the isomeric preferences in a quantitative way. The isomerization energy can be divided into two terms: the distortion energy (ΔE_{dist}) and the interaction energy difference ($\Delta\Delta E_{\mathrm{int}}$) [Eq. (7.1)].

$$\Delta E_{iso} = \Delta E_{dist} + \Delta\Delta E_{int} \tag{7.1}$$

The horizontal reactions of Figure 7.7 are related to the bonding between the E_2^{2+}-dimer fragment with the isolated P_4^{2-} fragment to form the D_{4h} and D_{2d} isomers, whereas vertical reactions involve the fragment distortions. In other words, to find the preferred geometry, the quantitative relationship between distortion and interaction energies in the IEDA must be analyzed. The changes in energy associated to each transformation have been summarized in Figure 7.8 and Table 7.2. In all cases, the interaction energy is stronger in the D_{2d} form ($\Delta E_{\text{int(2)}}$) than in the D_{4h} form ($\Delta E_{\text{int(1)}}$); at the same time the difference between these two decreases drastically from boron ($\Delta\Delta E_{\text{int}}$= -410.5 kcal ·mol^{-1}) to thallium ($\Delta\Delta E_{\text{int}}$ = -138.3 kcal ·mol^{-1}).

In each E_2P_4 cluster, the energy required to distort the fragments from the perfect inverse sandwich to the $D_{2\text{d}}$ form is positive (from 195 to 298 kcal ·mol^{-1}). For the boron cluster the interaction difference of -410.5 kcal ·mol^{-1} is clearly stronger than the distortion value of +298.3 kcal ·mol^{-1}. Here is worth mentioning that the reduction of the $\Delta\Delta E_{\text{int}}$ term down Group 13 is a consequence of the orbital contribution diminution and a significant increase of the Pauli repulsion, both into the D_{2d} isomers. The origin of the preference for the D_{2d} isomer over the D_{4h} isomer for B_2P_4 is the very strong interaction energy between the B_2^{2+} and P_4^{2-} fragments in the D_{2d} form (vide supra). In the rest of the clusters, this interaction energy is quite reduced and not sufficient to overcome the cost related to the geometrical changes from the inverse sandwich to the D_{2d} form (more than 256 kcal ·mol^{-1});

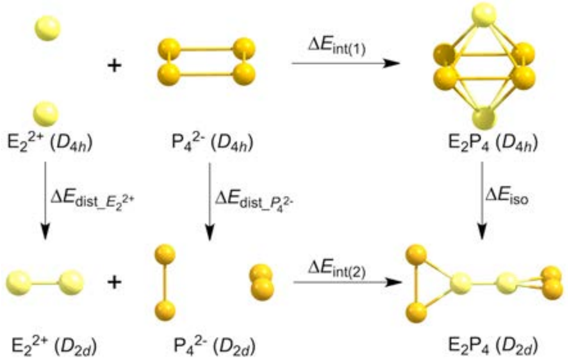

Figure 7.7. Energetic reaction cycle involving the isomerization of the E_2P_4 clusters (E= B-Tl) between D_{4h} and D_{2d} structures.

so for E= Al, Ga, In, or Tl, the cluster prefers to preserve the D_{4h} structure.

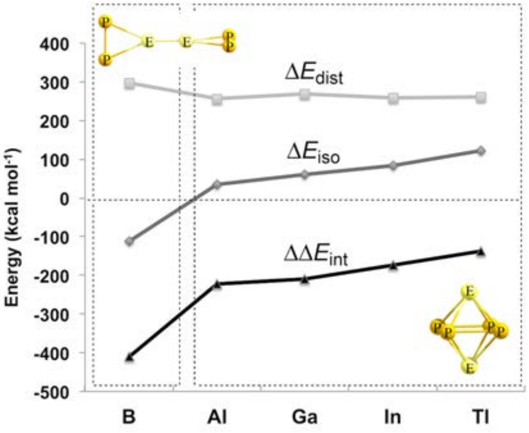

Figure 7.8. Contributions to the isomerization energy for the E_2P_4 clusters (E= B-Tl) by using IEDA.

Table 7.2. Results of IEDA at the S12h/TZ2P level for the E_2P_4 (E = B, Al, Ga, In, Tl) clusters with E_2^{2+} and P_4^{2-} fragments for the $D_{4h} \rightarrow D_{2d}$ isomerization reaction. Energy values are in kcal·mol⁻¹.

	$\Delta E_{int(1)}$	$\Delta E_{int(2)}$	ΔE_{dist_E2+2}	ΔE_{dist_P4-2}	$\Delta\Delta E_{Pauli}$	$\Delta\Delta V_{elstat}$	$\Delta\Delta E_{oi}$	$\Delta\Delta E_{disp}$	ΔE_{dist}	$\Delta\Delta E_{int}$	ΔE_{iso}
B	-651.9	-1062.3	93.8	204.5	-8.1	-9.2	-392.5	-0.7	298.3	-410.5	-112.2
Al	-503.9	-725.2	57.6	199.1	4.8	16.7	-241.5	-1.2	256.7	-221.2	35.5
Ga	-493.9	-702.8	70.2	199.2	65.0	-21.5	-251.6	-1.3	269.4	-209.4	60.5
In	-459.9	-632.7	61.2	196.3	69.3	-23.7	-216.8	-1.0	257.5	-172.2	84.7
Tl	-442.0	-580.4	66.0	195.4	125.0	-53.9	-208.8	-0.8	261.4	-138.6	123.1

7.3.5 Global and local aromaticity

In Table 7.3, the I_{NB} values for the whole molecule (global aromaticity) and the local aromaticity of the P_4^{2-} unit for the D_{4h} and D_{2d} isomers are collected together with the delocalization indices between P_4^{2-} and E_2^{2+} fragments for the D_{2d} conformer. The global aromaticity values cannot explain the relative stability among the different conformers: the numbers do not differ too much when moving along the group (with the exception of D_{4h} Al_2P_4); in addition, systematically D_{4h} conformers show positive numbers, whereas D_{2d}

Table 7.3. The second, third and fifth columns collect the results of I_{NB} aromaticity index (values multiplied by 1000) for the E_2P_4 (E= Al, Ga, In, Tl) *D_{4h}* and *D_{2d}* clusters. Global values (E_2P_4) and the local values for the P_4^{2-} unit (for comparison the free P_4^{2-} value is 53) for the *D_{4h}* conformer are collected. The fourth column contains the delocalization index between P_4^{2-} unit and the E_2^{2+} fragment.

	D_{4h}		D_{2d}	
	P_4^{2-}	E_2P_4	E_2^{2+}… P_4^{2-}	E_2P_4[a]
B	34	33	5.6	-25
Al	44	30	3.5	-18
Ga	41	32	4.8	-24
In	42	32	4.9	-24
Tl	42	32	5.1	-25

[a] Negative I_{NB} values are obtained by taking the sign under the sixth square root in the expression (see reference [238].

clusters show negative (and smaller in magnitude) values. However, inspection of the local aromaticity among *D_{4h}* conformers reveals that the P_4^{2-} ring in B_2P_4 is much less aromatic than the other *D_{4h}* clusters. In spite that there is not a clear relation between aromaticity and stability, the aromaticity of the phosphorus unit in *D_{4h}* shows that B_2P_4 has the least aromatic P_4^{2-} ring among *D_{4h}* conformers, supporting the boron preference for the *D_{2d}* conformer. On the other hand, the analysis of the interaction between P_4^{2-} and E_2^{2+} fragments by means of electron delocalization indices puts forward the stronger interaction between these moieties in the *D_{2d}* conformer, in agreement with the IEDA analysis. Finally, it is interesting to note that going from the P_4^{2-} unit to the D_{4h} E_2P_4 complex, the aromaticity decreases. Donation from the π orbitals of P_4^{2-} into the orbitals of same symmetry of the E_2^{2+} fragment leads to a significant reduction in the aromaticity of the 6π P_4^{2-} ring. The situation is similar to that of the benzene when it is coordinated to transition metals.[253]

7.3.6 ^{31}P-NMR shielding constants

In the same manner, we predicted the ^{31}P-NMR shielding constants for the *D_{4h}* and *D_{2d}* isomers at the KT2/ET-pVQZ level. As shown in Table 7.4, here exists a systematic change in both *D_{4h}* and *D_{2d}* isomers. Among the *D_{4h}* conformers, the ^{31}P-NMR shielding values increase (are less negative) as the cations contain more electrons. Here, it is interesting to note that the *D_{4h}* B_2P_4 complex has the most deshielded value (-629.6 ppm),

Table 7.4. ^{31}P-NMR shielding values (ppm) computed at the KT2/ET-pVQZ level for the D_{4h} and D_{2d} isomers of the E_2P_4 clusters.

	D_{4h}	D_{2d}
B	-629.6	-385.6
Al	-161.6	-857.8
Ga	-134.1	-863.8
In	-69.4	-1060.6
Tl	-45.4	-1269.3

supporting the aromaticity study that shows that the B_2P_4 has the least aromatic P_4^{2-} ring. In contrast, the D_{2d} isomers follow the opposite trend and the ^{31}P shielding values decrease from boron to thallium. Therefore, the ^{31}P-NMR shielding constants are sensitive to changes in the modifying cations and these results can be useful in future experimental studies to identify the presence of these clusters and their geometrical structure.

In this chapter, we have computationally explored the possibility of formation of inverse carbon-free sandwiches for clusters of type E_2P_4, with Group 13 elements B-Tl. This proposition is based on consideration of the aromaticity of the square-planar P_4^{2-} unit, which should favor the formation of the cluster with a proper choice of the E^+ cations. Our studies, including an energy decomposition analysis, indicate that the interaction energy between the E_2^{2+} and P_4^{2-} fragments is largest for E= B, and substantially reduced for E= Al-Tl. Nevertheless, the boron cluster is the only one for which the D_{4h} symmetric inverse sandwich is not the most favored isomer. Instead, it prefers to form a D_{2d}-symmetric structure of two perpendicular BP_2 units, which includes a multiple B-B bond. For the other elements (Al-Tl), the inverse sandwich isomer is indeed the most favored one, and becomes even more so when decreasing down the periodic table.

The peculiar behavior of boron cluster was understood by performing an isomerization energy decomposition analysis, which showed that the preference for the perpendicular D_{2d} isomer results directly from the interaction energy. For the boron cluster, the change in interaction energy when going from the D_{4h} to the D_{2d} isomer is more than sufficient to overcome the energetic cost that this change in geometry brings with it; for the other elements, the increase in interaction energy is insufficient and hence the D_{4h} isomer remains preferred. Moreover, the aromaticity analysis of these species and the delocalization between the fragments corroborate these trends. Additionally, the ^{31}P-NMR shielding constants have been predicted for the E_2P_4 cluster, in both D_{4h} and D_{2d} conformations, in order to support future experimental analysis.

Chapter 8

General Conclusions

Even though NMR spectroscopy is already extremely useful as analytical tool, it can benefit substantially from quantum-chemical calculations. The theoretical analysis of NMR properties, and in particular the calculation of chemical shift constants, can help to predict, confirm or establish the observed signals and provide a basis for spectral assignments and structure elucidation.

As this thesis has attempted to illustrate, a direct correlation between experimental and computed NMR data may be achieve if the modeling of the electronic structure is accurately described. However, the quality of the computed NMR chemical shifts depends on several factors and no simple protocol can be established for such studies. Several methodological issues such as the level of theory, basis set, effects of the environment, choice of the reference molecule, and relativistic effects are of crucial importance and the main factors that influence the quality of calculated data.

The challenging systems proposed in this thesis allowed us to gain a better understanding by accurately taking into consideration different strategies and procedures for the calculation of the NMR chemical shifts. Thus, depending on the target compounds, the main conclusions can be divided in four sections:

1) The first study of supramolecular complexes based on A-T and A-U base pairs showed us how the prediction of ^{13}C-NMR shielding constants can be very useful for examining the influence of substituents and chemical environment on NMR shielding constants. Experimental evidence that support the idea of a correlation between the Watson-Crick hydrogen-bond strength and the NMR shielding of *C*2-adenine has been refuted, proving that such an approach may yield the right

answer for the wrong reason.

2) From the second study of *trans*-platinum(II) complexes, where there are strong interactions between the solvent and the platinum complex, the use of *ab-initio* dynamic simulations is fundamental for the calculation of ^{31}P-NMR chemical shifts. Moreover, as the complexes contain heavy elements, a relativistic treatment was required and both scalar and spin-orbit relativistic effects need to be considered. In this case, the currently offered standard quantum chemical methods are not sufficient and a much higher accuracy of the computations is required.

3) Regarding the Host-Guest Hemicarcerands studied in Chapter 6, the ^{1}H-NMR chemical shifts calculations provided a direct correlation between theoretical and experimental measurements. Particularly for these large systems, DFT approaches are probably the only means available to obtain reasonably accurate results.

4) The novel E_2P_4 clusters (E= Group 13 elements), with a stable D_{4h} symmetric inverse-sandwich structure, have been proposed as a promising new target in main-group chemistry. The preference for the D_{2d} isomer for B_2P_4 and D_{4h} for the heavier analogues has been rationalized in terms of an isomerization- energy decomposition analysis and determination of aromaticity. As an additional tool for structural elucidation of these novel clusters, the ^{31}P-NMR shielding constants were predicted for the most stable structures.

As shown in this thesis, it seems that with some care the NMR chemical shifts can be accurately computed in most types of environment. However, some questions are still left to be answered concerning the scopes and limitations of the methodologies, in particular for practical applications where there should be some compromise between the cost and the quality.

References

---

(1) M. Lewitt, *Spin dynamics- Basics of nuclear magnetic resonance*, Wiley: Chichester, England, 2001.

(2) M. Bühl, T. van Mourik, *Wiley Interdisciplinary Reviews: Computational Molecular Science,* **2011**, *1*, 634.

(3) M. Kaupp, M. Bühl, V. G. Malkin, eds., *Calculation of NMR and EPR Parameters. Theory and Applications*, Weinheim: Wiley-VCH, 2004.

(4) A. A. Auer, J. Gauss, J. F. Stanton, *J. Chem. Phys.*, **2003**, *118*, 10407.

(5) M. J. Allen, T. W. Keal, D. J. Tozer, *Chem. Phys. Lett.*, **2003**, *380*, 70.

(6) T. W. Keal, D. J. Tozer, *J. Chem. Phys.*, **2003**, *119*, 3015.

(7) J. Poater, E. v. Lenthe, E. J. Baerends, *J. Chem. Phys.*, **2003**, *118*, 8584.

(8) M. Swart, C. Fonseca Guerra, F. M. Bickelhaupt, *J. Am. Chem. Soc.*, **2004**, *126*, 16718.

(9) G. Magyarfalvi, P. Pulay, *J. Chem. Phys.*, **2003**, *119*, 1350.

(10) Y. Zhao, D. G. Truhlar, *J. Phys. Chem. A,* **2008**, *112*, 6794.

(11) L. Armangué, M. Solà, M. Swart, *J. Phys. Chem. A,* **2011**, *115*, 1250.

(12) Y. Zhang, A. Wu, X. Xu, Y. Yan, *Chem. Phys. Lett.*, **2006**, *421*, 383.

(13) A. Wu, Y. Zhang, X. Xu, Y. Yan, *J. Comput. Chem.*, **2007**, *28*, 2431.

(14) D. J. Searles, H. Huber, *Molecular Dynamics and NMR Parameter Calculations*, M. Kaupp, M. Bühl, V. G. Malkin, eds. Calculation of NMR Parameters. Weinheim: Wiley-VCH, 2004, chapter 11, 175-189.

(15) T. A. Ruden, K. Ruud, *Ro-vibrational corrections to NMR parameters*, In: M. Kaupp, M. Bühl, V. G. Malkin, eds. Calculation of NMR parameters. Weinheim: Wiley-VCH, chapter 10, 1753-173, 2004.

(16) S. Grigoleit, M. Bühl, *Chem. Eur. J.*, **2004**, *10*, 5541.

(17) I. Ciofini, *Use of continuum solvent models in magnetic resonance parameter calculation*, In: M. Kaupp, M. Bühl, V. G. Malkin, eds. Calculation of NMR parameters. Weinheim: Wiley-VCH, chapter 12, 191-208, 2004.

(18) M. Jaszuński, K. V. Mikkelsen, A. Rizzo, M. Witanowski, *J. Phys. Chem. A,* **2000**, *104*, 1466.

(19) M. N. Manalo, A. C. de Dios, R. Cammi, *J. Phys. Chem. A,* **2000**, *104*, 9600.

(20) B. Mennucci, J. M. Martínez, J. Tomasi, *J. Phys. Chem. A,* **2001**, *105*, 7287.

(21) J. Kongsted, K. Ruud, *Chem. Phys. Lett.*, **2008**, *451*, 226.

(22) J. Autschbach In *Encyclopedia of Analytical Chemistry*; John Wiley & Sons, Ltd: 2006.

(23) J. Autschbach, S. Zheng, *Annu. Rep. NMR Spectrosc.*, **2009**, *67*, 1.

(24) E. van Lenthe, E. J. Baerends, J. G. Snijders, *J. Chem. Phys.*, **1993**, *99*, 4597.

(25) E. van Lenthe, J. G. Snijders, E. J. Baerends, *J. Chem. Phys.*, **1996**, *105*, 6505.

(26) S. K. Wolff, T. Ziegler, E. van Lenthe, E. J. Baerends, *J. Chem. Phys.*, **1999**, *110*, 7689.

(27) J. Autschbach, T. Ziegler, *Relativistic Computation of NMR Shieldings and Spin-Spin Coupling Constants*, In Encyclopedia of Nuclear Magnetic Resonance, Vol. 9, D. M. Grant, R. K. Harris, Eds., John Wiley & Sons: Chichester, U. K., 2002.

(28) M. Bühl, F. T. Mauschick, F. Terstegen, B. Wrackmeyer, *Angew. Chem. Int. Ed.*, **2002**, *41*, 2312.

(29) M. Buhl, F. T. Mauschick, *Phys. Chem. Chem. Phys.*, **2002**, *4*, 5508.

(30) M. Bühl, *J. Phys. Chem. A,* **2002**, *106*, 10505.

(31) M. Bühl, R. Schurhammer, P. Imhof, *J. Am. Chem. Soc.*, **2004**, *126*, 3310.

(32) M. Bühl, S. Grigoleit, H. Kabrede, F. T. Mauschick, *Chem. Eur. J.*, **2006**, *12*, 477.

(33) M. Sterzel, J. Autschbach, *Inorg. Chem.*, **2006**, *45*, 3316.

(34) M. Bühl, *Annu. Rep. NMR Spectrosc.*, **2008**, *64*, 77.

(35) J. Autschbach, *Calculation of heavy-nucleus chemical shifts: Relativistic all-electron methods*, In: M. Kaupp, M. Bühl, V. G. Malkin, eds. Calculation of NMR parameters. Weinheim: Wiley-VCH, chapter 14, 227-247, 2004.

(36) M. Bühl, *NMR of transition metal compounds*, In: M. Kaupp, M. Bühl, V. G. Malkin, eds. Calculation of NMR parameters. Weinheim: Wiley-VCH, 421-431, 2004.

(37) P. Hohenberg, W. Kohn, *Phys. Rev.*, **1964**, *136*, B864.

(38) A. Szabo, N. S. Ostlund, *Modern Quantum Chemistry*, MacMillian, New York, 1982.

(39) R. G. Parr, W. Yang, *Density Functional Theory of Atoms and Molecules*, Oxford University Press, New York, 1989.

(40) W. Koch, M. C. Holthausen, *A Chemist's Guide to Density Functional Theory*, Wiley-VCH, Weinheim, 2000.

(41) D. R. Hartree, *Math. Proc. Cambr. Phil. Soc.*, **2008**, *24*, 89.

(42) V. Fock, *Z. Phys.*, **1930**, *61*, 126.

(43) L. H. Thomas, *Math. Proc. Cambr. Phil. Soc.*, **2008**, *23*, 542.

(44) E. Fermi, *Rend. Accad. Lincei,* **1927**, *6*, 602.

(45) P. A. M. Dirac, *Math. Proc. Cambr. Phil. Soc.*, **2008**, *26*, 376.

(46) W. Kohn, L. J. Sham, *Phys. Rev.*, **1965**, *140*, A1133.

(47) J. C. Slater, *Phys. Rev.*, **1951**, *81*, 385.

(48) A. K. Rajagopal, K. Callaway, *Phys. Rev.*, **1973**, *B 7*, 1912.

(49) K. G. Dyall, K. Faegri, *Introduction to Relativistic Quantum Chemistry*, Oxford University Press, 2007.

(50) M. Reiher, A. Wolf, *Relativistic Quantum Chemistry*, Wiley, Weinheim, 2008.

(51) P. A. M. Dirac, *Proc. Roy. Soc. (London),* **1928**, *A 117*, 610.

(52) N. F. Ramsey, *Phys. Rev.*, **1950**, *78*, 695.

(53) V. G. Malkin, O. L. Malkina, L. A. Eriksson, D. R. Salahub, *Modern Density Functional Theory, Theoretical and Computational Chemistry*, J. M. Seminario, P. Politzer, eds., Elsevier Science: New York, Vol. 2, p. 273, 1995.

(54) G. Vignale, M. Rasolt, D. J. W. Geldart, *Adv. Quantum Chem.*, **1990**, *21*, 235.

(55) C. van Wüllen, *J. Chem. Phys.*, **1995**, *102*, 2806.

(56) A. M. Lee, N. C. Handy, S. M. Colwell, *The Journal of Chemical Physics,* **1995**, *103*, 10095.

(57) A. M. Lee, N. C. Handy, S. M. Colwell, *J. Chem. Phys.*, **1995**, *103*, 10095.

(58) T. Helgaker, M. Jaszuński, K. Ruud, *Chem. Rev.*, **1999**, *99*, 293.

(59) J. M. Haile, *Molecular Dynamics Simulations*, Wiley, 1991.

(60) M. P. Allan, D. J. Tildesley, *Computer Simulations of Liquids*, Clarendon Press, Oxford, 1987.

(61) F. Jensen, *Introduction to Computational Chemistry- 2nd ed.*, John Wiley & Sons Ltd, England, 2007.

(62) D. Frenkel, B. Smith, *Understanding Molecular Simulations, 2nd edition*, Academic Press, 2002.

(63) C. J. Cramer, D. G. Truhlar, *Solvent Effects and Chemical Reactivity*, O. Tapia, J. Beltran eds., Kluwer, Dordrecht, 1996.

(64) J. L. Rivail, D. Rinaldi, *Computational Chemistry, Review of Current Trends*, J. Leszczynki ed., World Scientific, New York, p. 139, 1995.

(65) C. J. Cramer, *Essentials of Computational Chemistry- Theories and Models*, John Wiley & Sons, Ltd, England,

2004.

(66) L. Piela, *Ideas of Quantum Chemistry*, Elsevier Science, 2006.

(67) A. R. Leach, *Molecular Modelling. Principles and Applications*, Longman, 1996.

(68) M. P. Allen, D. J. Tildesley, *Computer Simulations of Liquids*, Oxford Science Publications, Clarendon Press, Oxford, 1987.

(69) G. A. Jeffrey, W. Saenger, *Hydrogen Bonding in Biological Structures*, Springer-Verlag: Berlin, New York, Heidelberg, 1991.

(70) G. A. Jeffrey, *An Introduction to Hydrogen bonding*, Oxford University Press: New York, Oxford, Chapter 10, 1997.

(71) W. Saenger, *Principles of Nucleic Acid Structure*, Springer- Verlag: New York, Berlin, Heidelberg, Tokio, 1984.

(72) J. D. Watson, F. H. C. Crick, *Nature,* **1953**, *171*, 737.

(73) R. Franklin, R. G. Gosling, *Nature,* **1953**, *171*, 740.

(74) J. Poater, M. Swart, C. Fonseca Guerra, F. M. Bickelhaupt, *Comp. Theor. Chem.,* **2012**, *998*, 57.

(75) P. Acharya, P. Cheruku, S. Chatterjee, S. Acharya, J. Chattopadhyaya, *J. Am. Chem. Soc.,* **2004**, *126*, 2862.

(76) I. Vakonakis, A. C. LiWang, *J. Am. Chem. Soc.,* **2004**, *126*, 5688.

(77) Y.-I. Kim, M. N. Manalo, L. M. Peréz, A. LiWang, *J. Biomol. NMR,* **2006**, *34*, 229.

(78) R. Marek, V. Sklenar, *Annu. Rep. NMR Spectrosc.,* **2005**, *54*, 201.

(79) M. Dracinsky, R. Pohl, *Annu. Rep. NMR Spectrosc.,* **2014**, *82*, 59.

(80) J. Czernek, R. Fiala, V. Sklenar, *J. Magn. Reson.,* **2000**, *145*, 142.

(81) K. Malinakova, L. Novosadova, M. Lahtinen, E. Kolehmainen, J. Brus, R. Marek, *J. Phys. Chem. A,* **2010**, *114*, 1985.

(82) P. Vidossich, S. Piana, A. Miani, P. Carloni, *J. Am. Chem. Soc.,* **2006**, *128*, 7215.

(83) A. Pérez, J. Sponer, P. Jurecka, P. Hobza, F. J. Luque, M. Orozco, *Chem. Eur. J.,* **2005**, *11*, 5062.

(84) C. Fonseca Guerra, T. van der Wijst, F. M. Bickelhaupt, *Struct. Chem.,* **2005**, *16*, 211.

(85) C. Fonseca Guerra, T. van der Wijst, F. M. Bickelhaupt, *Chem. Eur. J.,* **2006**, *12*, 3032.

(86) C. Fonseca Guerra, T. van der Wijst, F. M. Bickelhaupt, *ChemPhysChem,* **2006**, *7*, 1971.

(87) G. te Velde, F. M. Bickelhaupt, E. J. Baerends, C. Fonseca Guerra, S. J. A. van Gisbergen, J. G. Snijders, T. Ziegler, *J. Comput. Chem.,* **2001**, *22*, 931.

(88) E. J. Baerends, *et. al*, SCM, Theoretical Chemistry, Vrije Universiteit, Amsterdam, The Netherlands, (see http://www.scm.com/ for more information).

(89) M. Swart, F. M. Bickelhaupt, *J. Comput. Chem.,* **2008**, *29*, 724.

(90) S. Grimme, J. Antony, S. Ehrlich, H. Krieg, *J. Chem. Phys.,* **2010**, *132*, 154104.

(91) S. Grimme, S. Ehrlich, L. Goerigk, *J. Comput. Chem.,* **2011**, *32*, 1456.

(92) C. Fonseca Guerra, T. van der Wijst, J. Poater, M. Swart, F. M. Bickelhaupt, *Theor. Chem. Acc.,* **2010**, *125*, 245.

(93) T. van der Wijst, C. Fonseca Guerra, M. Swart, F. M. Bickelhaupt, B. Lippert, *Angew. Chem. Int. Ed.,* **2009**, *48*, 3285.

(94) J. Poater, M. Swart, C. Fonseca Guerra, F. M. Bickelhaupt, *Chem. Commun.,* **2011**, *47*, 7326.

(95) R. Ditchfield, *Mol. Phys.,* **1974**, *27*, 789.

(96) E. Van Lenthe, E. J. Baerends, *J. Comput. Chem.,* **2003**, *24*, 1142.

(97) D. P. Chong, E. Van Lenthe, S. Van Gisbergen, E. J. Baerends, *J. Comput. Chem.,* **2004**, *25*, 1030.

(98) M. Swart, *Chem. Phys. Lett.,* **2013**, *580*, 166.

(99) P. R. T. Schipper, O. V. Gritsenko, S. J. A. van Gisbergen, E. J. Baerends, *J. Chem. Phys.*, **2000**, *112*, 1344.

(100) P. J. Stephens, F. J. Devlin, C. F. Chabalowski, M. J. Frisch, *J. Phys. Chem.*, **1994**, *45*, 11623.

(101) A. M. Teale, O. B. Lutnaes, T. Helgaker, D. J. Tozer, J. Gauss, *J. Chem. Phys.*, **2013**, *138*, 024111.

(102) A. Klamt, G. Schüürmann, *J. Chem. Soc., Perkin Trans. 2*, **1993**, 799.

(103) C. C. Pye, T. Ziegler, *Theor. Chem. Acc.*, **1999**, *101*, 396.

(104) M. Swart, E. Rösler, F. M. Bickelhaupt, *Eur. J. Inorg. Chem.*, **2007**, 3646.

(105) K. Morokuma, *Acc. Chem. Res.*, **1977**, *10*, 294.

(106) T. Ziegler, A. Rauk, *Theor. Chim. Acta*, **1977**, *46*, 1.

(107) F. M. Bickelhaupt, E. J. Baerends, *Kohn-Sham Density Functional Theory: Predicting and Understanding Chemistry*, Reviews in Computational Chemistry, Wiley-VCH: New York, Vol. 15, pp. 1-86, 2000.

(108) J. Šponer, P. Jurečka, P. Hobza, *J. Am. Chem. Soc.*, **2004**, *126*, 10142.

(109) C. Fonseca Guerra, F. M. Bickelhaupt, J. G. Snijders, E. J. Baerends, *J. Am. Chem. Soc.*, **2000**, *122*, 4117.

(110) C. Fonseca Guerra, F. M. Bickelhaupt, *Angew. Chem. Int. Ed.*, **1999**, *38*, 2942.

(111) P. Jurečka, P. Hobza, *J. Am. Chem. Soc.*, **2003**, *125*, 15608.

(112) P. Jurecka, J. Sponer, J. Cerny, P. Hobza, *Phys. Chem. Chem. Phys.*, **2006**, *8*, 1985.

(113) E. H. S. Anwander, M. M. Probst, B. M. Rode, *Biopolymers*, **1990**, *29*, 757.

(114) T. W. Hambley, *Coord. Chem. Rev.*, **1997**, *166*, 181.

(115) E. R. Jamieson, S. J. Lippard, *Chem. Rev.*, **1999**, *99*, 2467.

(116) J. Reedijk, *Chem. Commun.*, **1996**, 801.

(117) D. Lebwohl, R. Canetta, *European Journal of Cancer*, **1998**, *34*, 1522.

(118) P. J. O'Dwyer, J. P. Stevenson, *Clinical status of cisplatin, carboplatin, and other platinum-based antitumor drugs, Cisplatin: Chemistry and Biochemistry of a Leading Anticancer Drug*, 1999, pp. 29-69.

(119) R. B. Martin, *Cisplatin: Chemistry and Biochemistry of a Leading Anticancer Drug*, Lippert, B., Wiley-VCH, Zürich, 1999, p. 183.

(120) S. J. Berners-Price, T. A. Frenkiel, U. Frey, J. D. Ranford, P. J. Sadler, *J. Chem. Soc., Chem. Commun.*, **1992**, 789.

(121) L. Cubo, D. S. Thomas, J. Zhang, A. G. Quiroga, C. Navarro-Ranninger, S. J. Berners-Price, *Inorg. Chim. Acta*, **2009**, *362*, 1022.

(122) S. J. Berners-Price, L. Ronconi, P. J. Sadler, *Prog. Nucl. Magn. Reson. Spectrosc.*, **2006**, *49*, 65.

(123) A. G. Quiroga, *J. Inorg. Biochem.*, **2012**, *114*, 106.

(124) L. Cubo, A. G. Quiroga, J. Zhang, D. S. Thomas, A. Carnero, C. Navarro-Ranninger, S. J. Berners-Price, *Dalton Trans.*, **2009**, 3457.

(125) Francisco J. Ramos-Lima, Adoración G. Quiroga, José M. Pérez, M. Font-Bardía, X. Solans, C. Navarro-Ranninger, *Eur. J. Inorg. Chem.*, **2003**, *2003*, 1591.

(126) J. G. Verkade, L. D. Quin, *Methods in Stereochemical Analysis Volumes in the Series: Phosphorus 31 NMR Spectroscopy in Stereochemical Analysis*, VCH Publishers, Deerfield Beach, Florida, 1987.

(127) C. J. Jameson In *Encyclopedia of Analytical Chemistry*; John Wiley & Sons, Ltd: 2006.

(128) L. A. Truflandier, K. Sutter, J. Autschbach, *Inorg. Chem.*, **2011**, *50*, 1723.

(129) J. Autschbach, T. Ziegler, *J. Am. Chem. Soc.*, **2001**, *123*, 3341.

(130) J. Autschbach, T. Ziegler, *J. Am. Chem. Soc.*, **2001**, *123*, 5320.

(131) B. Le Guennic, K. Matsumoto, J. Autschbach, *Magn. Reson. Chem.*, **2004**, *42*, S99.

(132) J. P. Perdew, K. Burke, M. Ernzerhof, *Phys. Rev. Lett.*, **1996**, *77*, 3865.

(133) S. Grimme, *J. Comput. Chem.*, **2006**, *27*, 1787.

(134) A. Klamt, G. Schuurmann, *J. Chem. Soc., Perkin Trans. 2,* **1993**, 799.

(135) A. Klamt, *J. Phys. Chem.*, **1996**, *100*, 3349.

(136) C. C. Pye, T. Ziegler, *Theor. Chem. Acc.*, **1999**, *101*, 396.

(137) E. van Lenthe, A. Ehlers, E.-J. Baerends, *J. Chem. Phys.,* **1999**, *110*, 8943.

(138) E. van Lenthe, E. J. Baerends, J. G. Snijders, *J. Chem. Phys.*, **1994**, *101*, 9783.

(139) E. van Lenthe, R. van Leeuwen, E. J. Baerends, J. G. Snijders, *Int. J. Quantum Chem,* **1996**, *57*, 281.

(140) ReSpect, Relativistic Spectroscopy DFT program, Repisky M.; Komorovský, S.; Malkin, V. G.; Malkina, O. L. ; Kaupp, M.; Ruud, K., with contributions from Bast, R.; Ekström, U.; Kadek, M.; Knecht, S.; Konecny, L.; Malkin, E.; Malkin-Ondik, I. (see http://rel-qchem.sav.sk for more information/).

(141) A. M. Teale, O. B. Lutnæs, T. Helgaker, D. J. Tozer, J. Gauss, *J. Chem. Phys.*, **2013**, *138*, 024111.

(142) S. Reimann, U. Ekström, S. Stopkowicz, A. M. Teale, A. Borgoo, T. Helgaker, *Phys. Chem. Chem. Phys.*, **2015**, *17*, 18834.

(143) K. G. Dyall, *Theor. Chem. Acc.,* **1998**, *99*, 366.

(144) K. G. Dyall, *Theor. Chem. Acc.,* **2006**, *115*, 441.

(145) K. G. Dyall, *Theor. Chem. Acc.,* **2012**, *131*, 1.

(146) P. Lantto, K. Jackowski, W. Makulski, M. Olejniczak, M. Jaszuński, *J. Phys. Chem. A,* **2011**, *115*, 10617.

(147) C. J. Jameson, A. De Dios, A. Keith Jameson, *Chem. Phys. Lett.,* **1990**, *167*, 575.

(148) C. van Wullen, *Phys. Chem. Chem. Phys.*, **2000**, *2*, 2137.

(149) CP2K Developers Group, URL. http://www.cp2k.org/ (accessed Sep 2, 2016).

(150) J. Wang, R. M. Wolf, J. W. Caldwell, P. A. Kollman, D. A. Case, *J. Comput. Chem.,* **2004**, *25*, 1157.

(151) J. Wang, W. Wang, P. A. Kollman, D. A. Case, *J. Mol. Graphics Modell.,* **2006**, *25*, 247.

(152) W. L. Jorgensen, J. Chandrasekhar, J. D. Madura, R. W. Impey, M. L. Klein, *J. Chem. Phys.*, **1983**, *79*, 926.

(153) C. I. Bayly, P. Cieplak, W. Cornell, P. A. Kollman, *J. Phys. Chem.*, **1993**, *97*, 10269.

(154) A. K. Rappe, C. J. Casewit, K. S. Colwell, W. A. Goddard, W. M. Skiff, *J. Am. Chem. Soc.*, **1992**, *114*, 10024.

(155) N. Godbout, D. R. Salahub, J. Andzelm, E. Wimmer, *Can. J. Chem.*, **1992**, *70*, 560.

(156) S. Goedecker, M. Teter, J. Hutter, *Phys. Rev. B,* **1996**, *54*, 1703.

(157) L. A. Truflandier, J. Autschbach, *J. Am. Chem. Soc.,* **2010**, *132*, 3472.

(158) J. Autschbach, B. Le Guennic, *Chem. Eur. J.,* **2004**, *10*, 2581.

(159) E. R. Johnson, S. Keinan, P. Mori-Sánchez, J. Contreras-García, A. J. Cohen, W. Yang, *J. Am. Chem. Soc.*, **2010**, *132*, 6498.

(160) J. Contreras-García, E. R. Johnson, S. Keinan, R. Chaudret, J.-P. Piquemal, D. N. Beratan, W. Yang, *J. Chem. Theory Comput.,* **2011**, *7*, 625.

(161) F. J. Ramos-Lima, A. G. Quiroga, B. García-Serrelde, F. Blanco, A. Carnero, C. Navarro-Ranninger, *J. Med. Chem.,* **2007**, *50*, 2194.

(162) J. Vicha, J. Novotny, M. Straka, M. Repisky, K. Ruud, S. Komorovsky, R. Marek, *Phys. Chem. Chem. Phys.,* **2015**, *17*, 24944.

(163) P. Hrobárik, V. Hrobáriková, F. Meier, M. Repiský, S. Komorovský, M. Kaupp, *J. Phys. Chem. A,* **2011**, *115*, 5654.

(164) J. Vícha, R. Marek, M. Straka, *Inorg. Chem.,* **2016**, *55*, 1770.

(165) J. Autschbach, *Theor. Chem. Acc.,* **2004**, *112*, 52.

(166) E. C. Beret, R. R. Pappalardo, N. L. Doltsinis, D. Marx, E. Sánchez Marcos, *ChemPhysChem,* **2008**, *9*, 237.

(167) E. C. Beret, J. M. Martínez, R. R. Pappalardo, E. S. Marcos, N. L. Doltsinis, D. Marx, *J. Chem. Theory Comput.*, **2008**, *4*, 2108.

(168) D. J. Cram, S. Karbach, Y. H. Kim, L. Baczynskyj, G. W. Kallemeyn, *J. Am. Chem. Soc.*, **1985**, *107*, 2575.
(169) D. J. Cram, *Nature,* **1992**, *356*, 29.
(170) K. N. Houk, K. Nakamura, C. Sheu, A. E. Keating, *Science,* **1996**, *273*, 627.
(171) R. Warmuth, J. Yoon, *Acc. Chem. Res.*, **2001**, *34*, 95.
(172) J. Kang, J. Rebek, *Nature,* **1997**, *385*, 50.
(173) Y. Liu, R. Warmuth, *Org. Lett.*, **2007**, *9*, 2883.
(174) K. Nakamura, K. N. Houk, *J. Am. Chem. Soc.*, **1995**, *117*, 1853.
(175) F. Liu, R. C. Helgeson, K. N. Houk, *Acc. Chem. Res.*, **2014**, *47*, 2168.
(176) H. Wang, F. Liu, R. C. Helgeson, K. N. Houk, *Angew. Chem. Int. Ed.*, **2013**, *52*, 655.
(177) D. J. Cram, M. E. Tanner, C. B. Knobler, *J. Am. Chem. Soc.*, **1991**, *113*, 7717.
(178) M. L. C. Quan, D. J. Cram, *J. Am. Chem. Soc.*, **1991**, *113*, 2754.
(179) C. von dem Bussche-Hunnefeld, D. Buhring, C. B. Knobler, D. J. Cram, *J. Chem. Soc., Chem. Commun.*, **1995**, 1085.
(180) D. J. Cram, M. E. Tanner, R. Thomas, *Angew. Chem. Int. Ed. Engl.*, **1991**, *30*, 1024.
(181) C. N. Eid, C. B. Knobler, D. A. Gronbeck, D. J. Cram, *J. Am. Chem. Soc.*, **1994**, *116*, 8506.
(182) J. Kang, J. Rebek, *Nature,* **1996**, *382*, 239.
(183) D. D. Sternbach, D. M. Rossana, *J. Am. Chem. Soc.*, **1982**, *104*, 5853.
(184) N. K. Sangwan, H.-J. Schneider, *J. Chem. Soc., Perkin Trans. 2,* **1989**, 1223.
(185) E. L. Piatnitski, K. D. Deshayes, *Angew. Chem. Int. Ed.*, **1998**, *37*, 970.
(186) R. Warmuth, *Angew. Chem. Int. Ed. Engl.*, **1997**, *36*, 1347.
(187) H. Jiao, P. v. R. Schleyer, R. Warmuth, K. N. Houk, B. R. Beno, *Angew. Chem. Int. Ed. Engl.*, **1997**, *36*, 2761.
(188) T. Helgaker, O. B. Lutnaes, M. Jaszuński, *J. Chem. Theory Comput.*, **2007**, *3*, 86.
(189) L. s. Armangué, M. Solà, M. Swart, *J. Phys. Chem. A,* **2011**, *115*, 1250.
(190) S. Osuna, A. Rodriguez-Fortea, J. M. Poblet, M. Sola, M. Swart, *Chem. Commun.*, **2012**, *48*, 2486.
(191) C. Sheu, K. N. Houk, *J. Am. Chem. Soc.*, **1996**, *118*, 8056.
(192) R. Warmuth, J.-L. Kerdelhué, S. Sánchez Carrera, K. J. Langenwalter, N. Brown, *Angew. Chem. Int. Ed.*, **2002**, *41*, 96.
(193) X. Wang, Z. Yang, J. Wang, J. Zhang, W. Cao, *Journal of Molecular Structure: THEOCHEM,* **2006**, *766*, 169.
(194) B. R. Beno, C. Sheu, K. N. Houk, R. Warmuth, D. J. Cram, *Chem. Commun.*, **1998**, 301.
(195) R. C. Helgeson, K. Paek, C. B. Knobler, E. F. Maverick, D. J. Cram, *J. Am. Chem. Soc.*, **1996**, *118*, 5590.
(196) K. Nakamura, C. Sheu, A. E. Keating, K. N. Houk, J. C. Sherman, R. G. Chapman, W. L. Jorgensen, *J. Am. Chem. Soc.*, **1997**, *119*, 4321.
(197) M. J. Liddell, D. Margetic, A. S. Mitchell, R. N. Warrener, *J. Comput. Chem.*, **2004**, *25*, 542.
(198) T. A. Robbins, C. B. Knobler, D. R. Bellew, D. J. Cram, *J. Am. Chem. Soc.*, **1994**, *116*, 111.
(199) D. J. Cram, M. T. Blanda, K. Paek, C. B. Knobler, *J. Am. Chem. Soc.*, **1992**, *114*, 7765.
(200) E. v. Lenthe, E. J. Baerends, J. G. Snijders, *J. Chem. Phys.*, **1993**, *99*, 4597.
(201) E. van Lenthe, A. Ehlers, E.-J. Baerends, *J. Chem. Phys.*, **1999**, *110*, 8943.
(202) R. A. Kendall, T. H. D. Jr., R. J. Harrison, *J. Chem. Phys.*, **1992**, *96*, 6796.
(203) T. H. Dunning Jr, *J. Chem. Phys.*, **1989**, *90*, 1007.
(204) M. E. Harding, T. Metzroth, J. Gauss, *J. Chem. Theory Comput.*, **2008**, *4*, 64.
(205) CFOUR, J. F. Stanton, J. Gauss, M. E. Harding, P. G. Szalay, Austin, TX, USA; Mainz, Germany, 2010.
(206) A. Klamt, *J. Phys. Chem.*, **1996**, *100*, 3349.
(207) A. M. Orendt, J. C. Facelli, J. G. Radziszewski, W. J. Horton, D. M. Grant, J. Michl, *J. Am. Chem. Soc.*, **1996**,

118, 846.

(208) E. Kraka, D. Cremer, *Chem. Phys. Lett.*, **1993**, *216*, 333.

(209) P. Jutzi, N. Burford, *Chem. Rev.*, **1999**, *99*, 969.

(210) P. H. M. Budzelaar, J. J. Engelberts, J. H. van Lenthe, *Organomet.*, **2003**, *22*, 1562.

(211) P. Jutzi, G. Reumann, *J. Chem. Soc., Dalton Trans.*, **2000**, 2237.

(212) J. A. J. Pardoe, A. J. Downs, *Chem. Rev.*, **2007**, *107*, 2.

(213) C. L. B. Macdonald, A. H. Cowley, *J. Am. Chem. Soc.*, **1999**, *121*, 12113.

(214) O. T. Beachley, R. Blom, M. R. Churchill, K. Faegri, J. C. Fettinger, J. C. Pazik, L. Victoriano, *Organometallics*, **1989**, *8*, 346.

(215) J. Gauss, U. Schneider, R. Ahlrichs, C. Dohmeier, H. Schnoeckel, *J. Am. Chem. Soc.*, **1993**, *115*, 2402.

(216) A. Haaland, K.-G. Martinsen, S. A. Shlykov, H. V. Volden, C. Dohmeier, H. Schnoeckel, *Organomet.*, **1995**, *14*, 3116.

(217) A. Haaland, K.-G. Martinsen, H. V. Volden, W. Kaim, E. Waldhör, W. Uhl, U. Schütz, *Organomet.*, **1996**, *15*, 1146.

(218) Wei, M. Winter, R. A. Fischer, C. Yu, K. Wichmann, G. Frenking, *Chem. Commun.*, **2000**, 2495.

(219) B. Buchin, C. Gemel, T. Cadenbach, I. Fernández, G. Frenking, R. A. Fischer, *Angew. Chem.*, **2006**, *118*, 5331.

(220) R. A. Fischer, D. Weiß, M. Winter, I. Müller, H. D. Kaesz, N. Fröhlich, G. Frenking, *J. Organomet. Chem.*, **2004**, *689*, 4611.

(221) D. Weiss, T. Steinke, M. Winter, R. A. Fischer, N. Fröhlich, J. Uddin, G. Frenking, *Organomet.*, **2000**, *19*, 4583.

(222) D. Weiß, M. Winter, K. Merz, A. Knüfer, R. A. Fischer, N. Fröhlich, G. Frenking, *Polyhedron*, **2002**, *21*, 535.

(223) I. Fernández, E. Cerpa, G. Merino, G. Frenking, *Organomet.*, **2008**, *27*, 1106.

(224) N.-N. Liu, J. Xu, Y.-H. Ding, *Int. J. Quantum Chem*, **2013**, *113*, 1018.

(225) M. Baudler, K. Glinka, *Chem. Rev.*, **1993**, *93*, 1623.

(226) M. Baudler, K. Glinka, *Chem. Rev.*, **1994**, *94*, 1273.

(227) M. Baudler, *Angew. Chem. Int. Ed.*, **1987**, *26*, 419.

(228) G. Van Zandwijk, R. A. J. Janssen, H. M. Buck, *J. Am. Chem. Soc.*, **1990**, *112*, 4155.

(229) F. Kraus, J. C. Aschenbrenner, N. Korber, *Angew. Chem. Int. Ed.*, **2003**, *42*, 4030.

(230) Bilatu 1.0, J. Cabellos, F. Ortís-Chi, A. Ramírez, G. Merino, Cinvestav, Mérida, 2013.

(231) M. Saunders, *J. Comput. Chem.*, **2004**, *25*, 621.

(232) T. Ziegler, A. Rauk, E. Baerends, *Theor. Chim. Acta*, **1977**, *43*, 261.

(233) M. v. Hopffgarten, G. Frenking, *Wiley Interdisciplinary Reviews: Computational Molecular Science*, **2012**, *2*, 43.

(234) D. Y. Zubarev, A. I. Boldyrev, *Phys. Chem. Chem. Phys.*, **2008**, *10*, 5207.

(235) M. Contreras, E. Osorio, F. Ferraro, G. Puga, K. J. Donald, J. G. Harrison, G. Merino, W. Tiznado, *Chem. Eur. J.*, **2013**, *19*, 2305.

(236) C. Adamo, V. Barone, *J. Chem. Phys.*, **1999**, *110*, 6158.

(237) M. Swart, F. Matthias Bickelhaupt, *Int. J. Quantum Chem*, **2006**, *106*, 2536.

(238) J. Cioslowski, E. Matito, M. Solà, *J. Phys. Chem. A*, **2007**, *111*, 6521.

(239) E. Matito, M. Sola, P. Salvador, M. Duran, *Faraday Discuss.*, **2007**, *135*, 325.

(240) P. Salvador, E. Ramos-Cordoba, *J. Chem. Phys.*, **2013**, *139*, 071103.

(241) APOST-3D, P. Salvador, E. Ramos-Cordoba, Institute of Computational Chemistry and Catalysis,

University of Girona, Catalonia, Spain, 2011.

(242) I. Mayer, P. Salvador, *Chem. Phys. Lett.*, **2004**, *383*, 368.

(243) ESI-3D: Electron Sharing Indices Program for 3D Molecular Space Partitioning, E. Matito, Institute of Computational Chemistry and Catalisis, University of Girona, Catalonia, Spain, 2006.

(244) E. Matito, M. Duran, M. Solà, *J. Chem. Phys.*, **2004**, *122*, 014109.

(245) R. Ditchfield, *Mol. Phys.*, **1974**, *27*, 789.

(246) M. Zhou, N. Tsumori, Z. Li, K. Fan, L. Andrews, Q. Xu, *J. Am. Chem. Soc.*, **2002**, *124*, 12936.

(247) A. Moezzi, M. M. Olmstead, P. P. Power, *J. Am. Chem. Soc.*, **1992**, *114*, 2715.

(248) W. J. Grigsby, P. Power, *Chem. Eur. J.*, **1997**, *3*, 368.

(249) W. J. Grigsby, P. P. Power, *Chem. Commun.*, **1996**, 2235.

(250) H. Nöth, J. Knizek, W. Ponikwar, *Eur. J. Inorg. Chem.*, **1999**, *1999*, 1931.

(251) S. Giri, D. R. Roy, S. Duley, A. Chakraborty, R. Parthasarathi, M. Elango, R. Vijayaraj, V. Subramanian, R. Islas, G. Merino, P. K. Chattaraj, *J. Comput. Chem.*, **2010**, *31*, 1815.

(252) J. O. C. Jiménez-Halla, E. Matito, L. Blancafort, J. Robles, M. Solà, *J. Comput. Chem.*, **2009**, *30*, 2764.

(253) F. Feixas, J. O. C. Jiménez-Halla, E. Matito, J. Poter, M. Solà, *Pol. J. Chem.*, **2007**, *81*, 783.

Appendices

Appendix A1

Supporting material of Chapter 4, *"The influence of substituents and the environment on the NMR shielding constants of supramolecular complexes based on A-T and A-U base pairs"*

Table A1.1. VDD atomic charges in the front atoms and the adenine/thymine *C2* carbon atoms of the A^{X8}-T^{Y6} base pairs.

VDD atomic charges Q_A (a.u.)									
X8	Y6	N6	H6	O4	N1	H3	N3	C2-adenine	C2-thymine
H	H	-0.171	0.135	-0.291	-0.187	0.153	-0.121	0.092	0.208
NH_2	NH_2	-0.177	0.127	-0.308	-0.187	0.151	-0.131	0.083	0.208
OH	OH	-0.176	0.130	-0.302	-0.184	0.152	-0.127	0.087	0.209
NH^-	H	-0.184	0.116	-0.336	-0.080	0.147	-0.237	0.060	0.189
NH_2	H	-0.176	0.128	-0.291	-0.187	0.153	-0.121	0.084	0.207
NH_3^+	H	-0.158	0.150	-0.285	-0.171	0.153	-0.118	0.115	0.211
O^-	H	-0.184	0.118	-0.335	-0.083	0.147	-0.235	0.065	0.189
OH	H	-0.175	0.131	-0.290	-0.185	0.153	-0.121	0.088	0.207
OH_2^+	H	-0.157	0.151	-0.284	-0.169	0.153	-0.119	0.117	0.211
H	NH^-	-0.176	0.123	-0.366	-0.189	0.132	-0.137	0.090	0.194
H	NH_2	-0.172	0.133	-0.308	-0.188	0.150	-0.129	0.093	0.209
H	NH_3^+	-0.157	0.148	-0.284	-0.073	0.160	-0.223	0.110	0.205
H	O^-	-0.176	0.124	-0.358	-0.189	0.133	-0.136	0.090	0.192
H	OH	-0.172	0.133	-0.301	-0.188	0.152	-0.127	0.093	0.210
H	OH_2^+	-0.155	0.150	-0.268	-0.072	0.164	-0.222	0.109	0.210
F	H	-0.172	0.135	-0.289	-0.184	0.153	-0.122	0.092	0.208
Cl	H	-0.171	0.139	-0.288	-0.185	0.152	-0.121	0.096	0.211
Br	H	-0.171	0.138	-0.288	-0.185	0.150	-0.123	0.092	0.210
H	F	-0.171	0.134	-0.287	-0.188	0.155	-0.126	0.093	0.212
H	Cl	-0.170	0.135	-0.285	-0.187	0.154	-0.125	0.092	0.208
H	Br	-0.171	0.134	-0.284	-0.185	0.154	-0.124	0.090	0.208
F	F	-0.171	0.134	-0.285	-0.182	0.155	-0.125	0.091	0.212
Cl	Cl	-0.171	0.137	-0.283	-0.184	0.154	-0.126	0.093	0.210
Br	Br	-0.171	0.139	-0.283	-0.184	0.155	-0.122	0.096	0.210

Table A1.2. VDD atomic charges in the front atoms and the adenine/uracil *C*2 carbon atoms of the A^{X8}-U^{Y6} base pairs.

VDD atomic charges Q_A (a.u.)									
X8	Y6	N6	H6	O4	N1	H3	N3	C2-adenine	C2-uracil
H	H	-0.171	0.136	-0.297	-0.186	0.151	-0.122	0.091	0.213
NH_2	NH_2	-0.176	0.130	-0.315	-0.186	0.149	-0.128	0.082	0.210
OH	OH	-0.174	0.133	-0.305	-0.184	0.151	-0.125	0.089	0.213
NH^-	H	-0.185	0.117	-0.349	-0.078	0.147	-0.235	0.059	0.192
NH_2	H	-0.177	0.133	-0.297	-0.185	0.152	-0.120	0.085	0.212
NH_3^+	H	-0.157	0.150	-0.293	-0.169	0.154	-0.118	0.113	0.214
O^-	H	-0.184	0.120	-0.347	-0.081	0.148	-0.234	0.064	0.192
OH	H	-0.175	0.136	-0.298	-0.184	0.152	-0.119	0.090	0.212
OH_2^+	H	-0.156	0.151	-0.292	-0.166	0.154	-0.118	0.116	0.214
H	NH^-	-0.175	0.122	-0.377	-0.192	0.131	-0.136	0.092	0.197
H	NH_2	-0.171	0.133	-0.314	-0.188	0.148	-0.128	0.091	0.211
H	NH_3^+	-0.155	0.148	-0.289	-0.073	0.162	-0.220	0.107	0.207
H	O^-	-0.175	0.124	-0.370	-0.192	0.132	-0.135	0.093	0.196
H	OH	-0.171	0.135	-0.305	-0.187	0.151	-0.128	0.091	0.216
H	OH_2^+	-0.153	0.151	-0.274	-0.070	0.165	-0.218	0.108	0.213
F	H	-0.171	0.139	-0.296	-0.183	0.153	-0.119	0.095	0.212
Cl	H	-0.172	0.137	-0.296	-0.185	0.155	-0.121	0.092	0.214
Br	H	-0.171	0.136	-0.298	-0.187	0.153	-0.119	0.092	0.212
H	F	-0.171	0.137	-0.292	-0.185	0.152	-0.126	0.092	0.219
H	Cl	-0.171	0.137	-0.292	-0.186	0.152	-0.126	0.091	0.216
H	Br	-0.170	0.138	-0.292	-0.186	0.151	-0.125	0.091	0.216
F	F	-0.171	0.139	-0.291	-0.183	0.154	-0.123	0.094	0.217
Cl	Cl	-0.171	0.140	-0.291	-0.184	0.153	-0.122	0.095	0.214
Br	Br	-0.172	0.140	-0.292	-0.185	0.153	-0.123	0.094	0.216

Table A1.3. NMR C2-adenine shielding (σ) values (ppm) computed with SAOP/TZ2P level for the isolated adenine (AX8) bases and AX8-U base pairs.[a]

X8	Adenine (A^{X8})		A^{X8}-U		ΔΔ(σ)[c]	VDD charges[d]	
	C2 (σ)	Δσ	*C2* (σ)	Δσ		Q_A	ΔQ_A
H	29.39	0.00	30.77	0.00	0.00	0.091	0.000
NH^-	43.59	14.20	52.10[b]	21.33	7.13[b]	0.059	-0.032
NH_2	32.59	3.20	33.77	3.00	0.20	0.085	-0.006
NH_3^+	23.68	-5.71	24.82	-5.94	0.24	0.113	0.022
O^-	41.53	12.15	50.20[b]	19.43	7.28[b]	0.064	-0.027
OH	30.80	1.42	32.01	1.24	0.18	0.090	-0.001
OH_2^+	23.05	-6.34	24.25	-6.52	0.18	0.116	0.025
F	29.31	-0.07	30.49	-0.28	0.20	0.095	0.004
Cl	29.32	-0.07	30.57	-0.20	0.13	0.092	0.001
Br	29.67	0.28	30.91	0.15	0.00	0.092	0.001

[a] Geometries optimized at the BLYP-D3(BJ)/TZ2P level.

[b] Proton transfer occurs in the N1···H3-N3 hydrogen-bond from uracil to adenine.

[c] Absolute ΔΔ(σ) calculated as Δσ (A^{X8}-U) - Δσ (A^{X8}).

[d] VDD atomic charges Q_A (a.u.) in the *C2-adenine* atom of the A^{X8}-U base pairs.

Table A1.4. NMR *C2-adenine* shielding (σ) values (ppm) for the isolated adenine (A^{X8})[a] and the A^{X8}//A^{X8}-T[b] bases computed with SAOP/TZ2P level.

	Adenine (A^{X8})[a]		Adenine A^{X8}//A^{X8}-T[b]		
X8	*C2* (σ)	Δσ	*C2* (σ)	Δσ	ΔΔ(σ)[c]
H	29.39	0.00	29.70	0.00	0
NH^-	43.59	14.20	45.17	15.47	1.26
NH_2	32.59	3.20	32.82	3.11	0.09
NH_3^+	23.68	-5.71	24.04	-5.67	0.04
O^-	41.53	12.15	43.10	13.39	1.25
OH	30.80	1.42	31.09	1.39	0.03
OH_2^+	23.05	-6.34	23.48	-6.23	0.11
F	29.31	-0.07	29.61	-0.09	0.02
Cl	29.32	-0.07	29.60	-0.10	0.03
Br	29.67	0.28	29.94	0.23	0.05

[a] Geometries optimized at the BLYP-D3(BJ)/TZ2P level.
[b] A^{X8} bases at the A^{X8}-T geometry.
[c] Absolute ΔΔ(σ) calculated as Δσ (A^{X8}//A^{X8}-T) - Δσ (A^{X8}).

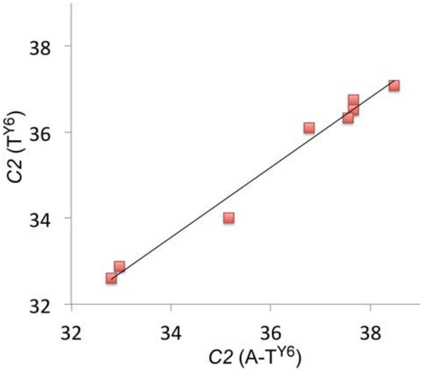

Figure A1.1. Calculated correlation between the *C2-thymine* shielding values (ppm) of isolated thymine (T^{Y6}) bases and A-T^{Y6} base pairs. The proton transfer systems were not included in the plot, due to its particular behavior.

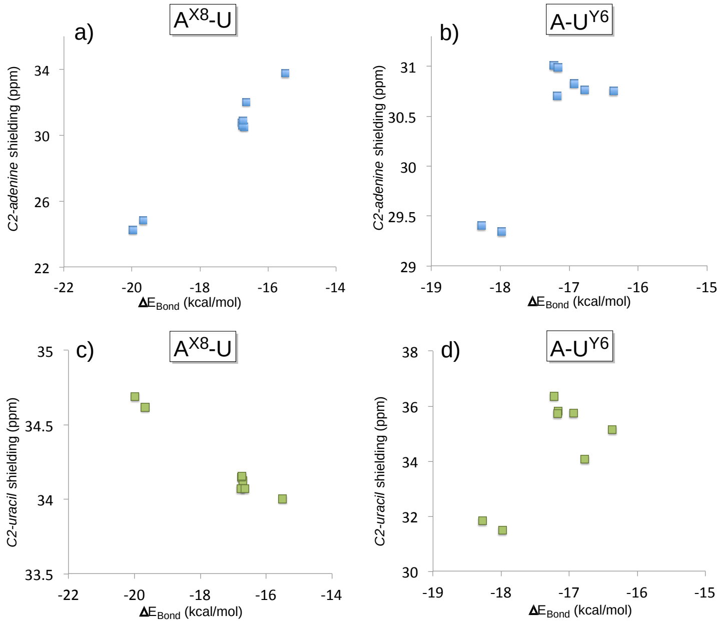

Figure A1.2. Calculated dependence of the NMR *C*2-shielding values (ppm) as a function of the hydrogen-bond strength (kcal·mol^{-1}). **a)** *C2-adenine* shielding of A^{X8}-U, **b)** *C2-adenine* shielding of A-U^{Y6}, **c)** *C2-uracil* shielding of A^{X8}-U, and **d)** *C2-uracil* shielding of A-U^{Y6} base pairs. The proton transfer systems were not included in the plot, due to its particular behavior.

Appendix A2

Supporting material of Chapter 5, *"Four-component relativistic ^{31}P-NMR calculations in trans-platinum(II) complexes: Importance of the solvent and dynamics in spectral simulations"*

Experimental section

At the ^{1}H NMR spectra of the complex (Figure A2.1a), the methyl group from the dma ligand coordinated to the platinum atom overlaps with the residual signal from the solvent used. This feature makes the detection of the speciation formed in solution more difficult and the solution studies require not only motorization by monodimentional NMR but also 2D-NMR experiments. In particular, the HSQC [^{1}H-^{13}C] NMR spectra (Figure A2.1b), allows the detection of the dma's cross peak near the residual DMSO signal and to discard residual solvent coordination.

Titration of the sample monitored by ^{1}H-NMR experiment to define the acuospecies is not possible as the pH of the solution itself is basic. However, the 2D-HSQC [^{1}H-^{13}C]

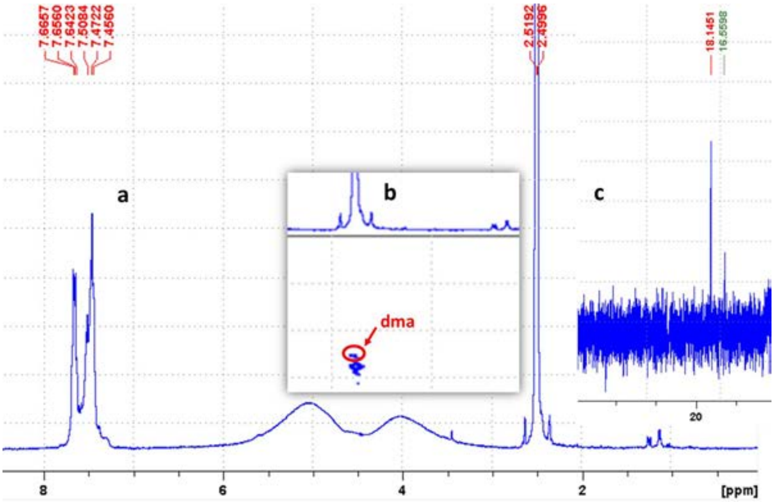

Figure A2.1 a) ^{1}H-NMR, b) HSQC [^{1}H-^{13}C] NMR and c) ^{31}P-NMR spectra of the complex in DMSO d_6 (200µl) and 300µl of D_2O/H_2O (90%/10%) after 30m.

NMR spectra discard DMSO coordination, as it show clearly no additional signals corresponding to DMSO coordination. However, we should be cautious and not discard any of those two possibilities, because the signals corresponding to these coordinating species may fall inside the water suppression area.

Table A2.1. Basis-set dependence of ZORA relativistic corrections (SR and SO) to the ^{31}P-NMR nuclear shielding constants and chemical shifts (in ppm) of the phosphine and *trans*-platinum(II) complexes using the KT2 functional.

Compounds	Basis set	Relativistic correction to nuclear shielding		Relativistic correction to chemical shift	
		SR	SO	SR	SO
1. Phosphine (PH_3) reference	DZP	-0.33	12.78	---	---
	TZ2P	-0.83	12.09	---	---
	ET-pVQZ	-2.08	10.59	---	---
	QZ4P	-2.04	11.35	---	---
2. trans-[$PtCl_2$(dma)(PPh_3)]	DZP	-1.66	46.22	1.33	-33.43
	TZ2P	-2.33	45.77	1.50	-33.68
	ET-pVQZ	-3.03	45.65	0.95	-35.06
	QZ4P	-2.50	46.56	0.46	-35.66
3. trans-[PtCl(DMSO)(dma)(PPh_3)]$^+$	DZP	3.14	52.21	-3.47	-39.42
	TZ2P	3.19	52.36	-1.64	-40.27
	ET-pVQZ	2.43	52.31	1.98	-41.73
	QZ4P	2.13	52.65	-4.17	-37.12
4. trans-[PtCl(H_2O)(dma)(PPh_3)]$^+$	DZP	3.14	46.65	-3.47	-33.86
	TZ2P	2.63	46.40	-3.46	-34.30
	ET-pVQZ	1.77	46.23	-3.85	-35.64
	QZ4P	1.85	46.70	-3.89	-31.46
5. trans-[PtCl(Acetone)(dma)(PPh_3)]$^+$	DZP	1.23	46.10	-1.56	-33.32
	TZ2P	0.93	45.96	-1.76	-33.87
	ET-pVQZ	0.22	46.10	-2.31	-35.51
	QZ4P	0.37	46.58	-2.41	-32.82
6. trans-[Pt$(DMSO)_2$(dma)(PPh_3)]$^{2+}$	DZP	5.44	50.72	-5.77	-37.94
	TZ2P	5.70	51.17	-6.53	-39.08
	ET-pVQZ	5.00	51.13	-7.08	-40.54
	QZ4P	4.71	51.31	-6.75	-33.21
7. trans-[Pt$(H_2O)_2$(dma)(PPh_3)]$^{2+}$	DZP	10.41	52.10	-10.74	-39.31
	TZ2P	10.19	51.80	-11.02	-39.70
	ET-pVQZ	9.20	51.72	-11.29	-41.14
	QZ4P	8.72	51.57	-10.77	-29.45
8. trans-[Pt$(Acetone)_2$(dma)(PPh_3)]$^{2+}$	DZP	6.84	49.81	-7.17	-37.03
	TZ2P	6.95	49.89	-7.78	-37.80
	ET-pVQZ	6.13	50.08	-8.21	-39.50

	QZ4P	5.72	49.73	-7.76	-30.62
9. Pt(DMSO)(H_2O)(dma)(PPh_3)$^{2+}$	DZP	7.09	49.22	-7.43	-36.44
	TZ2P	6.98	49.05	-7.81	-36.96
	ET-pVQZ	6.11	49.12	-8.19	-38.54
	QZ4P	5.73	48.40	-7.78	-29.28
10. trans-[Pt(DMSO)(Acetone)(dma)(PPh_3)]$^{2+}$	DZP	5.46	49.80	-5.79	-37.02
	TZ2P	5.68	50.12	-6.51	-38.03
	ET-pVQZ	5.06	50.21	-7.14	-39.63
	QZ4P	4.55	50.18	-6.59	-32.24
11. trans-[Pt(H_2O)(Acetone)(dma)(PPh_3)]$^{2+}$	DZP	8.46	50.91	-8.79	-38.12
	TZ2P	8.54	50.91	-9.37	-38.82
	ET-pVQZ	7.69	51.00	-9.77	-40.41
	QZ4P	7.12	50.73	-9.16	-30.21

Appendix A3

Supporting material of Chapter 6, *"Computational NMR Spectroscopy for Host-Guest Hemicarcerands"*

Figure A3.1. Most stable structures of hemicarceplexes (**1@G**) optimized at the PBE-D/TZ2P level.

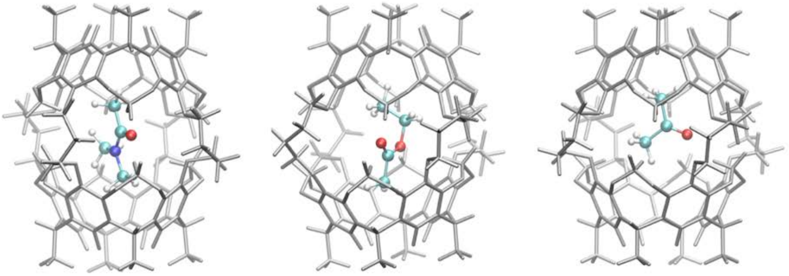

1a: $(CH_3)_2NCOCH_3$ **2a:** $CH_3CO_2CH_2CH_3$ **3a:** CH_3COCH_3

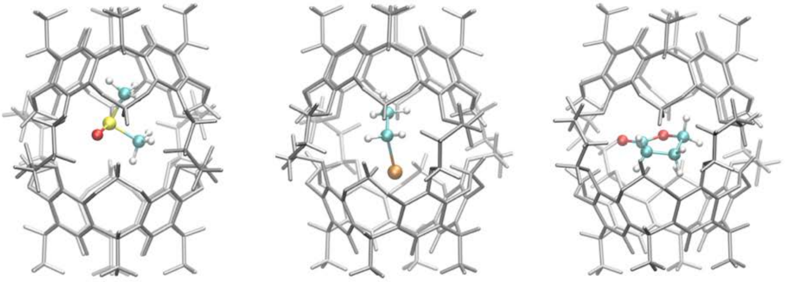

4a: CH_3SOCH_3 **5a:** CH_3CH_2I **6b:** 4-bytyrolactone

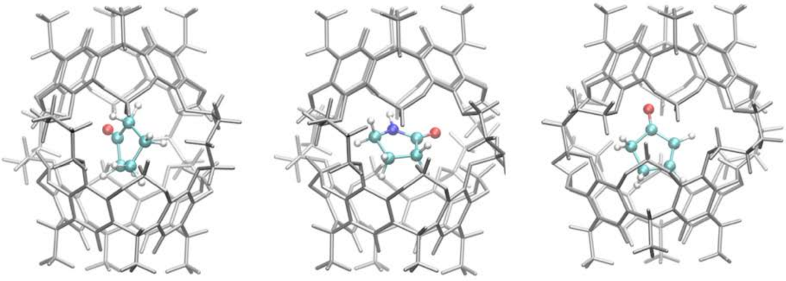

7b: cyclopentanone **8b:** $CH_2CH_2CH_2CONH$ **9b:** 2-cyclopenten-1-one

10c: benzene

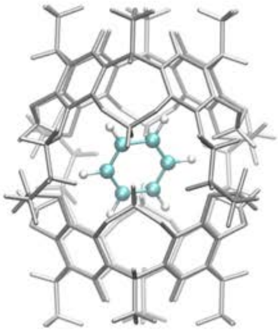

11c: $C_6H_5NH_2$

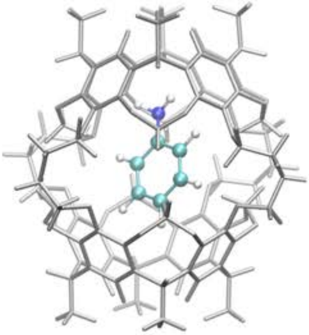

12c: $C_6H_5NO_2$

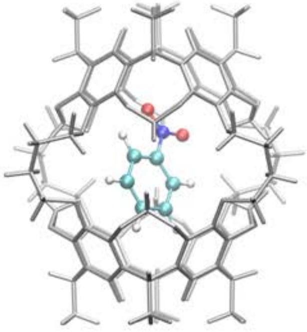

13c: C_6H_5I

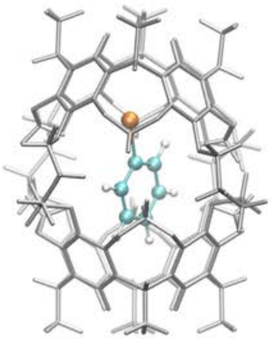

14d: 1,4-$Br_2C_6H_4$

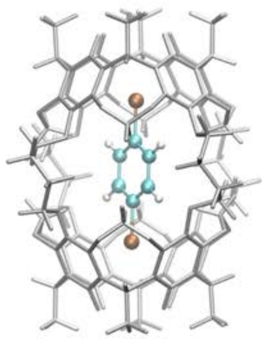

15d: 1,4-$(CH_3)_2C_6H_4$

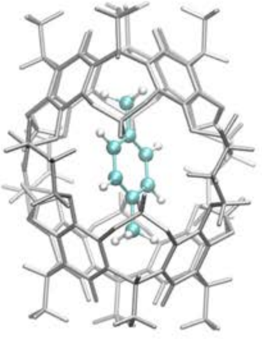

16d: 1,4-$(CH_3O)_2C_6H_4$

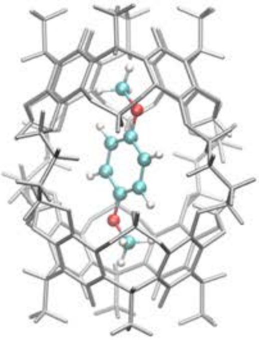

17d: 1,4-$(OH)_2C_6H_4$

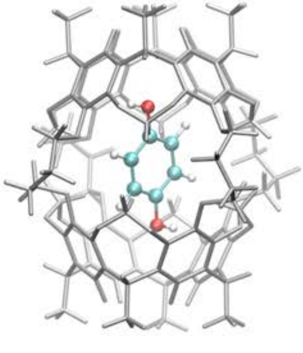

18d: 4-$CH_3C_6H_4OCH_3$

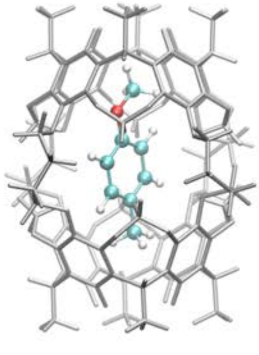

19d: 4-$FC_6H_4CH_3$

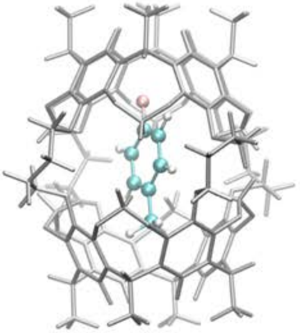

20d: 1,4-$I_2C_6H_4$

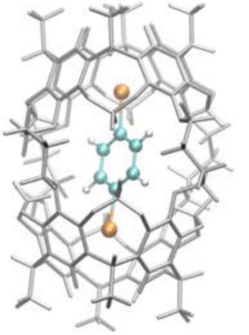

21e: 1,2-$(OH)_2C_6H_4$

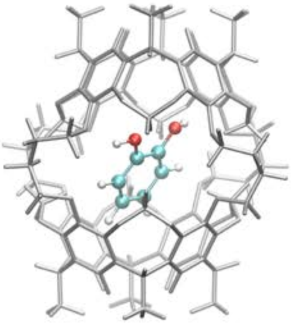

22e: 1,3-$(CH_3)_2C_6H_4$

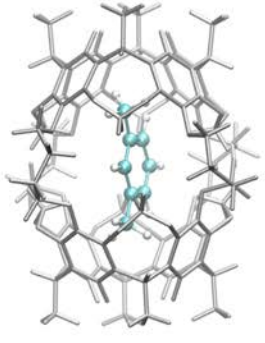

23e: 2-BrC_6H_4OH

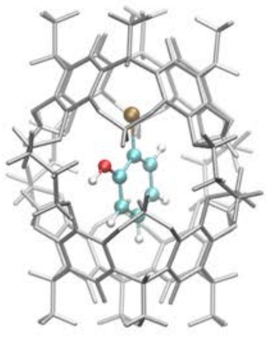

24f: 2,4-$Cl_2C_6H_3CH_3$

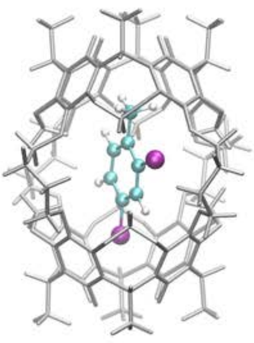

25f: 2,5-$(OH)_2C_6H_3CH_3$

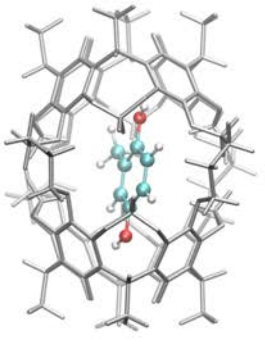

26f: 3,4-$Cl_2C_6H_3CH_3$

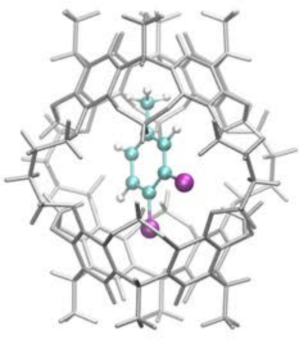

27f: 3,4-$(OH)_2C_6H_3CH_3$

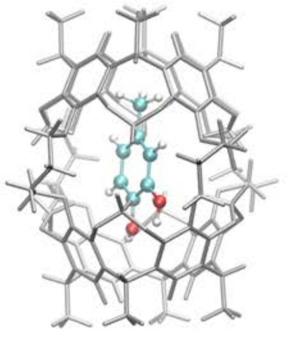

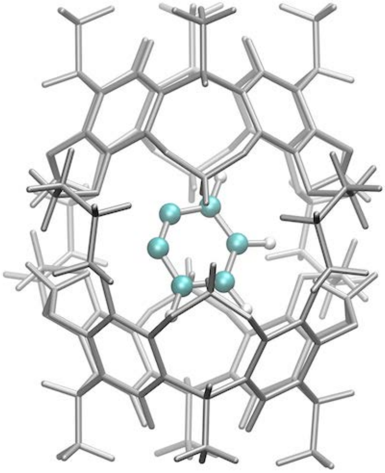Figure A3.2. Structure of (**1@o-benzyne**) optimized at the PBE-D/TZ2P level.